Universiteit
Leiden
The Netherlands

Heterogenized molecular (pre)catalysts for water oxidation and oxygen reduction

Ham, C.J.M. van der

Citation
Ham, C. J. M. van der. (2019, October 10). *Heterogenized molecular (pre)catalysts for water oxidation and oxygen reduction*. Retrieved from https://hdl.handle.net/1887/79257

Version:	Publisher's Version
License:	Licence agreement concerning inclusion of doctoral thesis in the Institutional Repository of the University of Leiden
Downloaded from:	https://hdl.handle.net/1887/79257

Note: To cite this publication please use the final published version (if applicable).

Cover Page

Universiteit Leiden

The handle http://hdl.handle.net/1887/79257 holds various files of this Leiden University dissertation.

Author: Ham, C.J.M. van der
Title: Heterogenized molecular (pre)catalysts for water oxidation and oxygen reduction
Issue Date: 2019-10-10

Heterogenized molecular (pre)catalysts for water oxidation and oxygen reduction

Proefschrift

ter verkrijging van

de graad van Doctor aan de Universiteit Leiden,

op gezag van Rector Magnificus prof. mr. C.J.J.M. Stolker

volgens besluit van het College voor Promoties

te verdedigen op donderdag 10 oktober 2019

klokke 13:45 uur

door

Cornelis Jozef Maria van der Ham

geboren te Gouda in 1989

Promotiecomissie:

Promotor:	Prof. dr. M.T.M. Koper
Co-promotor:	Dr. D.G.H. Hetterscheid
Overige leden:	Prof. dr. E. Bouwman
	Prof. dr. M. Ubbink
	Dr. S. Bonnet
	Prof. dr. M. Albrecht (Universität Bern, Switzerland)
	Dr. J.P. Hofmann (TU Eindhoven, The Netherlands)

ISBN: 978-90-830276-2-3

Printing: Print Service Ede

Cover illustration: starline / Freepik

Voor moeders

Table of Contents

1 Introduction **3**

1.1 Renewable energy and its storage 4

1.2 The thin line between homogeneous and heterogeneous catalysis . . . 12

1.3 Homogeneous *versus* heterogeneous electrochemical water oxidation and oxygen reduction catalysis concerning molecular (pre)catalysts 19

1.4 References 21

2 Structure dependence on the activation of molecular iridium precatalysts for the water oxidation reaction **27**

2.1 Introduction 28

2.2 Experimental 31

2.3 Results 36

2.4 Discussion 46

2.5 Conclusions 52

2.6 References 52

3 Activation pathways taking place at molecular copper precatalysts for the oxygen evolution reaction **57**

3.1 Introduction 58

3.2 Experimental 59

3.3 Results 63

3.4 Conclusions 69

4 *In situ* generated copper-phenanthroline complexes as catalysts for the oxygen reduction reaction **75**

4.1 Introduction 76

4.2 Experimental 78
4.3 Results 80
4.4 Discussion 88
4.5 Conclusion 92
4.6 References 92

5 Phenanthroline immobilized on Au electrodes as ligand in copper-mediated oxygen reduction 95

5.1 Introduction 96
5.2 Experimental 98
5.3 Results and discussion 100
5.4 Conclusion 119
5.5 References 119

6 Summary 121

1 | Introduction

"Advice is a dangerous gift, even from the wise to the wise, and all courses may run ill."

J.R.R. Tolkien in *The Fellowship of the Ring*

1.1 Renewable energy and its storage

1.1.1 The energy problem and catalysis

Between 400,000 B.C. and 1950, the global carbon dioxide concentration in the atmosphere has been fluctuating.[1] The highest value for the estimated CO_2 concentration in that period is approximately 300 ppm.[1] As a consequence of the use of fossil fuel the carbon dioxide concentration in the atmosphere has increased far beyond the natural fluctuations observed before 1950. Currently the CO_2 concentration is somewhat above 400 ppm while the emission of CO_2 is still increasing annually.[2, 3] The increase in global CO_2 concentration is the major cause of global climate change.[4]

In order to limit the global temperature increase, more renewable energy sources need to be employed. Solar energy and wind energy are promising alternatives for the traditional fossil fuels.[5, 6] One of the big challenges of renewable energy that needs to be faced before implementation is the large-scale storage of this renewable energy. Batteries are good energy carriers for low energy applications. However, the transportation of energy stored in batteries for large scale applications is cumbersome. Moreover batteries in general are not very environmentally friendly due to the presence of heavy metals such as lead. Storage of energy in a chemical fuel *e.g.* has the advantage of forming a full cycle in which no waste products are formed. The storage of energy as a chemical fuel therefore is an interesting alternative to the use of batteries in for example the automotive industry.

The reduction of protons and CO_2 to chemical fuels such as hydrogen and hydrocarbons has received a lot of attention lately.[7–12] The proton reduction reaction (PRR) to produce hydrogen and the hydrogen oxidation reaction (HOR) to consume hydrogen are shown in Equation 1.1.[7–11]

$$2\,H^+ + 2\,e^- \underset{\text{HOR}}{\overset{\text{PRR}}{\rightleftharpoons}} H_2 \tag{1.1}$$

A generalized reaction scheme for the reduction of CO_2 is displayed in Equation 1.2

$$CO_2 + n\,H^+ + n\,e^- + 2\,e^- \rightleftharpoons CO + \text{hydrocarbons} + \text{alcohols} + m\,H_2O \tag{1.2}$$

An electrochemical cell consists of two halfreactions, thus a second halfreaction is needed

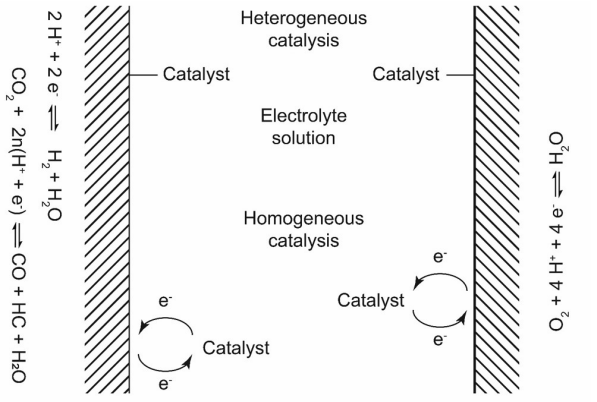

Figure 1.1: Schematic representation of heterogeneous (top part) and homogeneous (bottom part) catalysts as used in an electrochemical cell, HC = hydrocarbons.

to complement the PRR/HOR halfreaction. The water oxidation reaction (WOR) and oxygen reduction reaction (ORR) are good reactions to complement the PRR/HOR (see Equation 1.3), thus forming a closed cycle of two half reactions. The high redox potential (1.23 V *versus* RHE) and the non-toxicity of water and oxygen formed makes this redox reaction very suitable to in combination with the PRR and HOR redox reaction. The oxygen can be released into the atmosphere during fuel production. The waste products of the consumption of the renewable fuels produced 1.1 and 1.2 are water (in Equation 1.1 and 1.2) and CO_2 (in Equation 1.2 only). Both water and CO_2 are non-toxic products. Water is harmless for the environment whereas the CO_2 produced upon the oxidation of alcohols and hydrocarbons is captured from the atmosphere when these fuels are produced, so net no CO_2 is produced. In order to increase the rate and efficiency of the redox reactions, efficient catalysts are needed.

$$O_2 + 4\,H^+ + 4\,e^- \underset{\text{WOR}}{\overset{\text{ORR}}{\rightleftharpoons}} 2H_2O \tag{1.3}$$

In 1901, Ostwald discerned four different types of catalysis. In a 1902 publication in Nature, he stated: "*Catalytic action may be divided in four classes:-(1) Release in supersaturated systems. (2) Catalysis in homogeneous mixtures. (3) Heterogeneous catalysis. (4) Enzyme reactions.*".[13] The first process later became known as crystallization and is thus a physical phenomenon and not

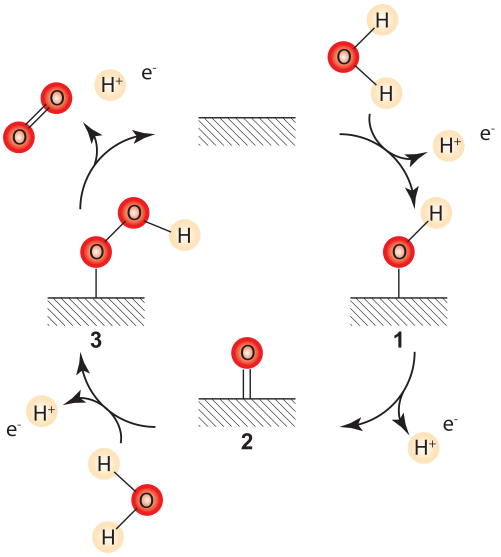

Figure 1.2: The most common mechanism for the electrochemical oxidation of water on heterogeneous surfaces.[15]

chemical nor catalytic.[14] In water oxidation and oxygen reduction catalysis, the focus is mostly on heterogeneous and homogeneous catalysis. Both have different traits and thus different advantages and disadvantages. In heterogeneous catalysis, the catalyst is in a different phase as the reactants. In electrocatalysis this means that the heterogeneous catalyst is the electrode itself or at least attached to the electrode surface (top part of Figure 1.1). Heterogeneous catalysts can be quite stable but are limited in opportunities for design. In homogeneous catalysis the catalyst and the reactant are in the same solution phase (bottom part of Figure 1.1). This means that in homogeneous electrocatalysis the electrode is only transferring electrons to or from the catalyst which is dissolved in the (aqueous) electrolyte and situated in very close proximity to the electrode. Homogeneous catalysts are generally more easy to tune than heterogeneous catalysts, but in general lack in stability.

1.1.2 Heterogeneous catalysts for the electrochemical oxidation of water

Heterogeneous electrocatalysis for the water oxidation and oxygen reduction reactions is a much more explored field compared to homogeneous electrocatalysis.[16–19] In the most common model, the first step in the heterogeneous water oxidation mechanism is the binding of the water molecule to a vacant site on the metal-oxide surface where it is oxidized and deprotonated, forming a metal hydroxide (Figure 1.2, **1**). This hydroxide is further oxidized and deprotonated forming a oxo-species (**2**). The oxo-species undergoes an attack by water and deprotonation and oxidation of the water molecule forming a superoxo-species (**3**). The superoxo-species is deprotonated and oxidized and dioxygen is liberated from the electrode surface (**4**).

The equilibrium potential for the water oxidation reaction ($E^0_{O_2/H_2O}$) is 1.23 V *versus* RHE.[20] From this equilibrium potential the free energy of a dioxygen molecule can be calculated when the free energy of water is defined as zero (Equations 1.4 and 1.5).[20]

$$e_0 E^0_{O_2/H_2O} = C_0 = [\Delta G(O_2) - \Delta G(H_2O)]/4 = 1.23\ \text{eV} \tag{1.4}$$

$$\Delta G(O_2) = 4 \times C_0 = 4.92\ \text{eV} \tag{1.5}$$

The optimal water oxidation catalyst for the heterogeneous oxidation of water should fulfill the condition wherein the intermediates **1**, **2** and **3** have an increased metal binding energy of 1.23 eV per reaction step (Equations 1.6-1.8).[20]

$$\Delta G(OH_{Ads}) = C_0 = 1.23\ \text{eV} \tag{1.6}$$

$$\Delta G(O_{Ads}) = 2 \times C_0 = 2.46\ \text{eV} \tag{1.7}$$

$$\Delta G(OOH_{Ads}) = 3 \times C_0 = 3.69\ \text{eV} \tag{1.8}$$

The scaling relations describe that the binding energy of all intermediates are connected, due to the similarity in the manner in which the intermediates are bound to the catalyst, as was first described in the group of Nørskov.[21] This means that it is not possible to optimize the binding energy of the intermediates to the electrode surface individually. The difference in binding energy of the OH_{Ads} and OOH_{Ads} species is 3.2 ± 0.2 eV on flat (111) surfaces, which is higher than the optimal 2.46 eV (Figure 1.3).[22] This non-optimal difference in binding energy between the

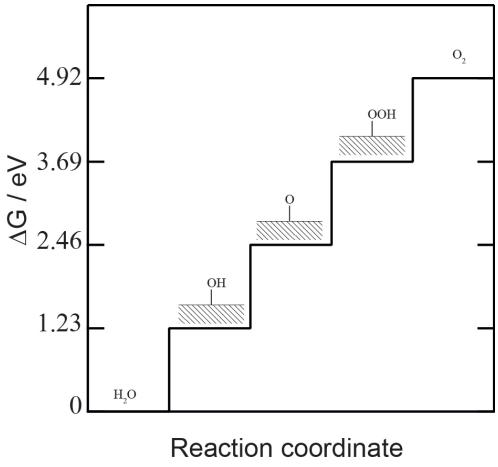

Figure 1.3: Intermediates in heterogeneous water oxidation reaction with their optimal binding energy. The arrow indicates the minimum binding energy difference for OH_{Ads} and OOH_{Ads}, which is 3.2 eV instead of the thermodynamic 2.46 eV due to scaling relations.

OH_{Ads} and OOH_{Ads} species leads to an additional potential that needs to be applied above the equilibrium potential of 1.23 V *versus* RHE for the water oxidation reaction. The extra potential that needs to be applied above the equilibrium potential to start catalysis is called the overpotential. In Figure 1.3 the energy levels of the intermediates are displayed *versus* the reaction coordinate under ideal circumstances. The steps which form the bottleneck of 3.2 eV *versus* the ideal 2.46 eV are indicated by the arrow.

The group of Jaramillo reported a benchmarking study for the water oxidation reaction wherein different surface metal oxide deposits on glassy carbon electrodes were investigated in alkaline media.[19] The potential was measured while water oxidation was performed chronoamperometrically at 10 mA cm^{-2} based on the geometric surface area. The metal oxide surfaces under consideration consisted of (alloys of) Co, La, Fe, Ir, Ni and Ce. IrO_2 was the best performing electrocatalyst with a potential of 1.55 V *versus* RHE at 10 mA cm^{-2}. The best performing non-noble metal catalyst was shown to be $NiFeO_x$ with a reported potential of 1.58 V *versus* RHE at 10 mA cm^{-2}. The potential for all non-noble metal catalyst are similar at 10 mA cm^{-2} between 1.58

and 1.66 V *versus* RHE. The IrO_2 catalyst has a lower potential at 10 mA cm^{-2}, but is unstable during long term electrolysis. However, in acidic electrolyte, the potential and thus the activity of IrO_2 was stable over 2 hours at 1.6 V *versus* RHE, whereas the non-noble metal based catalysts lost their activity.

1.1.3 Homogeneous catalysts for the (electro)chemical oxidation of water

For the homogeneous oxidation of water two different mechanisms are predominantly described in literature.[23] The first mechanism is similar to the mechanism for heterogeneous catalysts for water oxidation (Figure 1.2). In homogeneous context this mechanism is called the water nucleophilic attack (WNA) mechanism. The only difference between the heterogeneous and homogeneous mechanisms is that the electrode surface, depicted by the hatched rectangle in Figure 1.2, is replaced with the metal center of the molecular catalyst (M). Homogeneous catalytic systems following the WNA mechanism suffer from the same scaling relations and intrinsic overpotential as their heterogeneous counterparts. The difference in binding energy between each intermediate to the metal center needs to be equal to 1.23 eV (Equations 1.6-1.8). However the energy difference between the M-OH and M-OOH intermediates will be around 3.2 eV instead of the ideal 2.46 eV, leading to an intrinsic overpotential before water oxidation catalysis starts.

The other mechanism predominantly reported in literature starts with two metal binding sites which bind water and go through two deprotonation and oxidation steps, forming two metal-oxo species (Figure 1.4).[15] These two metal-oxo species couple via a radical reaction, dioxygen is released and the free binding sites on the two metal centers are available for a new catalytic cycle. This mechanism is called the radical oxo coupling (ROC) mechanism. In the ROC mechanism the optimal catalyst is found when $\Delta G_{M\text{-}OH}$ = 1.23 eV and $\Delta G_{M\text{-}O\bullet}$ = 2.46 eV, similarly to the WNA mechanism.[15] The potential limiting factor in catalysts displaying the WNA mechanism is the non-optimal $\Delta G_{M\text{-}OH} - \Delta G_{M\text{-}OOH}$ energy difference of at least 3.2 eV. Since there is no M-OOH intermediate in the ROC catalytic cycle, this bottleneck does not exist in the ROC mechanism, which might lead to catalysts with a lower overpotential.

The first report of a molecular water oxidation catalyst was by Meyer *et al* in 1982 (Figure 1.5, top left).[24] They reported a ruthenium-based $[(bpy)_2(H_2O)RuO\text{-}Ru(H_2O)(bpy)_2](ClO_4)_4$ complex (bpy = 2,2'-bipyridine) which evolves oxygen both electrochemically in acidic electrolyte

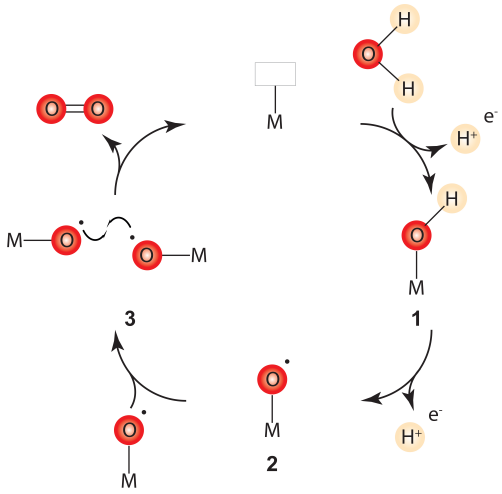

Figure 1.4: Radical oxo coupling (ROC) mechanism for certain homogeneous water oxidation catalysts.

and by chemical oxidation using cerium(IV) as chemical oxidant. A multitude of molecular complexes as catalysts for the water oxidation reaction has been reported since then. In the group of Sun, severak Ru-based molecular complexes have been developed as catalysts for both chemical and photochemical water oxidation (Figure 1.5, top right).[25] The complex [Ru(bda)(isoq)$_2$] (H_2bda = 2,2'-bipyridine-6,6'-dicarboxylic acid; isoq = isoquinoline) was used as catalyst to oxidize water using cerium(IV) or $[Ru(bpy)_3]^{2+}$ and light. A ROC mechanism was proposed wherein a ruthenium(IV) peroxo-dimer is formed.[26] Liberation of oxygen is the rate-limiting step under stoichiometric amounts of cerium(IV). Under excess of cerium(IV), oxygen liberation happens after the peroxo-dimer is further oxidized to form a superoxo-dimer and the rate determining step changes to the formation of the peroxo-dimer.

The first iridium-based molecular catalyst for the water oxidation reaction was reported by the group of Bernhard (Figure 1.5, bottom left).[27] A series of different cyclometallated iridium complexes was studied under chemical oxidation conditions and shown to perform water oxidation, forming dioxygen as the product. Since then different iridium-based catalysts for the water oxidation reaction have been reported.[28–30] Under electrocatalytic conditions some of

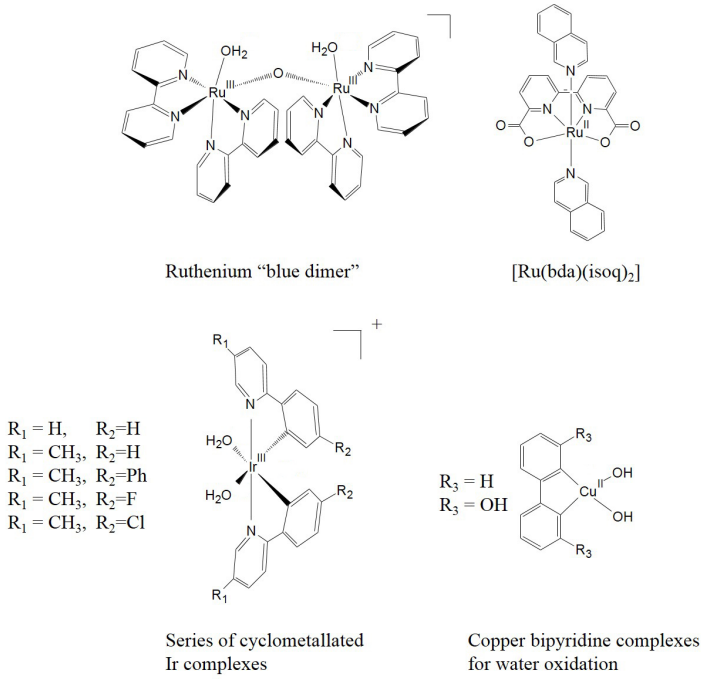

Figure 1.5: Examples of molecular complexes used in (electro)chemical water oxidation and oxygen reduction studies.

those complexes form a IrO_2 deposit on the electrode surface.[31–33] In electrocatalytic studies of molecular iridium complexes it is therefore a challenge to prevent the formation of iridium oxide layers on the electrode surface.

1.1.4 Copper complexes for the electrochemical water oxidation and oxygen reduction reaction.

Molecular copper electrocatalysts have been reported both for the water oxidation reaction and oxygen reduction reaction.[34–40] The first reported copper-based water oxidation catalyst is a copper bipyridine system which forms a mononuclear bishydroxy complex at high pH (Figure 1.5, bottom right).[39] Water oxidation catalysis was observed in a pH range of 11.6 to 13.3. A turnover frequency of 100 s^{-1} is reported at glassy carbon electrodes. Quickly after, a sec-

ond report on homogeneous water oxidation from the group of Lin appeared, wherein a 6,6'-dihydroxy-2,2'-bipyridine ligand was used. It has a lower overpotential and higher activity than the 2,2'-bipyridine complex, which is attributed to the proton shuttling effect of the hydroxy groups present on the bipyridine ligand. A number of copper based complexes have been reported for the oxygen reduction reaction with phenanthroline derivative ligands and its derivatives,[41–43] and pyridylalkylamine ligands.[44, 45] In homogeneous copper catalysis the challenge lies in finding catalysts that do not form heterogeneous copper (oxide) layers instantaneously on the electrode surface. This is due to the fast ligand exchange kinetics of copper, which may lead to the formation of free copper ions in the electrolyte solution.[46] Nevertheless, in literature the formation of heterogeneous metal (oxide) catalysts under reaction conditions is rarely discussed.

1.2 The thin line between homogeneous and heterogeneous catalysis

1.2.1 Degradation of homogeneous catalysts

Pinpointing the active species can be a challenge in homogeneous catalysis, as often only the resting states of the catalytic species are detectable, whereas the true active species are only present in undetecteable concentrations.[14] Since molecular catalyst have a lower stability than heterogeneous catalysts, catalyst degradation can be a major problem. In a 2011 review, Crabtree gave an overview of how homogeneous species may degrade during a catalytic reaction and how one may recognize the formation of nanoparticles.[14] The most important indications of the formation of heterogeneous catalysts from homogeneous species are summarized in Table 1.1.[14] One should always keep in mind the possibility of forming a heterogeneous catalyst from a homogeneous complex.

1.2.2 The difficulty in determining the active species in electrochemical homogeneous catalysis

The thin line between homogeneous and heterogeneous catalysis as discussed in the previous section also holds for electrochemical studies. Under oxidative conditions the formation of metal

Table 1.1: *Suspicious circumstances suggesting a need for further study of an operationally homogeneous metal catalyst system, adapted from Crabtree.[14]*

Events	**Comment**
Unexplained lag time before onset of catalysis	Conversion of molecular precursor to an active catalyst, possibly nanoparticulate
Catalyst properties, such as selectivity, closely resemble the properties of the appropriate analogous conventional heterogeneous catalyst	Nanoparticle (NP) catalysis possible
Ligand (L) effects are minimal; all active catalysts have similar rates and properties	All catalysts may convert to NPs having similar catalytic properties whatever the nature of L, but ligands can modify NP synthesis and so ligand-dependent activity cannot eliminate the possibility that NPs are the active species
Catalytic activity is halted by a selective poison for the heterogeneous catalyst	Hg(0) is most common but precautions are needed
Kinetic irreproducibility	Nanoparticle synthesis can be very dependent on conditions
Reaction mixture turns dark in color	Possible indication of NPs
Metal-containing deposit or mirror formed	Possible indication of intermediacy of NPs, and the deposit itself may be catalytically active
Harsh conditions	Ligands may degrade and release metal

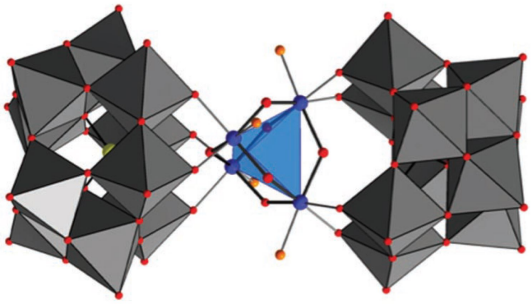

Figure 1.6: Structure of the ruthenium based POM **1** as reported simultaneously in the groups of Hill ([49]) and Bonchio ([50]). Depicted is the central $Ru_4(\mu\text{-}O)_4(\mu\text{-}OH)_2(H_2O)_4{}^{6+}$ core (ball-and-stick representation, Ru blue, μ-O red- $O(H_2)$ orange; hydrogen atoms omitted for clarity) and the slightly distorted Ru_4 tetrahedron (transparent blue). The polytungstate fragments are shown as gray octahedra, and Si as yellow spheres. The figure was reprinted from [49].

oxides from coordination compounds has been observed, whereas under reductive conditions the formation of a metallic layer is a possibility. The difficulty of interpretation of the data and the care with which the experimental conditions should be chosen is greatly displayed in the study of Co-based polyoxometallates (POMs) as water oxidation catalysts described by the groups of Hill [47] and Finke.[48] Both argued on the specification of the active species of these POM systems. Since these systems have been discussed in so many details, and since the same problems are likely to arise for other systems, it is presented here as a case study.

Polyoxometallate compounds are carbon-free ligands that can bind to metal ions, for example ruthenium. The ruthenium-based POM $Rb_8K_2[Ru_4O_4(OH)_2(H_2O)_4(\gamma{-}SiW_{10}\text{-}O_{36})_2]\cdot 25H_2O$ (**1**) was developed simultaneously in the groups of Bonchio[50] and Hill[49]. In the group of Hill, it was shown to oxidize water using both $[Ru(bpy)_3]^{3+}$[49, 51] and $(NH_4)_2[Ce(NO_3)_6]$ (CAN)[51] as chemical oxidant. Experiments using isotopically labelled water showed the formation of dioxygen from water and not from oxygen present in **1**.[49] Control experiments were performed with $[RuCl_3]$, which forms RuO_2 under catalytic conditions. The $RuCl_3$ catalyst showed an activity two orders of magnitude lower than that of **1**, indicating the complex does not degrade into RuO_2 during catalysis. The rate limiting step for water oxidation was determined to be the first oxidation

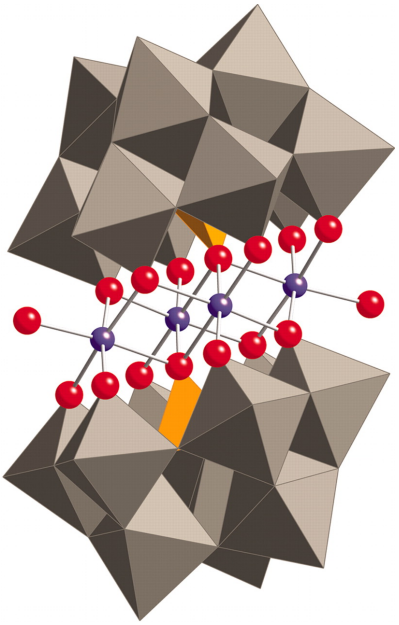

Figure 1.7: X-ray structure of Na_{10}**2** in combined polyhedral ($[PW_9O_{34}]$ ligands) and ball-and-stick (Co_4O_{16} core) notation. Co atoms are purple; O/OH_2(terminal) are red; PO_4 is displayed as orange tetrahedrals; and WO_6 as gray octahedra. Hydroge natoms, water molecules, and sodium cations are omitted for clarity. Figure reprinted from [47].

of water from the four times oxidized complex.[51] The complex is stable in water from neutral to slightly acidic pH, but will decompose below a pH of 1.5.[49]

Simultaneously in the group of Bonchio, the same polyoxometallate was developed and investigated using CAN.[50] Oxygen evolution was confirmed using gas chromatography and maximum turn over frequencies of 450 h^{-1} were observed. The catalyst was precipitated from the aqueous solution after water oxidation by addition of CsCl. Infrared and Raman spectroscopy of the precipitated complex confirmed the stability of the catalyst.

After this ruthenium-based POM compound, Hill reported the first Co_4-POM as active water oxidation catalyst.[47] The POM compound $[Co_4(H_2O)_2(PW_9O_{34})_2]^{10-}$ (**2**, Figure 1.7) was claimed to be an active water oxidation catalyst using both chemical and electrochemical oxidation. It was the only cobalt-based POM in a series to exhibit water oxidation using $[Ru(bpy)_3]^{3+}$.

A total turn over number (TON) of 75 was observed with a yield of 64%, based on the amount of $[Ru(bpy)_3]^{3+}$ added to the reaction solution. It was stated the catalyst could be kept in solution for 72 hours prior to catalysis without a significant change in TON and yield. At pH 8 a solution containing 5 μM **2** could be kept in water for over a month without changes in the ^{31}P NMR and the UV-Vis spectra. Nevertheless there is a concern that small amounts of Co^{2+} are responsible for the catalytic activity. By addition of bpy to to the solution, any free Co^{2+} in solution could be scavenged to form an inactive complex.[47] Some decrease in water oxidation activity is observed, which is attributed to loss of Co^{II} from the POM by competitive coordination of bpy and the oxidation of bpy. After the chemical oxidation by $[Ru(bpy)_3]^{3+}$ was completed, more $[Ru(bpy)_3]^{3+}$ was added to the catalyst solution. The same initial activity was observed in the second addition of $[Ru(bpy)_3]^{3+}$ as in the first addition, indicating no catalyst degradation took place during the first catalytic run.

By replacing the $[Ru(bpy)_3]^{3+}$ with the reduced form $[Ru(bpy)_3]^{2+}$ and with the addition $Na_2S_2O_8$ as sacrificial reductant, light-activated water oxidation was performed with **2** as catalyst.[52] An increase in both catalytic as well as initial quantum yield was observed with increasing catalyst concentration at pH 8. The highest TON of 224 was observed at 5 μM, the highest concentration used in this report.

Stracke and Finke continued the investigation of **2** electrochemically.[48] By performing a long-term cyclic voltammetry experiment with 500 μM solutions of **2** at pH 8 between 1.47 and 1.87 V *versus* RHE, the behavior of the catalyst over time was investigated at a 0.071 cm^2 glassy carbon (GC) electrode. The onset for water oxidation is observed around 1.65 V *versus* RHE. At the beginning of the experiment, the current reaches a maximum of 11 μA at the vertex potential of 1.86 V. Over time the maximum current increases to 140 μA after 3 hours of cycling. Such an activation process indicates a transformation of the molecular species and possibly deposition of material on the electrode surface. Scanning electron microscopy (SEM) in combination with energy dispersive X-ray spectroscopy (EDX) confirmed the presence of a cobalt layer on the surface of the GC electrode. The layer contained Co, O, P, and Na, with a Co:P:Na ratio of approximately 4:1:1, as determined by EDX. No tungsten from the PW_9O_{34} moiety was observed in the deposit. The CoO_x layer could also be formed by applying an oxidizing potential of 1.76 V *versus* RHE for 30 minutes. By transferring the electrode with deposit to an electrolyte solution in the absence of

2, the catalytic activity was retained. This suggests that the catalytic activity should be attributed to the surface adsorbed CoO_x.

The formation of the CoO_x layer under electrochemical conditions led to a further investigation of the catalytically active catalytic species under photochemical circumstances by Sartorel, Scandola and co-workers.[53] Using nanosecond flash photolysis, a 50 μM solution of $[Ru(bpy)_3]^{2+}$ was transformed (partly) into $[Ru(bpy)_3]^{3+}$. Depletion of the $[Ru(bpy)_3]^{3+}$ by reduction by a 5 μM solution of **2** was measured in the μs timescale using UV-Vis. As the catalyst was aged for longer times before photolysis, depletion of $[Ru(bpy)_3]^{3+}$ was faster, indicating that a decomposition product formed *in situ* is responsible for the depletion of $[Ru(bpy)_3]^{3+}$. As the oxidation of pristine **2** in cyclic voltammetry is higher than the oxidation potential of $[Ru(bpy)_3]^{3+}$, (photo)chemical water oxidation of **2** should not be possible with $[Ru(bpy)_3]^{2+}$ as oxidatant. The timescales wherein the $[Ru(bpy)_3]^{3+}$ is depleted does point to a molecular species, as the timescales are similar to stable Ru-POMs and is about 3 orders of magnitude higher than *e.g.* colloidal IrO_2 particles.[53, 54]

The concentration of **2** used in the electrochemical investigation by Stracke and Finke[48] is two orders of magnitude higher (0.5 mM) than the reports from Hill *et al* (<5 μM).[47, 52] An investigation of the maximum absorption of the 580 nm peak in UV-Vis spectroscopy of a 0.5 mM solution of **2** in 0.1 M phosphate buffer at pH 8 shows a decrease of 4.6 $\pm$ 0.6% over 3 hours.[48] This indicates that **2** degrades over time at high concentration. This was further confirmed with linear-sweep voltammetry based on the anodic peak at 1.77 V *versus* RHE at pH 8, which is associated with the presence of free Co^{II} in solution. The total amount of free Co^{II} leached was established electrochemically to be 58 μM after 3 hours, which corresponds to 2.9% of the total amount of cobalt added to the solution.

A further chemical and photochemical investigation of low concentration (<5 μM) of **2** in borate buffer at pH 8, once again showed the active catalyst is the completely intact Co_4-POM, with little to no activity from solvated Co^{II}.[55] Using UV-Vis spectroscopy, it was established that **2** is unstable in phosphate buffer, the buffer used in all reports described above, but is much more stable in borate buffer. Using ICP-MS and cathodic adsorptive stripping voltammetry (CAdSV) experiments a sixfold higher concentration of dissolved cobalt in phosphate buffers over borate buffers was observed. Photochemical water oxidation in the presence of **2** reached a turn over

number of 302 at pH 8, which is much higher than the TON reported for **2** in phosphate buffer. A chemical dioxygen yield of 24.2% was observed in borate buffer at pH 8.

The debate about the homogeneity or heterogeneity of the POM **2** is reviewed in the 2013 *JACS* paper of Geletii, Hill and co-workers concluding: "catalytic studies of molecular species, especially POM WOCs (water oxidation catalysts), under one set of experimental conditions should be compared only with extreme caution, if at all, to those under other conditions."[55]

After the initial 2010 Science paper from the group of Hill,[47] another Co-POM catalyst was reported with $Na_{10}[Co_4(H_2O)_2(VW_9O_{34})_2]\cdot 35H_2O$ (Na_{10}**3**$\cdot 35H_2O$) from the same group in 2014.[56] An exceptionally high TOF of $> 1 \times 10^3$ was observed under chemical oxidation conditions, based on the consumption of $[Ru(bpy)_3]^{3+}$. The catalyst is also active towards light driven water oxidation with $[Ru(bpy)_3]^{2+}$ and $Na_2S_2O_8$ as sacrificial reductant. Multiple spectroscopic techniques were used to establish the stability of the complex in solution and under catalytic conditions. In the ^{51}V NMR spectrum a peak was observed at -506.8 ppm, which does not change over the course of a month.

The stability and structure of the Na_{10}**3**$\cdot 35H_2O$ was questioned in the group of Finke.[57] The synthesis of Na_{10}**3**$\cdot 35H_2O$ yielded a brown powder, of which the elemental analysis was too high in tungsten by 1.56 %.[56, 57] In the synthesis of Na_{10}**3**$\cdot 35H_2O$ by Finke *et al* NaOAc impurities were found which were identified using infrared spectroscopy.[57] The infrared spectra reported by the group of Hill were cut off at 1200 cm^{-1}, well below the peak associated with NaOAc which is observed at 1600 cm^{-1} A critical note was also set at the ^{51}V NMR shift of -508.6 ppm with regard to the nature of that peak. Due to **3** being quadrupolar in vanadium, one would expect this peak to be broad. In **3**, a sharp peak with $\delta\nu_{1/2}$ = 28 Hz is observed at -508.6 ppm[56] or -510 ppm.[57] This is narrower than for any tetrahedral vanadium complex reported to date. Previously $V_4O_{12}{}^{4-}$ was reported to have the narrowest peak with $\delta\nu_{1/2}$ = 60 Hz.[57] If the procedure for synthesis of **3** is followed, but without the addition of the Co^{II} salt the -510 ppm is retained in the ^{51}V NMR spectrum. This indicates the -510 or -508.6 ppm peak is not associated with the complexated form of **3** claimed by Hill and coworkers,[56] but rather with the *cis*-$V_2W_4O_{19}{}^{4-}$ ligands which are dissociated from the cobalt center.[57] Purification of Na_{10}**3**$\cdot 35H_2O$ by recrystallization yielded a green solid which was determined to be mostly *cis*-$V_2W_4O_{19}{}^{4-}$

Electrochemical water oxidation using the Na_{10}**3**$\cdot 35H_2O$ catalyst was performed by Folkman and Finke both in phosphate and in borate buffer.[58] In the first hour of catalysis the oxidation current increases for both phosphate and borate buffers present in the electrolyte solution. The formation of a CoO_x layer is observed on the electrode surface as was confirmed with SEM/EDX. The ease of formation of CoO_x is attributed to free Co^{II}_{aq} dissolved in the electrolyte solution from the decomposition of **3**. The amount of **3** which decomposes is 87 to 100% based on line broadening on the ^{51}P NMR lines and cathodic stripping. The deposition of Co on the electrode surface is the same as was reported earlier by the group of Nocera.[59]

The development of the Co_4-POM systems **2** and **3** have led to a heated discussion in the literature with regard to the homogeneity and the structure of the active catalyst.[47, 48, 52, 53, 55–58] At low concentration, **2** forms a stable complex under (photo)chemical water oxidation conditions,[47, 52] at higher concentrations and under electrochemical water oxidation conditions it forms a metal oxide deposit on the electrode surface.[48] Although $[Ru(bpy)_3]^{3+}$ is not capable of oxidizing **2**, depletion of $[Ru(bpy)_3]^{3+}$ is observed in laser flash photolysis experiments, indicating that **2** decomposes to form a molecular complex with a lower oxidation potential in phosphate buffer.[53] The Co_4-POM **3** is believed not to be structurally correct but decomposes rapidly to form CoO_x under electrochemical conditions which is responsible for the water oxidation catalysis.[57, 58] Due to the harsh conditions of water oxidation catalysis, similar systems with homogeneous catalyst must suffer from stability issues as well, although this is often neglected in electrochemical studies.

1.3 Homogeneous *versus* heterogeneous electrochemical water oxidation and oxygen reduction catalysis concerning molecular (pre)catalysts

1.3.1 Scope of this thesis

The formation of heterogeneous materials from homogeneous (pre)catalysts is not unique to the Co-POM systems. However there are few reports of molecular complexes forming heterogeneous catalysts under reactive conditions. The aim of this thesis is to investigate the mechanism

of the formation of heterogeneous layers under catalytic conditions and strategies to prevent the formation of metal(oxide) deposits on electrodes under catalytic conditions. The focus is on the difficult but important water oxidation and oxygen reduction reactions, which form the bottleneck for the efficient storage of renewable energy in a chemical bond.

In Chapter 2 the water oxidation reaction is reported with two similar pyridyl-triazolylidene iridium complexes, which differ only in one position on the pyridyl-triazolylidene ligand. The influence of the ligand structure on the activity and the activation of the catalytic system has been investigated electrochemically. An *in situ* study on the formation of surface deposits and the gaseous products has been performed, while *ex situ* spectroscopy was used to investigate the structure and nature of the active site.

Copper complexes display rapid ligand exchange kinetics. The exchange rate of water ligands at Cu^{II} complexes is in the order of 10^8 s^{-1}.[46, 60] This is faster than the exchange rate on other first row transition metals such as Fe^{II} (10^5 s^{-1}), Co^{II} (10^4 s^{-1}) and Mn^{II} (10^5 s^{-1}). The exchange rate of water on noble metals is lower, with Ir^{III} having the slowest exchange rate (10^{-6} s^{-1}). The fast exchange kinetics of water ligands at Cu^{II} centers indicates that also other ligands will exchange more rapidly at copper complexes compared to other metals. Therefore care should be taken when using Cu^{II} complexes in the water oxidation and oxygen reduction reactions, as free Cu^{II} may be present already at very early stages during the catalytic reaction.

In Chapter 3 a $[Cu^{II}(bdmpza)_2]$ complex (bdmpza$^-$ = bis(3,5-dimethyl-1H-pyrazol-1-yl)acetate has been investigated for the water oxidation reaction. The exchange of the ligands with water or ions present in the electrolyte is minimized by the use of a tridentate bis-pyrazole ligand. The formation of a CuO layer was, however, not prevented, but even faster obtained if the complex was first treated under reducing conditions.

In Chapter 4 *in situ* generated Cu^{II} complexes with 1,10-phenanthroline ligands are reported for the oxygen reduction reaction. The use of a high concentration of 1,10-phenanthroline, should shift the equilibrium of phenanthroline binding towards complex formation, thus preventing the formation of metallic copper on the electrode surface.

Chapter 5 reports copper complexes with 1,10-phenanthrolineligands which are covalently attached to the electrode surface while Cu^{II} is present in the electrolyte solution. In presence of copper, $[Cu(phen)L_x]$ complexes form on the surface of the gold working electrode. By immo-

bilizing the ligands onto the electrode surface, the copper ions cannot get close to the electrode surface. The formation of metallic copper on the electrode surface under oxygen reduction conditions is prevented by blocking of the ligands which are attached to the electrode surface. The *in situ* generated copper complexes have been investigated for the oxygen reduction reaction.

1.4 References

(1) Carbon Dioxide | Vital Signs – Climate Change: Vital Signs of the Planet., https://climate.nasa.gov/vital-signs/carbon-dioxide/, Accessed: 2018-08-06.

(2) US Department of Commerce, NOAA, E. S. R. L. ESRL Global Monitoring Division - Global Greenhouse Gas Reference Network., https://www.esrl.noaa.gov/gmd/ccgg/trends/full.html, Accessed: 2018-08-06.

(3) OMR - OMR Public., https://www.iea.org/oilmarketreport/omrpublic/, Accessed: 2018-08-06.

(4) Global Temperature | Vital Signs – Climate Change: Vital Signs of the Planet., https://climate.nasa.gov/vital-signs/global-temperature/, Accessed: 2018-08-06.

(5) Ellabban, O.; Abu-Rub, H.; Blaabjerg, F. *Renew. Sust. Energ. Rev.* **2014**, *39*, 748–764.

(6) Jacobson, M. Z.; Delucchi, M. A. *Energy Policy* **2011**, *39*, 1154–1169.

(7) Zeradjanin, A. R.; Grote, J.-P.; Polymeros, G.; Mayrhofer, K. J. J. *Electroanal.* **2016**, *28*, 2256–2269.

(8) Zeng, M.; Li, Y. *J. Mater. Chem. A* **2015**, *3*, 14942–14962.

(9) Pedersen, C. M.; Escudero-Escribano, M.; Velázquez-Palenzuela, A.; Christensen, L. H.; Chorkendorff, I.; Stephens, I. E. L. *Electrochim. Acta* **2015**, *179*, 647–657.

(10) Davydova, E. S.; Mukerjee, S.; Jaouen, F.; Dekel, D. R. *ACS Catal.* **2018**, *8*, 6665–6690.

(11) Lu, S.; Zhuang, Z. *Sci. China Mater.* **2016**, *59*, 217–238.

(12) Kibsgaard, J.; Gorlin, Y.; Chen, Z.; Jaramillo, T. F. *J. Am. Chem. Soc.* **2012**, *134*, 7758–7765.

(13) Ostwald, F. W. *Nature* **1902**, *65*, 522–526.

(14) Crabtree, R. H. *Chem. Rev.* **2012**, *112*, 1536–1554.

(15) Hessels, J.; Detz, R. J.; Koper, M. T. M.; Reek, J. N. H. *Chem. Eur. J.* **2017**, *23*, 16413–16418.

(16) Hunter, B. M.; Gray, H. B.; Müller, A. M. *Chem. Rev.* **2016**, *116*, 14120–14136.

(17) Roger, I.; Shipman, M. A.; Symes, M. D. *Nat. Rev. Chem.* **2017**, *1*, 1–13.

(18) Rüttinger, W.; Dismukes, G. C. *Chem. Rev.* **1997**, *97*, 1–24.

(19) McCrory, C. C. L.; Jung, S.; Peters, J. C.; Jaramillo, T. F. *J. Am. Chem. Soc.* **2013**, *135*, 16977–16987.

(20) Koper, M. T. M. *J. Electroanal. Chem.* **2011**, *660*, 254–260.

(21) Fernández, E. M.; Moses, P. G.; Toftelund, A.; Hansen, H. A.; Martínez, J. I.; Abild-Pedersen, F.; Kleis, J.; Hinnemann, B.; Rossmeisl, J.; Bligaard, T.; Nørskov, J. K. *Angew. Chem. Int. Ed.* **2008**, *47*, 4683–4686.

(22) Rossmeisl, J.; Qu, Z.-W.; Zhu, H.; Kroes, G.-J.; Nørskov, J. K. *J. Electroanal. Chem.* **2007**, *607*, 83–89.

(23) Sala, X.; Maji, S.; Bofill, R.; García-Antón, J.; Escriche, L.; Llobet, A. *Acc. Chem. Res.* **2014**, *47*, 504–516.

(24) Gersten, S. W.; Samuels, G. J.; Meyer, T. J. *J. Am. Chem. Soc.* **1982**, *104*, 4029–4030.

(25) Duan, L.; Araujo, C. M.; Ahlquist, M. S. G.; Sun, L. *P. Natl, Acad. Sci. U.S.A.* **2012**, *109*, 15584–15588.

(26) Duan, L.; Bozoglian, F.; Mandal, S.; Stewart, B.; Privalov, T.; Llobet, A.; Sun, L. *Nat. Chem.* **2012**, *4*, 418–423.

(27) McDaniel, N. D.; Coughlin, F. J.; Tinker, L. L.; Bernhard, S. *J. Am. Chem. Soc.* **2008**, *130*, 210–217.

(28) Blakemore, J. D.; Crabtree, R. H.; Brudvig, G. W. *Chem. Rev.* **2015**, *115*, 12974–13005.

(29) Hetterscheid, D. G. H.; Reek, J. N. H. *Eur. J. Inorg. Chem.* **2014**, 742–749.

(30) Hetterscheid, D. G. H. *Chem. Commun.* **2017**, *53*, 10622–10631.

(31) Blakemore, J. D.; Schley, N. D.; Olack, G. W.; Incarvito, C. D.; Brudvig, G. W.; Crabtree, R. H. *Chem. Sci.* **2011**, *2*, 94–98.

(32) Abril, P.; del Rio, M. P.; Tejel, C.; Verhoeven, T. W. G. M.; Niemantsverdriet, J. W.; Van der Ham, C. J. M.; Kottrup, K. G.; Hetterscheid, D. G. H. *ACS Catal.* **2016**, *6*, 7872–7875.

(33) Schley, N. D.; Blakemore, J. D.; Subbaiyan, N. K.; Incarvito, C. D.; D'Souza, F.; Crabtree, R. H.; Brudvig, G. W. *J. Am. Chem. Soc.* **2011**, *133*, 10473–10481.

(34) Van Dijk, B.; Hofmann, J. P.; Hetterscheid, D. G. H. *Phys. Chem. Chem. Phys.* **2018**, *20*, 19625–19634.

(35) Thorum, M. S.; Yadav, J.; Gewirth, A. A. *Angew. Chem. Int. Ed.* **2009**, *48*, 165–167.

(36) Xi, Y.-T.; Wei, P.-J.; Wang, R.-C.; Liu, J.-G. *Chem. Commun.* **2015**, *51*, 7455–7458.

(37) Zhang, T.; Wang, C.; Liu, S.; Wang, J.-L.; Lin, W. *J. Am. Chem. Soc.* **2014**, *136*, 273–281.

(38) Su, X.-J.; Gao, M.; Jiao, L.; Liao, R.-Z. Z.; Siegbahn, P. E. M.; Cheng, J.-P.; Zhang, M.-T. *Angew. Chem. Int. Ed.* **2015**, *54*, 4909–4914.

(39) Barnett, S. M.; Goldberg, K. I.; Mayer, J. M. *Nat. Chem.* **2012**, *4*, 498–502.

(40) Fisher, K. J.; Materna, K. L.; Mercado, B. Q.; Crabtree, R. H.; Brudvig, G. W. *ACS Catal.* **2017**, *7*, 3384–3387.

(41) Zhang, J.; Anson, F. C. *Electrochim. Acta* **1993**, *38*, 2423–2429.

(42) Zhang, J.; Anson, F. C. *J. Electroanal. Chem.* **1992**, *341*, 323–341.

(43) Lei, Y.; Anson, F. C. *Inorg. Chem.* **1994**, *33*, 5003–5009.

(44) Langerman, M. P.; Hetterscheid, D. G. H. *Submitted*.

(45) Asahi, M.; Yamazaki, S.-i.; Itoh, S.; Ioroi, T. *Dalton T.* **2014**, *43*, 10705.

(46) Reedijk, J. *Platin. Met. Rev.* **2008**, *52*, 2–11.

(47) Yin, Q.; Tan, J. M.; Besson, C.; Geletii, Y. V.; Musaev, D. G.; Kuznetsov, A. E.; Luo, Z.; Hardcastle, K. I.; Hill, C. L. *Science* **2010**, *328*, 342–5.

(48) Stracke, J. J.; Finke, R. G. *J. Am. Chem. Soc.* **2011**, *133*, 14872–14875.

(49) Geletii, Y. V.; Botar, B.; Kögerler, P.; Hillesheim, D. A.; Musaev, D. G.; Hill, C. L. *Angew. Chem. Int. Ed.* **2008**, *47*, 3896–3899.

(50) Sartorel, A.; Carraro, M.; Scorrano, G.; De Zorzi, R.; Geremia, S.; McDaniel, N. D.; Bernhard, S.; Bonchio, M. *J. Am. Chem. Soc.* **2008**, *130*, 5006–5007.

(51) Geletii, Y. V.; Besson, C.; Hou, Y.; Yin, Q.; Musaev, D. G.; Quiñonero, D.; Cao, R.; Hardcastle, K. I.; Proust, A.; Kögerler, P.; Hill, C. L. *J. Am. Chem. Soc.* **2009**, *131*, 17360–17370.

(52) Huang, Z.; Luo, Z.; Geletii, Y. V.; Vickers, J. W.; Yin, Q.; Wu, D.; Hou, Y.; Ding, Y.; Song, J.; Musaev, D. G.; Hill, C. L.; Lian, T. *J. Am. Chem. Soc.* **2011**, *133*, 2068–2071.

(53) Natali, M.; Berardi, S.; Sartorel, A.; Bonchio, M.; Campagna, S.; Scandola, F. *Chem. Commun.* **2012**, *48*, 8808.

(54) Natali, M.; Orlandi, M.; Berardi, S.; Campagna, S.; Bonchio, M.; Sartorel, A.; Scandola, F. *Inorg. Chem.* **2012**, *51*, 7324–7331.

(55) Vickers, J. W.; Lv, H. J.; Sumliner, J. M.; Zhu, G. B.; Luo, Z.; Musaev, D. G.; Geletii, Y. V.; Hill, C. L. *J. Am. Chem. Soc.* **2013**, *135*, 14110–14118.

(56) Lv, H.; Song, J.; Geletii, Y. V.; Vickers, J. W.; Sumliner, J. M.; Musaev, D. G.; Kögerler, P.; Zhuk, P. F.; Bacsa, J.; Zhu, G.; Hill, C. L. *J. Am. Chem. Soc.* **2014**, *136*, 9268–9271.

(57) Folkman, S. J.; Kirner, J. T.; Finke, R. G. *Inorg. Chem.* **2016**, *55*, 5343–5355.

(58) Folkman, S. J.; Finke, R. G. *ACS Catal.* **2017**, *7*, 7–16.

(59) Kanan, M. W.; Nocera, D. G. *Science* **2008**, *321*, 1072–1075.

(60) Taube, H. *Chem. Rev.* **1952**, *50*, 69–126.

2 | Structure dependence on the activation of molecular iridium precatalysts for the water oxidation reaction

Water oxidation using Ir-based complexes is a well-established electrochemical reaction. However, the carbon backbone of the iridium complex is often oxidized under catalytic circumstances yielding ill-defined active species. In this work, a comparison is made between two similar pyridyl-triazolylidene iridium complexes for their electrochemical water oxidation behavior. The proton in the IrL_1L_2 is replaced by a methoxy moiety in IrL_1L_3. The activation behavior of iridium pyridyl-triazolylidene complexes with a Cp^* ligand is highly dependent on the substituents on the triazolylidene ring. Molecular complexes adsorbed on the working electrode are responsible for the water oxidation activity, whilst at the same time part of the ligand backbone is oxidized to carbon dioxide. The active species of both complexes are compared to benchmark systems. The ligands of the active species are partially oxidized but the catalysts still have a molecular nature.

"Miracles are not contrary to nature but only contrary to what we know about nature. "
St. Augustine

Submitted

2.1 Introduction

One of the challenges in the water oxidation reaction mediated by molecular catalysts is the determination which reaction intermediates are present and involved in the catalytic reaction. Mechanistic studies on water oxidation catalysts are typically carried out using sacrificial reagents such as sodium periodate or cerium ammonium nitrate. The use of sacrificial reagents to pinpoint the presence of reaction intermediates in particular has been successful in the case of the relatively robust ruthenium-based molecular catalysts.[1–5]

Studies with sacrificial reagents to pinpoint which reaction intermediates are present during catalysis typically have been less successful with iridium-based catalysts equipped with a pentamethylcyclopentadienyl ligand (Cp^{*-}), in particular since such iridium Cp* complexes typically are precursors rather than the true active species. While keeping the drawbacks of sacrificial oxidants discussed above in mind, the use of a chemical oxidant can be very useful in the isolation of catalytic intermediates, or to detect species that are en route to the catalytically active species. The group of Macchioni discovered that the Cp^{*-} ligand in a $[Cp^*Ir(bzpy)NO_3]$ complex (bzpy = 2-benzoylpyridine) is slowly oxidized in presence of sacrificial reagents in a 1:1 mixtures of acetone and water.[6] They used H_2O_2, cerium ammonium nitrate and $NaIO_4$ as oxidants and found three different species wherein the Cp* ligand has been partially oxidized. Based on the structures that Macchioni *et al.* have observed with NMR spectroscopy (Figure 2.1) it is believed that the first step in catalyst activation is the epoxidation of a Cp* C-C bond of Cp* via an Ir-oxo species. This species is further oxidized by addition of water to the epoxide species. The last intermediate that was detected in this catalyst activation study contains one ketone-moiety on

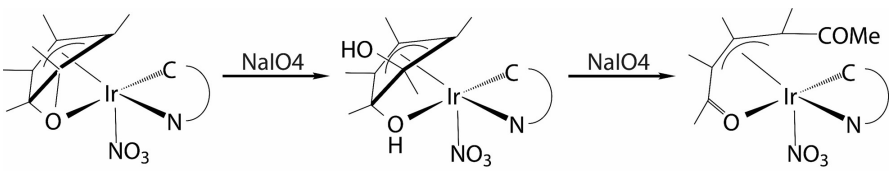

Figure 2.1: Oxidation of petnamethylcyclopentadienyl (Cp*) oxidation at a $[Cp^*Ir(bzpy)NO_3]$ complex upon treatment by periodate as chemical oxidant. Figure reporduced from [6].

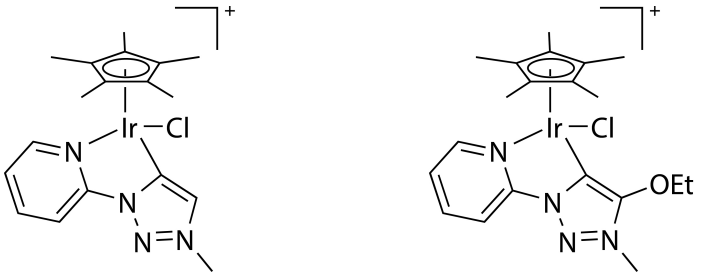

Figure 2.2: The structure of the complexes **1** and **2**.

the ring-opened aromatic remnant of Cp*, of which one is presumably coordinated to the Ir^{III} center. Further oxidation leads to the formation of acetic acid.

The complementary ligands present at iridium appear to be retained during at least the initial stages of catalysis. In the group of Albrecht, a wide variety of pyridyl-triazolylidene and other iridium complexes have been investigated for water oxidation using chemical oxidants to establish a structure-reactivity correlation.[7–13] Two catalysts that are particularly interesting in terms of activity are shown in Figure 2.2 and contain either an unmodified triazolylidene (complex **1**) or an ethoxy substituted triazolylidene ring (complex **2**). Upon treatment of these complexes with chemical oxidants, the rate of oxygen production increases over time, indicating that the catalysts need to be activated before water oxidation can take place. The results with cerium ammonium nitrate show that complex **2** activates more rapidly than complex **1**, which is attributed to the favorable electronic properties of complex **2**.[13] Furthermore both the maximum turnover number and turnover frequency seems to be limited by the amount of cerium present in solution and not by the maximum activity of the complexes.

The use of cerium ammonium nitrate as a sacrificial reagent is not ideal as it could interfere in the catalytic cycle. For example it has been reported that oxygen atom transfer can take place from the coordination sphere of cerium or periodate.[14–16] It has also been observed that cerium can participate in the catalytic cycle by direct coordination to the M-O bond.[17] Moreover it was shown that cerium can be incorporated in the *in situ* formed cataytic nanoparticles during water oxidation catalysis.[18] In light of the possible involvement of sacrificial reagents in this chapter electrochemical techniques are used to study the water oxidation reaction in pres-

ence of **1** and **2**. Such electrochemical tools provide reaction conditions that are much closer to an actual application in a electrochemical or photoelectrochemical water splitting device. In literature a few studies regarding iridium-based water oxidation catalysts have been reported wherein electrochemistry is combined with both *in situ* and *ex situ* techniques to investigate the nature of the catalytic systems. [19–24]

The complex $[Ir(Cp^*)(OH_2)_3]SO_4$ (**3**) has been investigated extensively using both chemical and electrochemical methods. Oxygen evolution starts at the moment that cerium ammonium nitrate is added to the solution containing **3**, indicating that the formation of an active species is extremely fast. An initial turnover frequency of 10.4 min^{-1} is observed with a 5 μM solution of **3** and 78 mM cerium ammonium nitrate at pH 0.89. The turnover frequency increases with catalyst concentration, indicating higher order reaction kinetics for **3**.[19]

Upon electrochemical oxidation of **3** at a graphite electrode in 0.1 M KNO_3 at pH 2.9, a catalytic wave is observed starting at 1.27 V *versus* RHE in the first scan of the cyclic voltammogram.[20] Upon repetitive cycling, a reversible peak redox couple grows at 1.05 V *versus* RHE, with a ΔE of 0.25 mV, which points to an adsorbed redox-active species. This absorbed material consists of amorphous iridium oxide and is called the blue layer. The increase in peak current with each consecutive scan is an indication that more material is deposited onto the working electrode during each scan. With the increase in peak current of the redox couple, the maximum current of the catalytic wave increases as well. After 10 cycles of cyclic voltammetry, 4.1 nmol cm^{-2} iridium is adsorbed as determined by the integration of the redox waves. Upon transfer of the deposited blue layer to a solution deprived of **3**, both the reversible redox couple and the catalytic wave are visible without a decrease in current. By measuring the mass increase using an electrochemical quartz crystal microbalance (EQCM), a total mass increase of 800 ng is observed over four consecutive scans. This suggests that in case of the formation of pure IrO_2, the total amount of electroactive iridium is 5.5%, whereas the remainder of the material is dormant.[21]

In contrast to **3**, which degrades to heterogeneous iridium oxide, the complex $[IrCp^*(pyalc)CF_3COO]$ (**4**, pyalc = 2-(2-pyridyl)-2-propanolate) was shown to produce a well-defined molecular catalyst for the water oxidation reaction.[21] Water oxidation was observed above 1.4 V *versus* RHE at pH 7 at a basal plane graphite electrode. The formation of dioxygen was identified using both RRDE techniques and a Clark electrode, whereas no deposit was observed by EQCM tech-

niques. After transferring the used electrode to an electrolyte solution deprived of catalyst, no catalytic activity was observed, confirming that no surface adsorption of active catalytic material had taken place.

The complex $[IrCp^*(Me_2NHC)(OH)_2]$ (**5**, Me_2NHC = N-dimethylimidazolin-2-ylidene) does form a surface deposit upon oxidation, which starts at 1.3 V *versus* RHE at pH 1.[22] The formation of dioxygen could be detected above 1.55 V *versus* RHE, while the presence of CO_2, a product of ligand degradation, was not observed.[23] *Ex situ* X-ray photoelectron spectroscopy showed the formed surface deposit does not contain large aggregates of iridium oxide and appears to consist of mononuclear molecular Ir centers.[22] *In situ* Raman spectroscopy illustrated the presence of a μ-oxo dimer in the reaction mixture under oxidative conditions, similar to what has been reported in the case of **4** by Crabtree and coworkers.[21]

The anionic complex $[IrCl_3(picolinate)(HOMe)]^-$ (**6**) displays a very long incubation time before it becomes active in the water oxidation reaction.[24] During this activation time, iridium oxide is formed on the electrode surface which is the true catalytic species during catalysis.

These different studies show that the role of the complementary ligands in iridium complexes have a dramatic effect on the homogeneity, the structure and the potential activity of the active species. The outstanding activity and longevity of the complexes **1** and **2** in the presence of sacrificial reagents prompted us to study these systems by electrochemical techniques and compare their results with the benchmark systems above.[13]

2.2 Experimental

2.2.1 Electrochemical methods

All experiments were performed on an Autolab PGSTAT 128N potentiostat. The experiments were carried out in a 25 ml glass cell in a three-electrode setup, using a gold working electrode (WE) (99.999%, Alfa Aesar). A gold wire (99.99%, Alfa Aesar) acted as counter electrode and the experiments were performed *versus* the reversible hydrogen electrode (RHE). The electrochemical cell was boiled twice in Millipore MilliQ water (>18.2 MΩ cm resistivity) prior to the experiment. The gold WE consisted of a disc (0.05 cm^2 geometrical surface area) and was used in a hanging meniscus configuration. The WE was cleaned by applying 10 V between the WE and a

graphite counter electrode for 30 s in a 10% H_2SO_4 (Sigma Aldrich 95%, ACS reagent) solution. This was followed by dipping the WE in a 6 M HCl (VWR chemicals 37%, Normapur) solution for 20 s. The electrode was flame annealed, followed by electrochemical polishing in 0.1 M $HClO_4$ (Merck, Suprapur), scanning between 0 and 1.75 V versus RHE for 200 cycles at 1 V s^{-1}. The electrolyte consisted of 0.1 M $HClO_4$ (Merck Suprapur, used as received) in Millipore MilliQ water (>18.2 MΩ cm resistivity) in which complex **1** or **2** was dissolved to make 0.5 mM solutions. The complexes were synthesised and characterized in the Albrecht group and made available for this investigation.[13] The electrochemical cell was purged with argon (Linde, 6.0) for at least 15 minutes prior to experiments.

2.2.2 OLEMS setup

The online electrochemical mass spectrometry (OLEMS) setup consisted of a hydrophobic porous tip (Kel-F with a Teflon plug), brought in close proximity to the WE. The gaseous products formed during electrochemistry were transferred through the tip into the mass spectrometer (Pfeiffer QMS200). An Ivium A06075 potentiostat was used to perform the electrochemical experiments.

A quadrupole mass spectrometer works on the principle of measuring the current of the ionized products impinging on the detector. The ion current of the mass spectrometer observed in the OLEMS is dependent on different factors:

- The rate of gas formation on the electrode surface
- The distance between the working electrode and the Teflon tip
- The rate of diffusion of the gas through the electrolyte
- The diffusion rate through the Teflon tip
- The ionizability of the gas

The distance between the working electrode and the tip is independent of the gas evolved, but might differ over different experiments. The gases in a quadrupole mass spectrometer are detected by means of ionization of the gaseous molecules. The ionizability of the gases differs between different molecules. The sensitivity for common gases are well-tabulated for use in ionizing pressure gauges, relative to nitrogen gas. Dioxygen has a sensitivity factor of 0.9, while carbon dioxide has a sensitivity factor of 0.7 versus N_2.[25] Thus the sensor is 1.25 times more

sensitive for dioxygen than for carbon dioxide. The diffusion of gases through the electrolyte solution is similar, 1.67×10^{-5} cm^2 s^{-1} for CO_2 and 2.01×10^{-5} cm^2 s^{-1} for O_2.[26] The distance between the electrode and the tip is small (10-100 μm) and should not influence the sensitivity for different gases significantly. Since the distance between the tip and the working electrode will differ over different experiments, the absolute ion current measured between different experiments cannot be compared and therefore all mass spectrometry data are displayed unitless.

2.2.3 Data processing in OLEMS

In an OLEMS experiment combined with cyclic voltammetry, two different datafiles are produced: electrochemical data and the mass spectrometer (MS) data. The MS data does not include the potential applied in a cyclic voltammetry. The potential can be generated manually by noting the start cycle in the MS data and using the scan rate of the CV. It has been observed that over very long experiments,the potential can drift due to discrepancies in the scan rate of the potentiostat. A method to generate the potential based on the start- and endtime of the different cycles is developed and used to couple the applied potential to the MS data.

In the MS data, the scans are separated and the time in each scan normalized. The potential is then generated using Equation 2.1,

$$E(t) = \frac{E_l - E_h}{\pi} \times \sin^{-1}\left(\sin\left((-)2\pi \times t + \frac{\pi}{2} + \pi\frac{E_s - E_l}{E_h - E_l}\right)\right) + E_l + \frac{E_h - E_l}{2} \quad (2.1)$$

where E_l and E_h are the lower and upper limits of the CV, E_s is the starting potential and t is the normalized time. The minus sign between parenthesis is only added if the scan starts in the negative direction and $E_s \neq E_l$ or $E_s \neq E_h$.

The first term ($\frac{E_l - E_h}{\pi}$) changes the amplitude of the sinusoidal wave to the vertex potential of the cyclic voltammogram. The last part ($E_l + \frac{E_h - E_l}{2}$) moves the equilibrium to the middle of the two vertices. The central part of Equation 2.1 ($\frac{\pi}{2} + \pi\frac{E_s - E_l}{E_h - E_l}$) moves the period of the sinusoidal wave to the starting potential of the experiment.

2.2.4 EQCM setup

The electrochemical quartz crystal microbalance consisted of a PEEK cell purchased from Autolab. The cell was deoxygenated with Ar (Linde, 6.0) prior to experiment. A gold working electrode (0.35 cm^{-2} geometric surface area and 0.39 cm^2 real surface area) on a quartz crystal was used as received. A gold counter electrode was used and the experiments were measured *versus* the reversible hydrogen electrode (RHE). The RHE consisted of a Pt wire embedded in glass. The gas outlet of the electrode was connected to a bubbler. This enabled the H_2 gas to remain at the electrode during experiments without the need to bubble hydrogen. Bubbling hydrogen gas at the reference electrode during the experiment can result in a high noise in Δf during experiments. Cyclic voltammetry were performed between 1.2 and 2.0 V *versus* RHE at pre-oxidized electrodes in 0.1 M $HClO_4$ at 10 mV s^{-1}. Chronoamperometry was performed at 1.7 and 1.8 V for 15 minutes.

The sensitivity coefficient of the quartz crystal (c_f) was determined by deposition of $Pb(NO_3)_2$. An electrolyte solution containing 10 mM $Pb(NO_3)_2$ and 0.1 M $HClO_4$ was prepared. Cyclic voltammetry at 100 mV s^{-1} gave the relationship between the Δf and the amount of Pb deposited onto the electrode, calculated from the current observed during cyclic voltammetry, assuming 100% faradaic efficiency towards Pb deposition. The sensitivity coefficient was determined to be 1.26×10^{-8} g cm^{-2} Hz^{-1} (Figure 2.3).

2.2.5 XPS

The XPS measurements were carried out with a Thermo Scientific K-Alpha, equipped with a monochromatic small-spot X-ray source and a 180° double focusing hemispherical analyzer with a 128-channel detector. Spectra were obtained using an aluminium anode (Al Kα = 1486.6 eV) operating at 72 W and a spot size of 400µm. Survey scans were measured at a constant pass energy of 200 eV and region scans at 50 eV. The background pressure was 2×10^{-8} mbar and during measurement 4×10^{-7} mbar argon because of charge compensation.

Samples for XPS were prepared by chronoamperometry in 0.1 M $HClO_4$ at pH 1 with 0.5 mM solutions of **1**, using EQCM gold working electrodes at 1.8 V *versus* RHE for 1, 2, 5 and 10 minutes with a gold counter electrode.

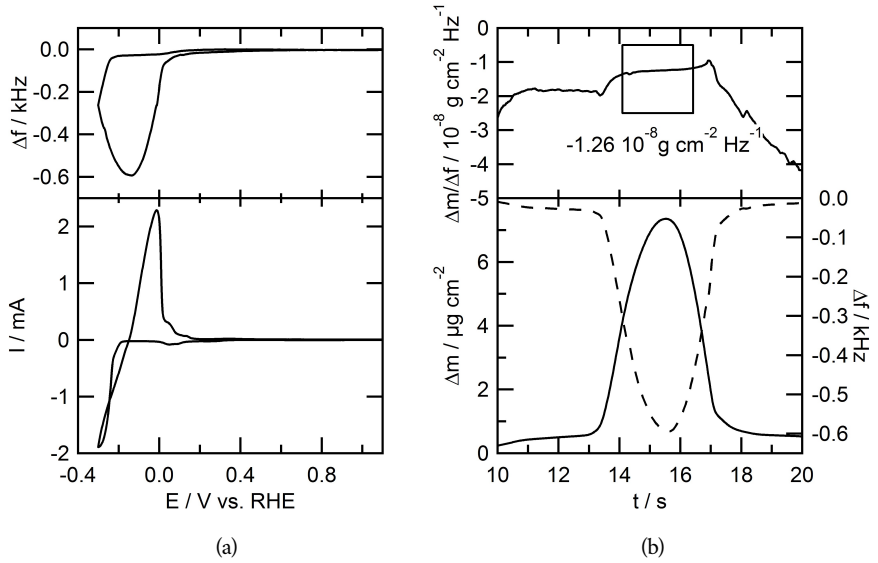

Figure 2.3: Calibration of the EQCM by bulk deposition of $PbNO_3$. a) The bottom panel shows the cyclic voltammogram of a 10 mM $PbNO_3$ solution in 0.1 M $HClO_4$ electrolyte solution at 100 mV s^{-1} on a gold electrode (1.5 cm^2 geometric surface area). The top panel shows the corresponding frequency change measured during the cyclic voltammetry. b) The bottom panel shows the frequency (dotted line) and mass change (solid line) between 0.1 to -0.3 and back to 0.1 V in time. The mass change is calculated from the current assuming 100% faradaic efficiency for the deposition of Pb . The top panel shows the sensitivity coefficient c_f which is averaged over the data points highlighted by the box.

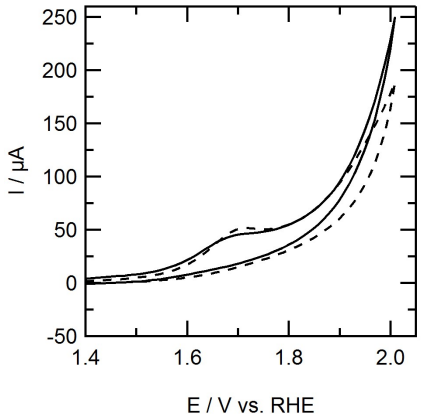

Figure 2.4: Fifth scan of cyclic voltammetry on a Au electrode (0.050 cm^2 in 0.1 M $HClO_4$ electrolyte solution) with 0.5 mM of **1** (solid line) and **2** (dotted line) in solution at pH 1 at 100 mV s^{-1}. The oxidative regime of the fifth scan between 1.4 and 2.0 V *versus* RHE is displayed.

2.2.6 XAS

X-ray absorption spectra were collected at the iridium L_3-edge (11215 eV) on the EXAFS station (BM26A) of the Dutch-Belgian beamline (DUBBLE)[27] at the European Synchrotron Radiation Facility (ESRF) in Grenoble, France. The solid benchmark materials were diluted with boron nitride and measured as pressed pellets in the transmission mode; 2 scans were averaged together to improve the signal-to-noise ratio. The samples were also recorded in the transmission mode and 6 - 8 scans were averaged. The EXAFS spectra were processed using Viper[28] and simulations were performed in EXCURVE.[29, 30] Samples were prepared by oxidizing graphite electrodes at 2.0 V *versus* RHE for 10 minutes in 1 mM solutions of **5** in 0.1 M $HClO_4$.

2.3 Results

The redox processes occurring in the presence of complexes **1** and **2** were investigated with cyclic voltammetry. In this study the working electrode is in a hanging meniscus configuration, meaning the electrode approaches the electrolyte from the top. Any solid material formed in proximity of the electrode which is not adsorbed will precipitate into the electrolyte and sink to the bottom

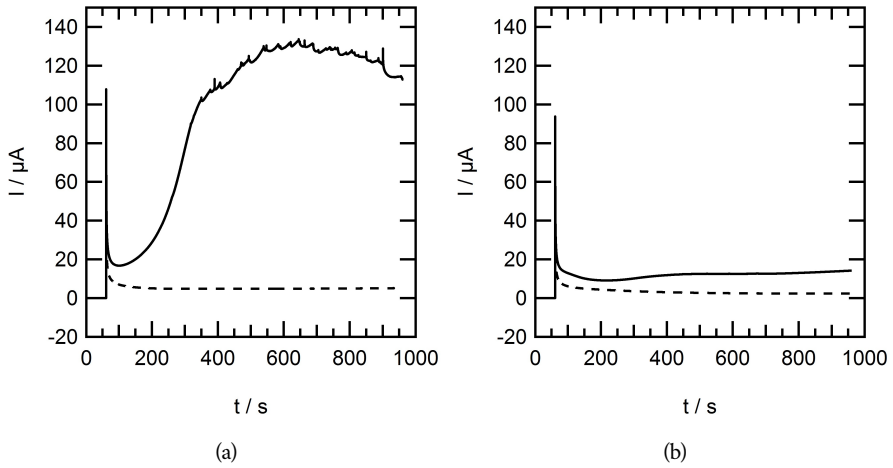

Figure 2.5: Chronoamperometry of 0.5 mM solutions of a) complex **1** and b) complex **1** at a gold electrode while applying 1.7 V (dotted line) and 1.8 V (solid line) *versus* RHE in a 0.1 M $HClO_4$ electrolyte solution. The lower potential region (0.7 to 1.4 V) is omitted for clarity.

of the electrochemical cell. The oxidation of gold, in absence of catalyst observed between 1.2 and 1.6 V, is not visible in the cyclic voltammograms. The reduction of the formed gold oxide is observed between 1.2 and 1.0 V, which is typical for a gold electrode in $HClO_4$ solution. Cyclic voltammetry of 0.5 mM solutions of **1** and **2** at a gold working electrode in 0.1 M $HClO_4$ was performed for 5 scans at 100 mV s^{-1} between 0.7 and 2.0 V *versus* RHE (fifth scan displayed in Figure 2.4). In both the cyclic voltammograms of **1** and **2**, an oxidative peak is observed at 1.7 V. This oxidative peak is most likely due to redox events of the complexes, but in part may also be caused by further oxidation of the gold working electrode.[31–42] Between 1.8 and 2.0 V, both complexes show a catalytic current which increases with the applied potential. With 220 µA *versus* 190 µA at 2 V *versus* RHE, the maximum current observed with complex **1** present in solution is higher than with complex **2** in solution. The activity of complex **1** increases from 180 to 220 µA at 2.0 V over 5 consecutive scans, whereas in the cyclic voltammogram with complex **2** in solution identical currents over 5 scans are observed. The oxidative wave at 1.7 V is present in all scans for both complexes.

Chronoamperometry was performed at 1.7 V to investigate the nature of the oxidation event

and at 1.8 V to investigate the activity of the complexes for water oxidation in a hanging meniscus configuration (Figure 2.5). At an applied potential of 1.7 V *versus* RHE little current is observed for both complexes (< 5 μA), indicating that little to no water oxidation activity takes place. At 1.8 V both complexes show an increase in current over time. In chronoamperometry experiments with complex **1** present in the electrolyte solution a minimum current after 40 seconds of amperometry is observed. Between 40 and 300 seconds the current increases, which is probably due to the activation of the complex. After 300 seconds the current stabilizes around 120 μA. For complex **2** the current goes through a minimum after 120 seconds of amperometry. An increase in current observed, reaching a final current of 14 μA after 900 seconds of amperometry. With complex **2** in solution, less current is observed than with complex **1** in the time frame of the experiment, which is in agreement with the maximum activity of both complexes at 2.0 V in cyclic voltammetry. The significant increase in current over time suggests that activation of the catalyst has taken place, but may also point to formation of a surface deposit. This is further investigated with EQCM.

In these EQCM experiments, a quartz crystal with a 200 nm layer of Au (0.35 cm^2 geometric surface area) is oscillated at 6 MHz. The oscillation frequency of the quartz crystal is directly related to the mass of the crystal, including the Au layer. This allows one to accurately determine the mass changes of the electrode by recording the frequency of oscillation during an electrochemistry experiment. It is important to note here that beside small changes in mass, also changes in the hydrophobicity have a strong effect on the oscillation frequency. Local changes in hydrophobicity are to be expected when the solution becomes saturated in dioxygen and gas bubbles start to form.[43]

In the cyclic voltammogram in the EQCM setup, the working electrode is situated at the bottom of the electrochemical cell. This is in contrast to the experiments described above, where the working electrode was used in a hanging meniscus configuration. One of the drawbacks of the use of gold electrodes in general and specifically in combination with the EQCM is gold oxidation and reduction chemistry, which may influence the electrochemical behavior of the complexes under study. In particular the oxidation of gold has a dramatic effect on the frequency of the quartz crystal. Upon prolonged cycling in $HClO_4$ electrolyte, this might lead to the destruction of the EQCM electrode altogether. This can be circumvented by keeping the potential either above

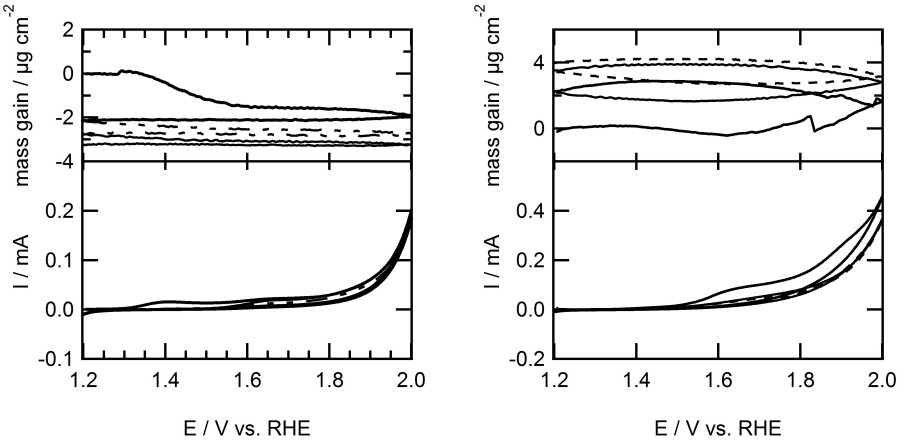

Figure 2.6: Cyclic voltammograms of 0.5 mM solutions of **1** (a) and **2** (b) in 0.1 M $HClO_4$ at 10 mV s^{-1} (bottom) and the potential-dependent mass gain, calculated from the changes of oscillation frequency of the quartz crystal-working electrode assembly.

or below 1.2 V *versus* RHE during an experiment, limiting the potential window for investigation.

There are several examples where EQCM is used to investigate the formation of a surface deposit. While oxidizing water at a gold electrode using **5**, a deposition is formed at the gold electrode. [22] The oxidation was performed in 0.1 M Na_2SO_4 electrolyte between 1.25 and 2.1 *versus* RHE at 10 mV s^{-1}. At pH 1 a mass increase of 3 µg cm^{-2} was reported over the course of three scans. This surface deposit is unstable in electrolytes without any complex present. Also in cyclic voltammetry experiments at low potential, a decrease in mass is observed.[22] Crabtree *et al* investigated several iridium-based complexes using EQCM as well.[21, 44] The complex $[Ir(Cp^*)(OH_2)_3]SO_4$ (**3**) forms the so-called blue layer on the electrode surface, with a total mass increase on the quartz crystal of 0.75 µg. The blue layer does not desorb from the electrode surface in absence of $[Ir(Cp^*)(OH_2)_3]SO_4$ in the electrolyte solution. In contrast to **3**, the complex $[Ir(Cp^*)(pyalc)(CF_3COO)]$ (**4**) does not show any deposit at all, suggesting that the active species in the latter is a truly homogeneous catalyst.

The cyclic voltammogram of complex **1** shows an oxidation event between 1.3 and 1.5 with

a peak current of 15 μA in the first scan in the EQCM configuration at a gold electrode in 0.1 M $HClO_4$ electrolyte at 10 mV s^{-1}. A second oxidative peak is observed at 1.65 V, with a peak current of 21 μA. This is followed by a faradaic wave, starting at 1.75 V and reaching a maximum current of 185 μA at 2.0 V. In the backward scan, a reductive wave is observed between 1.3 and 1.2 V, reaching a maximum current of -10 μA at 1.2 V. In the second and third scan, the first oxidation wave between 1.3 and 1.5 V is no longer observed and the peak current of the oxidation event at 1.65 V decreases in current. The catalytic current increases with each consecutive scan. At 2.0 V, the current is 180 μA in the second scan and 200 μA in the third scan. The QCM data appears to point to a decrease in mass of the electrode assembly over the course of the experiment, which is most likely to due hydrophobicity effects by formation of oxygen bubbles.

In the first scan of the cyclic voltammogram of complex **2**, an oxidation event is observed starting at 1.5 V with a peak current of current of 85 μA at 1.65 V. The oxidative peak is followed by a faradaic wave that increases from 1.75 to 2.0 V to a maximum current of 460 μA. In the backward scan a reductive wave is observed between 1.25 and 1.2 V. In the second and third scan the oxidative peak at 1.6 V is no longer visible and the current of the catalytic wave decreases to roughly 370 μA. The reductive wave between 1.25 and 1.2 V is still visible in the second and third backward scan. The QCM response corresponding to the cyclic voltammogram in the first scan shows an increase in mass between 1.6 to 2.0 V, which keeps increasing in the backward scan to 1.5 V leading to a total mass gain of 3.3 μg cm^{-2}. A subsequent decrease in mass of 1.2 μg cm^{-2} is observed between 1.5 and 1.2 V and at the start of the second scan up to 1.55 V. At 1.55 V the mass of the electrode starts increasing again and at 1.75 V in the backward scan it stabilizes at a mass gain of 2.1 μg cm^{-2}. The mass decreases again at 1.35 V in the backward scan until 1.55 V is reached in the forward scan in the third cycle with a total decrease of 1.2 μg cm^{-2}. Between 1.8 V in the forward scan and 1.7 V in the backward scan, the mass increases another 1.3 μg cm^{-2}. Finally, between 1.4 and 1.2 V of the third backward scan, a small decrease of 0.2 μg cm^{-2} is observed, leading to a total mass increase of 3.8 μg cm^{-2} over three scans.

Both complex **1** and **2** form a deposit on the electrode surface under chronoamperometric conditions at 1.8 V *versus* RHE (Figure 2.7). The formation of the surface deposit is accompanied with an increase in current. Accumulation of material on the working electrode starts the moment 1.8 V is being applied. In case of a 0.5 mM solution of complex **1** the total amount of

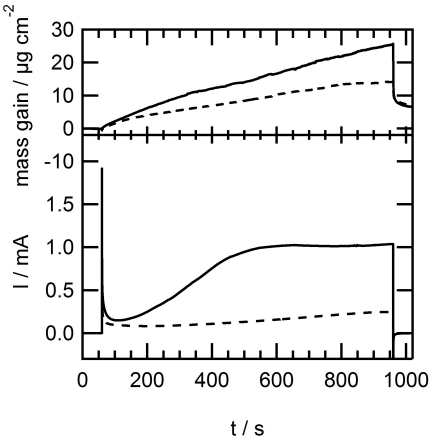

Figure 2.7: Bottom: chronoamperometry at 1.8 V at a Au electrode (0.39 cm^2) in a 0.5 mM solution complex **1** (solid line) or **2** (dotted line) and 0.1 M $HClO_4$. Top: The corresponding mass change as calculated from the frequency change recorded by EQCM.

material deposited after 15 minutes of amperometry is 10 µg cm^{-2}. For an equimolar solution of complex **2** less deposition is observed: 5.5 µg cm^{-2}. The chronoamperometry at 1.8 V of complex **1** shows an increase in current, until after 500 seconds of oxidation, the current stabilizes at 1 mA. An increase in current is observed upon oxidation of complex **2** as well, but it does not stabilize and after 15 minutes of oxidation, only 250 µA current is obtained. This suggests that complex **1** is activated quicker than complex **2** at a gold electrode in 0.1 M $HClO_4$ at 1.8 V. After oxidation, the potential is returned to 0.7 V, resulting in an apparent mass loss of approximately 50%, which may be due to changes in the hydrophobicity of the local electrolyte. Another explanation could be the loss of material from the electrode, which was observed previously with very similar IrCp* complexes including **5**.[21, 22]

To investigate whether the complexes or the surface deposits are truly active water oxidation catalysts, the gaseous products are analyzed by OLEMS. Apart from the formation of dioxygen, formation of CO_2 is to be expected in case the ligands (*e.g.* Cp*, see Figure 2.2) are oxidized during catalysis. Linear sweep voltammetry in combination with mass spectrometry shows the formation of both oxygen and carbon dioxide for both complexes, as is displayed in Figure 2.8.

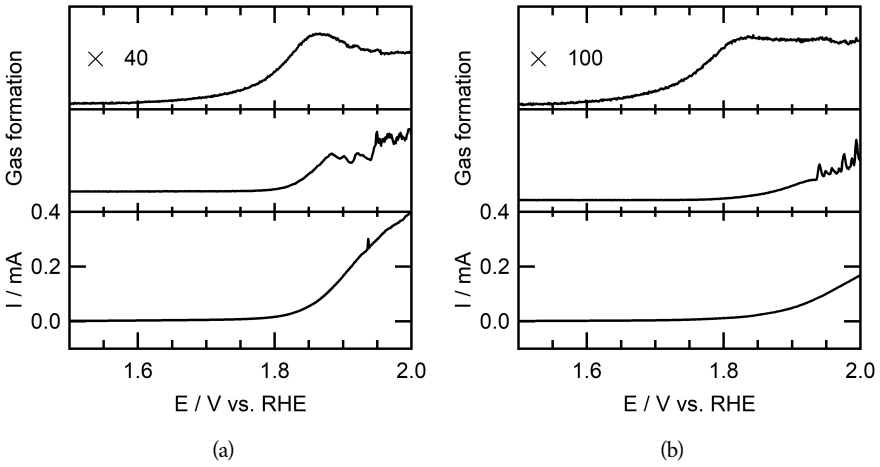

Figure 2.8: a) Linear sweep voltammogram of a 0.5 mM solution of **1** (bottom panel) in 0.1 M $HClO_4$ at 1 mV s^{-1} while tracking the production of CO_2 (top panel) and O_2 (middle panel). The top panel has been magnified 30 times for clarity. b) Cyclic voltammogram of a 0.5 mM solution of **2** (bottom panel) in 0.1 M $HClO_4$ at 1 mV s^{-1} while tracking the production of CO_2 (top panel) and O_2 (middle panel) in 0.1 M $HClO_4$. The top panel has been magnified 20 times for clarity.

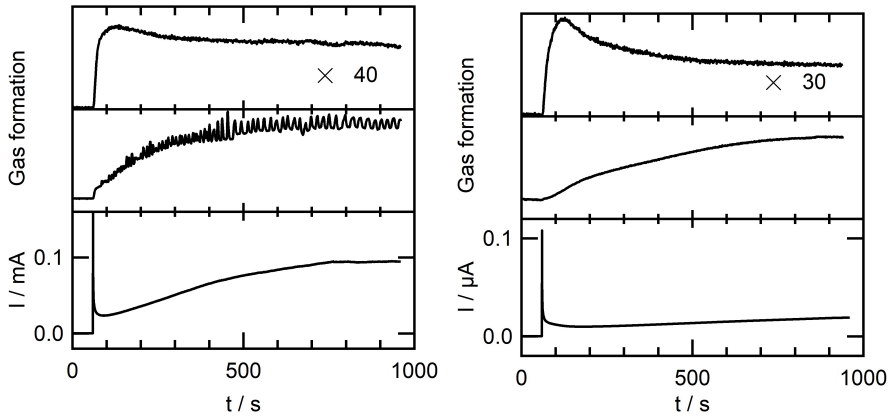

Figure 2.9: a) Chronoamperometry at 1.8 V *versus* RHE of complex **1** (bottom panel) while tracking the production of CO_2 (top panel) and O_2 (middle panel) in 0.1 M $HClO_4$. b) Chronoamperometry at 1.8 V *versus* RHE of complex **2** (bottom panel) while tracking the production of CO_2 (top panel) and O_2 (middle panel) in 0.1 M $HClO_4$.

With complex **1** in solution, carbon dioxide formation starts at 1.6 V . A maximum in rate of carbon dioxide formation is observed at 1.85 V, after which it decreases and eventually stabilizes at 1.95 V. Oxygen formation starts at 1.8 V which is at a significantly higher potential than the first burst of CO_2. At 1.88 V, the oxygen mass trace starts spiking, which points to the formation of gas bubbles at the surface of the electrode. The observed ion current for oxygen is two orders of magnitude higher than the ion current of carbon dioxide.

Complex **2** produces carbon dioxide beyond 1.55 V as is observed from the linear sweep voltammogram (Figure 2.8b). Evolution of oxygen starts at 1.8 V. In the oxygen trace, the spiky signal associated with bubble formation is observed beyond 1.95 V. The ion current for oxygen in this case is approximately 40 times higher than the ion current for CO_2.

In situ mass spectrometry in combination with chronoamperometry shows that complex **1** produces large amounts of dioxygen at the moment when an oxidizing potential is applied, whereas the activation of complex **2** to an active species takes a considerable longer reaction time (see Figure 2.9). The observed current in chronoamperometry with **1** in solution has a minimum

of 23 μA after 30 s and increases to 94 μA after 700 s of oxidation at 1.8 V where it stabilizes. In the chronoamperometry of **2**, the current goes through a minimum current of 9.9 μA after 120 seconds of oxidation and from there on increases up to 19 μA until the experiment was stopped at 15 minutes. The oxygen traces follow the current profiles of **1** and **2** exactly, apart from the spikes due to bubble formation in the case of **1**. Whereas evolution of dioxygen is sluggish at first in the case of complex **2**, an immediate burst of CO_2 is detected for both complex **1** and **2** upon applying a 1.8 V potential. After 70 seconds, the CO_2 evolution rate stabilizes upon oxidation of complex **1**. Complex **2** also evolves CO_2, with a peak at 60 seconds. The CO_2 evolution rate slowly decays and stabilizes after 400 seconds. The ion current observed for CO_2 is approximately 40 times lower than the O_2 formation, both in case of complex **1** and complex **2**.

In order to further investigate the structure of the active surface deposit, X-ray Photoelectron Spectroscopy (XPS) was measured of the gold electrode *ex situ* after water oxidation in the presence of complex **1**. Water oxidation was performed by amperometry at 1.8 V *versus* RHE in a 0.1 M $HClO_4$ and 0.5 mM solution of complex **1**. The electrode was taken out of the electrolyte and rinsed carefully with water. Different oxidation times from 1 to 10 minutes were used to track the evolution of the deposit.

Since XPS is a surface sensitive technique, the intensity of the Au XPS peaks should decrease as more material is deposited on the electrode surface (Figure 2.10a). The Au 4f peak is observed at 84.1 eV. This peak indeed decreases in intensity with increasing oxidation time, confirming that a layer of material has covered the gold electrode during the deposition experiment. The gold peak decreased to 10 percent of the initial intensity after 1 minute of oxidation.

The binding energy of 4f electrons in iridium is expected between 60.5 and 61 eV for metallic Ir, and expected up to 65 eV for highly oxidized iridium species such as $KIrCl_5NO$.[45] The binding energy of the 4f electrons in the molecular water oxidation complex **4** is found at 62.4 eV. [46, 47] The XPS spectrum for the gold electrode with the oxidized complex **1** shows a peak at 62.4 eV (Figure 2.10b. The intensity of the XPS sample correlates well with the oxidation time and amount of material deposited on the electrode.

In our group, the complex $[IrCl_3(pic)(MeOH)]^-$ (**6** - pic = picolinate) was determined to be a pre-catalyst for water oxidation. [24] The complex was degraded upon oxidation and an activated process is observed. An XPS analysis of the deposition after water oxidation catalysis shows the

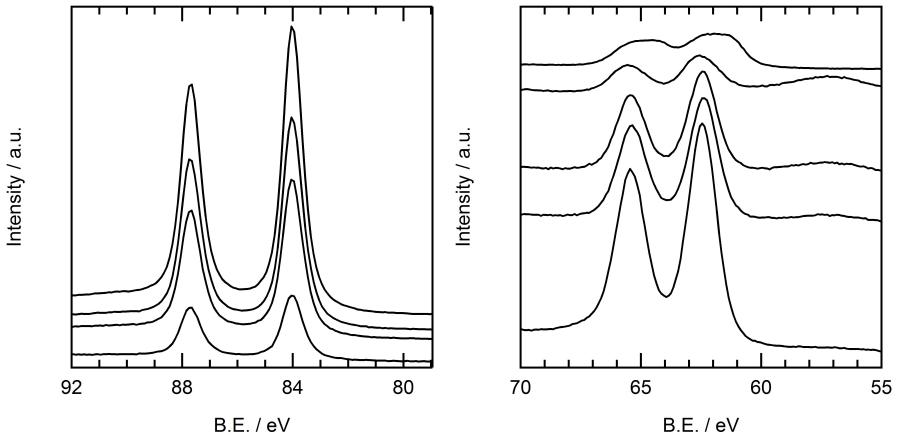

Figure 2.10: a) X-ray photoelectron spectra in the Au 4f region. From top to bottom the surface deposit on the gold electrode after 1, 3, 5 and 10 minutes of oxidation at 1.8 V *versus* RHE is displayed. b) X-ray photoelectron spectra in the Ir 4f region. The top trace is the powdered form of **1**, the rest from top to bottom is the surface deposit on the gold electrode after 1, 3, 5 and 10 minutes of oxidation at 1.8 V *versus* RHE.

Ir 4f electrons have a binding energy of 62.0 V. This is close to the values of benchmark Ir_2O_3, which are found at roughly 61.8 eV.

The surface deposit formed when complex **5** is oxidized has also been investigated using XPS.[22] The XPS spectrum shows the binding energy of the Ir 4f electrons is 62.2 eV, which is somewhat lower than was observed for activated **1** and activated **4**. Verification whether the deposit of complex **5** contains molecular structures, or is the path to formation of iridium oxide was obtained by extended X-ray absorption fine structure (EXAFS) analysis.

In EXAFS, among others the distance between the iridium center and the atoms in its direct environment can be investigated. The bond length between the iridium and its neighbors is indicative of the oxidation state of iridium and the type of atom that is present in the first coordination sphere. For an Ir-C bond, a longer bond length is expected compared to an Ir-O bond. In this investigation, the surface deposits of **5** were investigated and compared to the parent complex and benchmark IrO_2, as displayed in Figure 2.11 and Table 2.1. Complex **5** (1 mM in 0.1 M $HClO_4$ electrolyte) was oxidized at graphite foil at a range of potentials: 1.1 V, 1.3 V, 1.5 V, 1.7 V, 1.9 V and 2.0 V *versus* RHE for 5 minutes. In the parent complex, the measured bond length between the Ir center and its closest neighbor is 2.08 Å. The Ir-O bond length in IrO_2 is determined to be 1.96 Å. Oxidizing complex **5** at potentials between 1.1 and 1.5 V bond lengths between 2.04 and 2.11 Å are observed. Oxidizing the complex between 1.5 and 2.0 V decreases the bond length to 2.00-2.04 Å. The bond lengths found in case of **5** is still higher than the bond length found for IrO_2. In contrast to IrO_2, no signs pointing to short iridium-iridium distances have been observed in case of oxidized **5**.

2.4 Discussion

In contrast to electrochemical oxidation of **4**, deposits are formed on the electrode surface upon oxidation of complexes **1** and **2**. Whereas no deposition appears to be formed in case of **1** in cyclic voltammetry mode (Figure 2.6), a considerable large change in frequency in EQCM is observed compared to complex **2** in amperometry mode. It is not straightforward to interpret these data. The changes in frequency appear to be strongly related to the precise reaction conditions as well as the catalyst structure in ways we do not yet fully understand.[44] Moreover changes in the local hydrophobicity caused by bubble formation result in QCM frequency changes as well. This

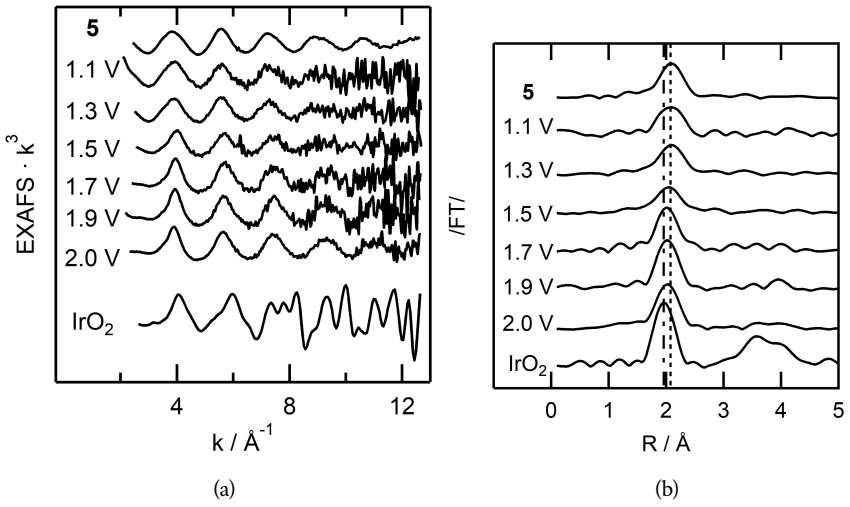

Figure 2.11: a) k^3 weighted iridium L_3 edge EXAFS and b) the modulus of the corresponding phase-corrected FT of 2 reference compounds and graphite electrodes exposed to different oxidizing potentials. From top to bottom: **5**, electrode oxidized at 1.1 V, 1.3 V, 1.5 V, 1.7 V, 1.9 V and 2.0 V, and benchmark IrO_2. The grey line and dotted grey line in b show the peak position of **5** and IrO_2 respectively.

Table 2.1: *Single shell simulations with C (carbon) or O (oxygen) for selected reference compounds and carbon electrodes exposed to certain potentials. The best fit index (C or O) is highlighted in bold.*

	C			O		
	Threshold energy(eV)	Number of atoms@distance (Å) and Debye–Waller factor ($2\sigma^2$, Å^2)	Fit index with k^3-weighting ($\times 10^3$)	Threshold energy(eV)	Number of atoms@distance (Å) and Debye–Waller factor ($2\sigma^2$, Å^2)	Fit index with k^3-weighting ($\times 10^3$)
5	-10.5607	5.7@2.147 (0.007)	**0.4903**	-14.6284	4.1@2.110 (0.009)	0.5555
1.1 V	-16.8836	6.8@2.139 (0.016)	**1.9858**	-19.6258	5.0@2.090 (0.019)	2.1008
1.3 V	-9.1949	5.9@2.146 (0.011)	**1.0433**	-12.1444	4.5@2.101 (0.014)	1.0929
1.5 V	-7.99290	5.0@2.100 (0.010)	**1.3133**	-10.597	4.0@2.053 (0.015)	1.3161
1.7 V	-7.3754	5.7@2.068 (0.004)	1.3189	-11.095	4.4@2.031 (0.015)	**1.3000**
1.9 V	-11.1800	6.1@2.075 (0.003)	1.2304	-15.147	4.6@2.039 (0.005)	**1.1833**
2.0 V	-9.08911	6.1@2.087 (0.005)	0.5581	-12.6264	4.5@2.049 (0.007)	**0.4625**
IrO_2	7.26908	6.6@2.010 (0.002)	3.2154	-12.1225	4.5@1.976 (0.014)	**3.3055**

may also explain the observed currents do not fully correlate with the amount of deposition on the electrode, albeit Crabtree *et al.* in case of the blue layer formed by the oxidation of **3** already showed that only part of the iridium sites in such an arrangement is electrochemically active in water oxidation catalysis.[44] Over the entire comparison, complex **1** does show a considerable higher current compared to complex **2**, which is accompanied by oxygen bubble formation - clearly visible in Figures 2.8 and 2.9 - and saturation effects. The OLEMS experiment in amperometry mode clearly suggests that complex **1** forms a highly active species for the oxygen evolution reaction much more rapidly than complex **2** This may be due to steric effects of the OEt moiety on the triazolylidene ligand. Possibly a dimeric structure as has been characterized in case of **4** and observed in the case of complex **5** is the active species. Alternatively one can imagine that complex **1** is a good catalyst itself, whereas complex **2** is too sterically hindered for fast turnovers until the Cp* has reacted away.

It is interesting to note that the iridium signals in the *ex situ* XPS spectra of the *ex situ* deposit obtained by oxidation of **1** matches very well with the μ-oxo bridged iridium(IV) dimer obtained in the group of Crabtree upon oxidation of **4**. Although the oxidation state of iridium in IrO_2 is also +IV, the signal for IrO_2 is found at a significant lower binding energy, allowing one to distinguish between molecular iridium(IV) species and iridium(IV) present in iridium oxide. In light of these binding energies very lengthy incubation times and the presence of redox waves that are typical for iridium oxide, our group has previously assigned the active species in case of complex **6** to iridium oxide. In term of XPS spectroscopy, deposits of complex **5** lie somewhat between those of **6** and **1**.

In EXAFS, the short binding distance between iridium and its first coordination shell of 1.96 Å recorded in case of IrO_2 gives a clear benchmark for the formation of IrO_2. The surface deposits of **5** oxidized at different potentials show clearly that the bond length in all adsorbed complexes is considerably longer (between 2.0 and 2.08 Å). Although the average bond length reduces upon an increase of the applied potential, this means complex **5** does produce larger aggregates of IrO_2 within the time frames wherein the experiments have been carried out. Between 1.1 and 1.5 V, the bond length is more in line with an Ir-C bond, whereas between 1.7 and 2.0 V the bond length decreases and modeling of the complex points more to displacement of carbon for oxygen in the first coordination sphere. This suggests that the complex does change structurally

during water oxidation, yet it is unclear what is the exact active species during water oxidation. No iridium - iridium interactions could be observed, which are very pronounced in the case of IrO_2 at higher $Å^{-1}$ Most likely the deposit of **5** is a single site molecular iridium species. The obtained EXAFS results did not allow us to distinguish between different atom-type within the coordination sphere of iridium, including powders of the precursors,[48] which refrain us from further X-ray absorption studies of *e.g.* complex **1**.

In general obtaining structure reactivity studies in the electrochemical water oxidation reaction in the presence of molecular iridium precursors has been very difficult. This study is no exception herein. It appears that every molecular iridium complex is active, with **6** being an exception, while the activity throughout an experiment appears to change continuously upon oxidation of the sample and appears to be strongly dependent on the applied reaction conditions. The choice for the Cp^* functionality, which role is most likely for that of a placeholder rather than it being directly present in the active species has not made things much easier. Only in very few cases catalytic intermediates have been identified in the reaction mixture. The μ-O bridged dimer reported by Crabtree *et al.* is an unique example,[21] whereas deposited **1** appears to have a similar electronic structure, based on XPS analysis. The large plethora of iridium catalysts for the water oxidation reaction have not led to well-defined design principles. This is in contrast to for example molecular ruthenium catalysts, for which clever proton shuttles to facilitate the water nucleophilic attack mechanism, and π-stacking strategies for binuclear oxygen-oxygen coupling reactions have been invented.[49] In case of iridium, modification of the ligands employed appear to be more useful to guide activation of the precatalyst to the true active species. In many cases this has led to formation of iridium oxide that is formed sooner or later under the catalytic conditions applied, whereas in other cases ill-defined catalytic species are formed that are categorized somewhere between a heterogeneous catalyst and a single-site species. In case of **4** this has led to a well-defined binuclear catalytic system that shows a very low onset for the water oxidation reaction at remarkable low iridium loadings. In terms of XPS analysis, it appears that the complexes **1** and **2** are relatively close to such species, albeit the electrochemistry of **1** and **2** is significantly more complex.

In the electrochemical iridium-based water oxidation reaction different types of active species can be identified (Figure 2.12). One is the formation of a well-defined molecular complex in so-

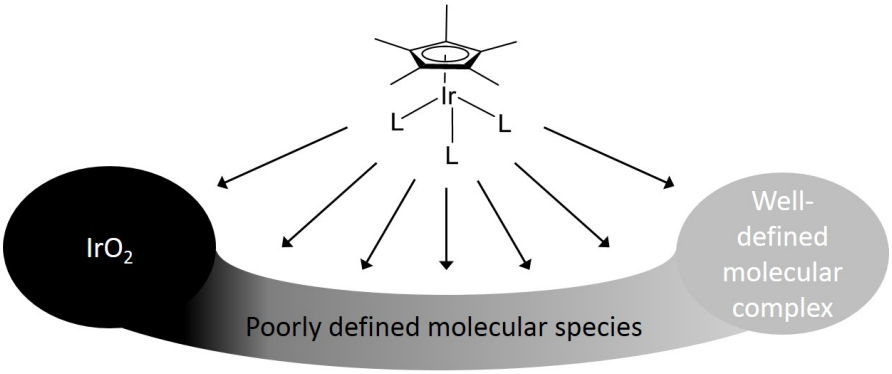

Figure 2.12: Active catalyst formation of various types of active species in the electrochemical water oxidation reaction.

lution, as was observed for complex **4**.[21] On the other side is the formation of iridium oxide as active catalyst, as was observed with the **3** and **6** precursors. In between these two extremes is a poorly defined region where the active site is a molecular complex which does form a surface deposit on the electrode. The complexes **1**, **2** and **5** are in this region. The challenge now lies in finding the prerequisites for complexes to be as much on the molecular side as possible, where ligand design already plays a large role.

The activation of pre-catalysts using the electrochemical methods presented in this work shows a different trend compared to a concerted study wherein a family of complexes including **1** an **2** was studied using the sacrificial reagent cerium ammonium nitrate.[7–13] The activation of complex **1** is faster under electrochemical conditions on all levels, but shows a remarkable slower reaction rate in the cerium ammonium nitrate driven water oxidation (1500 h^{-1} *versus* 2500 h^{-1} for complex **2**). Also it appears to activate much slower under these conditions. Where cerium ammonium nitrate and other sacrificial oxidants may be useful for the examination of intermediates and provide structural information on the catalyst, it does not always agree with results obtained with electrochemical methods. Therefore, one needs to be careful in designing catalytic experiments and in drawing conclusions from experiments in complicated reactions such as the water oxidation reaction.

2.5 Conclusions

Water oxidation has been achieved using pyridyl-triazolylidene iridium-based pre-catalysts **1** and **2**. The activation of these pre-catalysts involves the formation of a deposit on the surface of the Au working electrode.

Dioxygen and carbon dioxide formation was observed in voltammetric experiments, where the formation of CO_2 started at lower potentials than O_2. In chronoamperometric experiments, both O_2 and CO_2 formation start instantaneously upon applying an oxidizing potential in case of complex **1**, whereas the formation of O_2 is initially sluggish in case of complex **2**.

Activation of water oxidation catalysts can differ greatly with different means of oxidation. The observed trend in the cerium ammonium nitrate driven water oxidation reaction showed a remarkably different trend in activity than the electrochemical data presented here. This strongly suggests that the method of study in structure-activity relationships or structure-activation relationships do influence the results. Therefore it is best to use complementary techniques or at least apply a method of oxidation that is as close as possible to the final application.

2.6 References

(1) Bernet, L.; Lalrempuia, R.; Ghattas, W.; Mueller-Bunz, H.; Vigara, L.; Llobet, A.; Albrecht, M. *Chem. Commun.* **2011**, *47*, 8058.

(2) Gersten, S. W.; Samuels, G. J.; Meyer, T. J. *J. Am. Chem. Soc.* **1982**, *104*, 4029–4030.

(3) Wasylenko, D. J.; Ganesamoorthy, C.; Henderson, M. A.; Berlinguette, C. P. *Inorg. Chem.* **2011**, *50*, 3662–3672.

(4) Concepcion, J. J.; Jurss, J. W.; Norris, M. R.; Chen, Z.; Templeton, J. L.; Meyer, T. J. *Inorg. Chem.* **2010**, *49*, 1277–1279.

(5) Duan, L.; Bozoglian, F.; Mandal, S.; Stewart, B.; Privalov, T.; Llobet, A.; Sun, L. *Nat. Chem.* **2012**, *4*, 418–423.

(6) Zuccaccia, C.; Bellachioma, G.; Bortolini, O.; Bucci, A.; Savini, A.; Macchioni, A. *Chem. Eur. J.* **2014**, *20*, 3446–56.

(7) Lalrempuia, R.; McDaniel, N. D.; Müller-Bunz, H.; Bernhard, S.; Albrecht, M. *Angew. Chem. Int. Ed.* **2010**, *49*, 9765–9768.

(8) Petronilho, A.; Rahman, M.; Woods, J. A.; Al-Sayyed, H.; Müller-Bunz, H.; MacElroy, J. M. D.; Bernhard, S.; Albrecht, M. *Dalton T.* **2012**, *41*, 13074.

(9) Woods, J. A.; Lalrempuia, R.; Petronilho, A.; McDaniel, N. D.; Müller-Bunz, H.; Albrecht, M.; Bernhard, S. *Energ. Environ. Sci.* **2014**, *7*, 2316.

(10) Corbucci, I.; Petronilho, A.; Müller-Bunz, H.; Rocchigiani, L.; Albrecht, M.; Macchioni, A. *ACS Catal.* **2015**, *5*, 2714–2718.

(11) Navarro, M.; Li, M.; Müller-Bunz, H.; Bernhard, S.; Albrecht, M. *Chem. Eur. J.* **2016**, *22*, 6740–6745.

(12) Navarro, M.; Smith, C. A.; Li, M.; Bernhard, S.; Albrecht, M. *Chem. Eur. J.* **2018**, *24*, 6386–6398.

(13) Olivares, M.; van der Ham, C. J. M.; Li, M.; Müller-Bunz, H.; Verhoeven, M. W. G. M.; Niemantsverdriet, J. W.; Hetterscheid, D. G. H.; Bernhard, S.; Albrecht, M. *In preparation*.

(14) Hetterscheid, D. G. H.; Reek, J. N. H. *Eur. J. Inorg. Chem.* **2014**, 742–749.

(15) Wasylenko, D. J.; Ganesamoorthy, C.; Borau-Garcia, J.; Berlinguette, C. P. *Chem. Commun.* **2011**, *47*, 4249.

(16) Yoshida, M.; Masaoka, S.; Abe, J.; Sakai, K. *Chem. Asian J.* **2010**, *5*, 2369–2378.

(17) Codolà, Z.; Gómez, L.; Kleespies, S. T.; Que Jr, L.; Costas, M.; Lloret-Fillol, J. *Nat. Commun.* **2015**, *6*, 5865.

(18) Hong, D.; Murakami, M.; Yamada, Y.; Fukuzumi, S. *Energ. Environ. Sci.* **2012**, *5*, 5708–5716.

(19) Blakemore, J. D.; Schley, N. D.; Balcells, D.; Hull, J. F.; Olack, G. W.; Incarvito, C. D.; Eisenstein, O.; Brudvig, G. W.; Crabtree, R. H. *J. Am. Chem. Soc.* **2010**, *132*, 16017–16029.

(20) Blakemore, J. D.; Schley, N. D.; Olack, G. W.; Incarvito, C. D.; Brudvig, G. W.; Crabtree, R. H. *Chem. Sci.* **2011**, *2*, 94–98.

(21) Schley, N. D.; Blakemore, J. D.; Subbaiyan, N. K.; Incarvito, C. D.; D'Souza, F.; Crabtree, R. H.; Brudvig, G. W. *J. Am. Chem. Soc.* **2011**, *133*, 10473–10481.

(22) Hetterscheid, D. G. H.; van der Ham, C. J. M.; Diaz-Morales, O.; Verhoeven, M. W. G. M.; Longo, A.; Banerjee, D.; Niemantsverdriet, J. W.; Reek, J. N. H.; Feiters, M. C. *Phys. Chem. Chem. Phys.* **2016**, *18*, 10931–10940.

(23) Diaz-Morales, O.; Hersbach, T. J. P.; Hetterscheid, D. G. H.; Reek, J. N. H.; Koper, M. T. M. *J. Am. Chem. Soc.* **2014**, *136*, 10432–10439.

(24) Abril, P.; del Rio, M. P.; Tejel, C.; Verhoeven, T. W. G. M.; Niemantsverdriet, J. W.; Van der Ham, C. J. M.; Kottrup, K. G.; Hetterscheid, D. G. H. *ACS Catal.* **2016**, *6*, 7872–7875.

(25) Moore, J. H.; Davis, C. C.; Coplan, M. A.; Greer, S. C., *Building scientific apparatus: a practical guide to design and construction*, 1989, p 102.

(26) Lide, D. R., *CRC Handbook of Chemistry and Physics, 84th Edition, 2003-2004*, 2003; Vol. 53, p 2616.

(27) Nikitenko, S.; Beale, A. M.; van der Eerden, A. M. J.; Jacques, S. D. M.; Leynaud, O.; O'Brien, M. G.; Detollenaere, D.; Kaptein, R.; Weckhuysen, B. M.; Bras, W.; IUCr *J. Synchrotron Radiat.* **2008**, *15*, 632–640.

(28) Klementev, K. V. *J. Phys. D: Appl. Phys.* **2001**, *34*, 209–217.

(29) Gurman, S. J.; Binsted, N.; Ross, I. *J. Phys. C: Solid State Phys.* **1986**, *19*, 1845–1861.

(30) Gurman, S. J.; Binstedt, N.; Ross, I. *J. Phys. C: Solid State Phys.* **1984**, *17*, 143–151.

(31) Awad, M. I.; Ohsaka, T. *Journal of Power Sources* **2013**, *226*, 306–312.

(32) Burke, L. D.; O'Sullivan, J. F. *J. Electroanal. Chem.* **1990**, *285*, 195–207.

(33) Doyle, R. L.; Lyons, M. E. G. *J. Solid State Electr.* **2014**, *18*, 3271–3286.

(34) Baten, S. M. A.; Taylor, A. G.; Wilde, C. P. *Electrochim. Acta* **2008**, *53*, 6829–6834.

(35) Burke, L. D.; Lee, B. H. *J. Electroanal. Chem.* **1992**, *330*, 637–661.

(36) Burke, L. D.; Nugent, P. F. *Gold Bull.* **1997**, *30*, 43–53.

(37) Iotov, P. I.; Kalcheva, S. V. *Gold Bull.* **2001**, *34*, 95–103.

(38) Doménech-Carbó, A.; Sabaté, F.; Sabater, M. J. *J. Phys. Chem. C* **2018**, *122*, 10939–10947.

(39) Zou, S.; Burke, M. S.; Kast, M. G.; Fan, J.; Danilovic, N.; Boettcher, S. W. *Chem. Mater.* **2015**, *27*, 8011–8020.

(40) Burke, L. D.; Cunnane, V. J.; Lee, B. H. *J. Electrochem. Soc.* **1992**, *139*, 3–10.

(41) Cherevko, S.; Zeradjanin, A. R.; Topalov, A. A.; Kulyk, N.; Katsounaros, I.; Mayrhofer, K. J. J. *ChemCatChem* **2014**, *6*, 2219–2223.

(42) Klaus, S.; Trotochaud, L.; Cheng, M.-J.; Head-Gordon, M.; Bell, A. T. *ChemElectroChem* **2016**, *3*, 66–73.

(43) Hetterscheid, D. G. H. *Chem. Commun.* **2017**, *53*, 10622–10631.

(44) Blakemore, J. D.; Schley, N. D.; Kushner-Lenhoff, M. N.; Winter, A. M.; Souza, D.; Crabtree, R. H.; Brudvig, G. W. *Inorg. Chem.* **2012**, *51*, 7749–7763.

(45) Moulder, J. F.; Stickle, W. F.; Sobol, P. E.; Bomben, K. D. Handbook of X-ray Photoelectron Spectroscopy., 1995.

(46) Sharninghausen, L. S.; Sinha, S. B.; Shopov, D. Y.; Choi, B.; Mercado, B. Q.; Roy, X.; Balcells, D.; Brudvig, G. W.; Crabtree, R. H. *J. Am. Chem. Soc.* **2016**, *138*, 15917–15926.

(47) Hintermair, U.; Sheehan, S. W.; Parent, A. R.; Ess, D. H.; Richens, D. T.; Vaccaro, P. H.; Brudvig, G. W.; Crabtree, R. H. *J. Am. Chem. Soc.* **2013**, *135*, 10837–10551.

(48) Feiters, M. C.; Longo, A.; Banerjee, D.; van der Ham, C. J. M.; Hetterscheid, D. G. H. *J. Phys. Conf. Ser.* **2016**, *712*, 012059.

(49) Blakemore, J. D.; Crabtree, R. H.; Brudvig, G. W. *Chem. Rev.* **2015**, *115*, 12974–13005.

3 | Activation pathways taking place at molecular copper precatalysts for the oxygen evolution reaction

Abstract

The activation processes of the complex $[Cu^{II}(bdmpza)_2]$ (bdmpza$^-$ = bis(3,5-dimethyl-1H-pyrazol-1-yl)acetate) in the water oxidation reaction were investigated using cyclic voltammetry and chronoamperometry. Two different paths wherein CuO is formed were distinguished. $[Cu^{II}(bdmpza)_2]$ can be oxidized at high potentials to form CuO, which was observed by a slight increase in catalytic current over time in chronoamperommetry. When $[Cu^{II}(bdmpza)_2]$ is initially reduced at low potentials, a more active water oxidation catalyst is generated, yielding high catalytic currents from the moment a sufficient potential is applied. This work highlights the importance of catalyst pretreatment and the choice of the experimental conditions in water oxidation catalysis using copper complexes.

"Faith and reason are like two wings on which the human spirit rises to the contemplation of truth; and God has placed in the human heart a desire to know the truth"

St. John Paul II in *Fides et Ratio*

Published in: *Catal. Today* **2016***290,* 33-38

3.1 Introduction

The water oxidation reaction has been extensively studied in the presence of homogeneous water oxidation catalysts that predominantly are based on noble metals such as ruthenium [1–3] and iridium. [4–9] In particular in case of molecular ruthenium systems bearing bipyridine type ligands, mechanistic studies have provided the community with detailed insights how water oxidation catalysis occurs. [10–12] In case of other water oxidation catalysts the true active species turned out to be metal oxide deposits that were formed from their organometallic precursors under the harsh oxidative conditions applied. [13–16] In terms of atom abundance and economic viability, complexes that are based on first row transition metals are more interesting than their second and third row counterparts, albeit such systems typically do not operate well under acidic conditions. Due to substantial faster ligand dissociation kinetics at these first row transitions metals, control over the catalyst structure is considerably more cumbersome. Nevertheless, molecular catalysts in case of manganese,[17] iron,[18–20] cobalt[21] and since very recently copper[22–30] have been reported. Especially in case of the latter, ligand exchange kinetics are fast, and consequently several papers have appeared wherein copper oxides proved to be the competent catalytic species rather than their molecular precursors.[31–35] A fruitful strategy to prevent formation of copper oxides appears to lie with multi-denticity. [29] Nevertheless, also the copper bipyridine complexes, first reported by Mayer *et al.*, appear to react exclusively via molecular sites, [22, 23] suggesting that discrimination between homogeneous versus heterogeneous catalysis is much more complex. From early cobalt polyoxometallate water oxidation chemistry the scientific community has already learned that the formation of which type of catalytic species is formed can be largely dependent on the exact reaction conditions applied, especially in case of highly dynamic systems.[36–39]

Preliminary water oxidation studies in our lab in the presence of $[Cu^{II}(bdmpza)_2]$ ($bdmpza^-$ = bis(3,5-dimethyl-1H-pyrazol-1-yl)acetate, Figure 3.1), a structure similar to the aforementioned copper bipyridine system, revealed that the observed water oxidation activity is strongly dependent on the electrochemical pretreatment of the molecular catalyst, even though the eventual catalytic experiments were carried out under the exact same conditions. In light of the discussion whether catalysis occurs at a homogeneous versus heterogeneous species and how one can

control the activity of these catalytic species, the pretreatment dependence triggered us to investigate the catalyst activation pathways of $[Cu^{II}(bdmpza)_2]$ in detail. In this contribution we discuss two independent pathways to the formation of CuO, the true active species, wherein the observed reactivity is greatly dependent on the activation path.

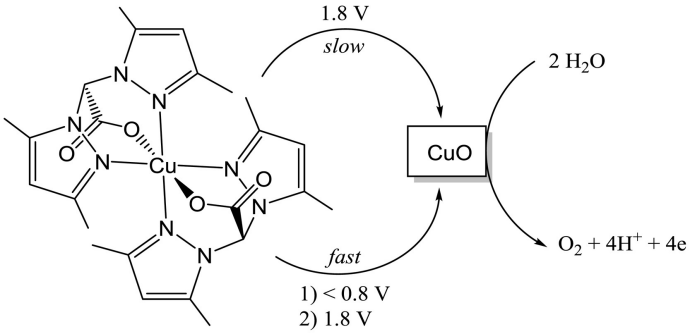

Figure 3.1: Paths of activation observed for $[Cu^{II}(bdmpza)_2]$.

3.2 Experimental

3.2.1 Materials

The bdmpzaNa ligand was synthesized by Tom van Dijkman according to literature procedure[40] and used as received. $Cu(OTf)_2$ (Alfa Aesar, 99%) was used as received.

NaOH (Merck, 99.9995%) was used as received. Electrolyte solutions were made using Millipore MilliQ water (>18.2 MΩ cm resistivity). Argon (Linde, 5.0) and hydrogen (Linde, 5.0) were used as received

3.2.2 Complex synthesis

$[Cu^{II}(bdmpza)_2]$ was obtained by dropwise addition of 0.33 mmol bdmpzaNa in 25 ml methanol to a solution of 0.33 mmol $Cu^{II}(OTf)_2$ in 25 ml methanol. After stirring for 30 minutes, part of the methanol was evaporated and diethyl ether was added to the reaction mixture to yield a blue-green precipitate overnight. The crystalline material was dried *in vacuo* and recrystallized from methanol at -20°C, yielding the complex $[Cu^{II}(bdmpza)_2]$. The infrared spectra of

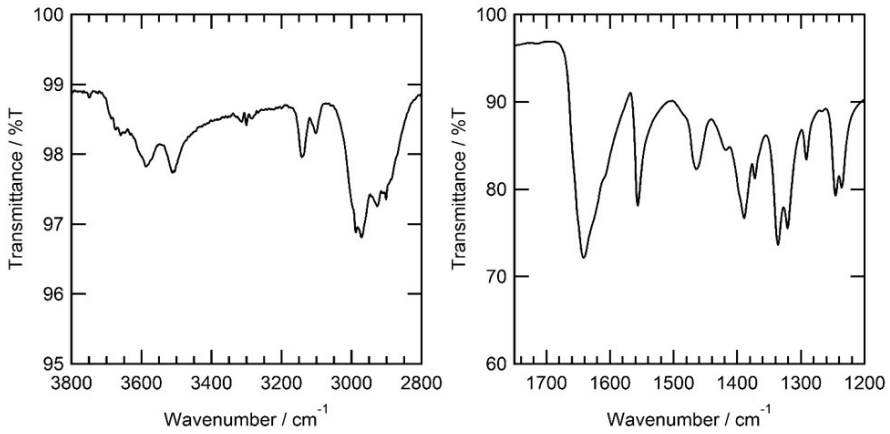

Figure 3.2: IR spectrum of $[Cu^{II}(bdmpza)_2]$, which shows characteristic vibrations: at $\tilde{\upsilon}$ = 1642 cm^{-1} (1645 cm^{-1}) [41] and $\tilde{\upsilon}$ = 1557 cm^{-1} (C-N, 1558 cm^{-1}) [41].

$[Cu^{II}(bdmpza)_2]$ are in good agreement with previous reported data (see Figure 3.2). [41] ESI MS m/z (calc):558.2 (558.2, $[M]^+$ 580.2 (580.2, $[M+Na]^+$), 612.2 (612.2, $[M+Na+MeOH]^+$).

3.2.3 Electrochemical methods

All experiments were performed on an Autolab PGSTAT 128N. All electrochemical experiments were performed in one-compartment 25 ml glass cells in a three-electrode setup, using a gold (Mateck, 99.999%) working electrode (WE). In all cases a gold wire (Mateck, 99.99%) was used as a counter electrode and all experiments were measured *versus* the reversible hydrogen electrode. The electrochemical cell was boiled twice in Millipore MilliQ water (>18.2 MΩ cm resistivity) prior to the experiment. The Au working electrode consisted of a disc (0.050 cm^2 geometric surface area) and was used in a hanging meniscus configuration. The WE was cleaned by applying 10 V between the WE and a graphite counter electrode for 30 s in a 10% H_2SO_4 solution. This was followed by dipping the WE in a 6 M HCl solution for 20 s. The electrode was flame annealed, followed by electrochemical polishing in 0.1 M $HClO_4$, while scanning between 0 and 1.75 V *versus* RHE for 200 cycles at 1 V s^{-1}. After drying the electrode *in vacuo* 5 µL of a 18 mM solution of $[Cu^{II}(bdmpza)_2]$ in ethanol was dropcasted onto the working electrode and dried in air. The electrolyte solutions were prepared from MilliQ water (>18.2 MΩ cm resistivity) and ≥99.9995%

NaOH obtained from Sigma-Aldrich.

The electrochemical quartz crystal microbalance (EQCM) experiments were performed in a 3 ml Teflon cell purchased from Autolab. As a working electrode, an Autolab EQCM electrode was used, wherein a 200 nm gold layer (0.35 cm^2) was deposited on a quartz crystal. Since the hydrogen bubbles of the RHE reference electrode disturbed the frequency during the EQCM measurements, a Pd/H_2 reference electrode was prepared by applying a potential of -4.0 V between the Pd wire and a platinum counter electrode for approximately 10 min. Prior to the experiment the potential of the Pd/H_2 electrode relative to the RHE was determined. All EQCM data were corrected to the RHE scale. The sensitivity coefficient (c_f) was determined to be 1.26×10^{-8} µg cm^{-2} Hz^{-1}, *c.f.* Figure 2.3 in chapter 2.

During the online electrochemical mass spectrometry (OLEMS) measurements the gaseous products formed at the working electrode were collected via a hydrophobic tip (KEL-F with a porous Teflon plug) in close proximity to the surface of the working electrode and analyzed in a Pfeiffer QMS 200 mass spectrometer. An Ivium A06075 potentiostat was used in combination with the OLEMS experiments. A detailed description of the OLEMS setup is available elsewhere. [42]

3.2.4 XPS

The XPS measurements were carried out with a Thermo Scientific K-Alpha, equipped with a monochromatic small-spot X-ray source and a 180° double focusing hemispherical analyzer with a 128-channel detector. Spectra were obtained using an aluminium anode (Al Kα = 1486.6 eV) operating at 72 W and a spot size of 400µm. Survey scans were measured at a constant pass energy of 200 eV and region scans at 50 eV. The background pressure was 2×10^{-8} mbar and during measurement 4 x 10^{-7} mbar Argon because of charge compensation.

Samples for XPS were prepared by chronoamperometry in 0.1 M NaOH at pH 13, using 0.8 cm^2 pyrolitic graphite discs as working electrodes. Prior to use, the electrodes were sanded with waterproof 2500 grit sandpaper. A total amount of 180 nmol $[Cu^{II}(bdmpza)_2]$ was dropcasted onto the electrodes and the discs were used in a hanging meniscus configuration.

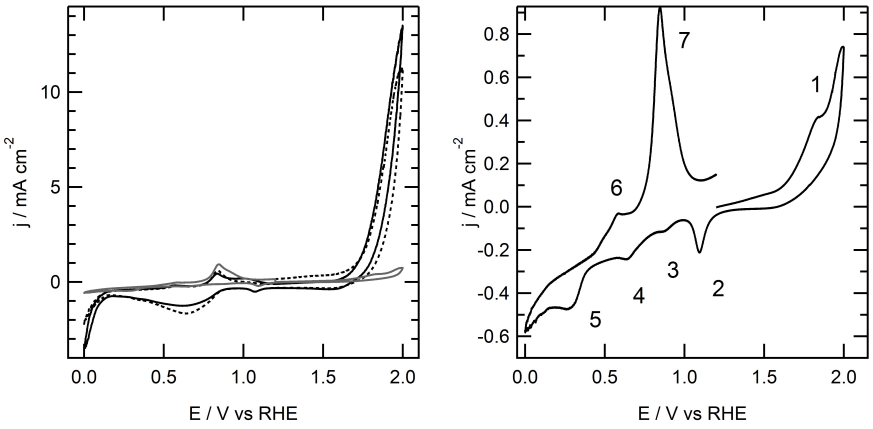

Figure 3.3: (a) The first three scans of a cyclic voltammetry experiment of $[Cu^{II}(bdmpza)_2]$ in 0.1 M NaOH at a 100 mV s^{-1} scan rate. The first scan of the cyclic voltammetry (grey line) is depicted in magnified view separately (b) from the 2nd (dotted black line) and 3rd scan (solid black line).

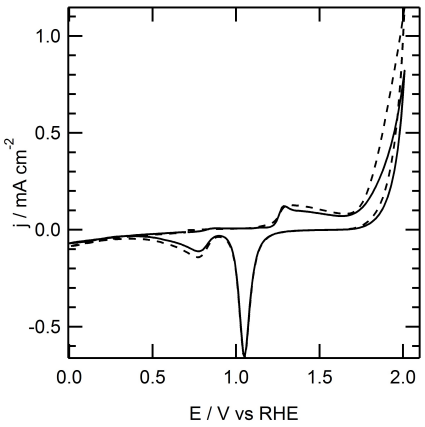

Figure 3.4: First (dotted line) and second (solid line) scan of a cyclic voltammogram of a Au WE in 0.1 M NaOH electrolyte solution at a scan rate of 100 mV s^{-1}.

3.3 Results

The bdmpza$^-$ ligands of [Cu^{II}(bdmpza)$_2$] are centrosymmetrically arranged around the copper ion, forming a trans-CuN_4O_2 complex, wherein the copper site is coordinatively saturated.[41] However, it is not unprecedented that one of the ligand arms of bdmpza$^-$ dissociates in favor of coordination of water,[43] providing an entry into catalysis at a molecular species. The redox chemistry of [Cu^{II}(bdmpza)$_2$] was explored by dropcasting the complex onto a gold working electrode (WE). Figure 3.3 shows the cyclic voltammogram of 90 nmol [Cu^{II}(bdmpza)$_2$] dropcasted onto a 0.050 cm^2 (geometric surface area) gold electrode in a 0.1 M aqueous NaOH solution at pH 13. The experiment was started at 1.2 V *versus* RHE and scanned towards positive potentials initially. In the first scan relatively little catalytic current is observed, which contrasts the second and third scans. Scanning the potential up to 2.0 V *versus* RHE resulted in a small peak (designated 1 in Figure 3.3b) in the cyclic voltammogram, which does not exceed the current displaying that of a blank gold electrode under the same conditions (see Figure 3.4).

While starting above 1.2 V *versus* RHE and scanning into a positive direction first or scanning in negative direction immediately does not result in changes in the reduction chemistry. Below 1.2 V a series of sharp reduction peaks (2-5 in Figure 3.3b) can be observed that lie on top of a

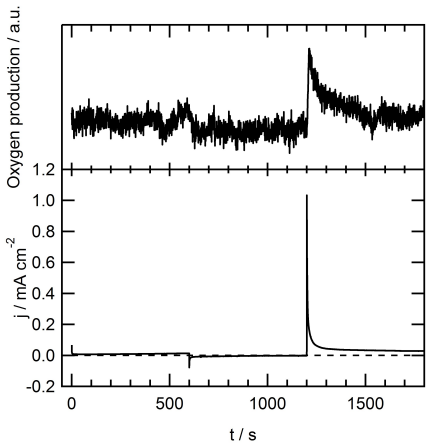

Figure 3.5: Chronoamperometry of 360 nmol $[Cu^{II}(bdmpza)_2]$ dropcasted onto a 0.72 cm^2 gold electrode (geometrical surface area) in 0.1 M NaOH. The potential was set at 2.0 V *versus* RHE for 600 seconds, then set to 0.0 V for another 600 seconds and then returned to 2.0 V for the last 600 seconds (bottom panel). The evolution of dioxygen was followed simultaneously using OLEMS (top panel).

broad negative baseline current that starts roughly at 0.8 V *versus* RHE. The negative baseline current continues upon scanning into the positive direction until 0.8 V after which a very sharp oxidative peak (7) is observed at 0.9 V *versus* RHE. With an onset of roughly 1.6 V *versus* RHE a substantial catalytic wave is observed in the cyclic voltammetry that greatly exceeds the oxidative current that was observed in the first scan. When an initial starting potential was selected below 0.8 V *versus* RHE, such a catalytic current can already be observed at the very first oxidative scan, suggesting it is triggered by an initial reduction of $[Cu^{II}(bdmpza)_2]$. In the second reductive scan a broad feature at 0.5 V *versus* RHE is observed followed by a catalytic reductive current with an onset at 0.2 V *versus* RHE. This latter catalytic feature is most likely due to reduction of dioxygen that is formed above 1.7 V *versus* RHE in the second scan. From here on the redox features in the cyclic voltammogram do not further change upon potential cycling. The catalytic current does increase somewhat from scan 2 to 3, indicating that still more active water oxidation sites are formed on the WE.

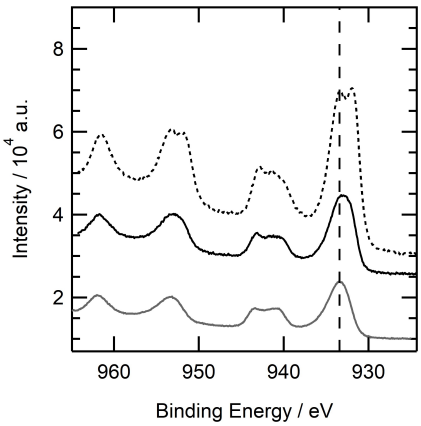

Figure 3.6: *Ex situ* XPS spectra taken after dropcasting 180 nmol $[Cu^{II}(bdmpza)_2]$ onto 0.88 cm^2 pyrolitic disc and applying 2.0 V for 10 minutes (black dotted line), applying 0 V for 10 minutes followed by 10 minutes of applying 2.0 V (black solid line). The grey line is benchmark CuO, while the vertical dotted line is at 933.4, indicating the peak for CuO.

The displayed catalytic activity in the presence of $[Cu^{II}(bdmpza)_2]$ was further evaluated by chronoamperometry experiments using both gold (Figure 3.5) and pyrolytic graphite electrodes. In this series of experiments 1.2 V *versus* RHE was selected as a standby potential as no oxidative or reductive currents were observed at this potential in the first scan of the voltammogram of $[Cu^{II}(bdmpza)_2]$. On gold an initial current of 7 μA cm^{-2} was observed after 120 seconds of amperometry at 2.0 V that steadily increased to 13 μA cm^{-2} after 30 minutes (Figure 3.5). This suggests that some activation of $[Cu^{II}(bdmpza)_2]$ to a (more) active catalytic species takes place under these oxidative conditions. In line with the oxidative current observed in the amperometry, online electrochemical mass spectrometry (OLEMS) data do show formation of some dioxygen over the course of time (Figure 3.5, top panel).

X-ray photoelectron spectroscopy of $[Cu^{II}(bdmpza)_2]$ dropcasted on a pyrolytic graphite electrode that was kept at 2.0 V *versus* RHE for 10 minutes shows two independent signals in the binding energy region of the 2p electrons of copper at 931.1 and 933.3 eV (see Figure 3.6. The low binding energy peak (931.3 eV) can be due to either Cu metal or a Cu(I) species, such as

Cu_2O. The Cu LMM Auger peaks exclude the presence of metallic Cu (which has a distinct peak at 565,5 eV), and, interestingly, also that of $Cu(OH)_2$(which has a peak at 570.4 eV).[44] The signal at 933.3 eV is similar to that of CuO for which we find a binding energy of 933.4 eV (slightly higher values have been reported in literature: *i.e.* 933.9 eV, [34] 933.7 eV, [45] 933.8 eV [46]). The shake-up structure is mostly characteristic of CuO, except for the small but visible feature on the high binding energy side (about 942 eV), which is also present in the spectrum of Cu_2O. Hence we interpret the *ex situ* XPS measurement of $[Cu^{II}(bdmpza)_2]$ kept at 2.0 V *versus* RHE for 10 minutes to a mixture of Cu(I) and Cu(II) oxides, while the spectra show no evidence for Cu metal nor $Cu(OH)_2$. Apparently $[Cu^{II}(bdmpza)_2]$ slowly converts to CuO at 2.0 V *versus* RHE. Since CuO is a known water oxidation catalyst[33, 34, 47] and the catalytic activity increases upon prolonged electrolysis it seems likely that CuO is responsible for most, if not all, catalytic current. In fact at this point we have no reason to believe that any of the observed catalytic activity should be ascribed to the $[Cu^{II}(bdmpza)_2]$ species itself.

When the potential after the initial amperometry experiment at 2.0 V is set at 0.0 V for 10 minutes and then placed back at 2.0 V *versus* RHE, a considerably higher catalytic current is observed. This is in line with OLEMS data at this stage, which shows that a considerable amount of dioxygen is produced (Figure 3.5, top panel). After 60 seconds a current of 56 μA cm^{-2} was recorded that slowly decreased to 28 μA cm^{-2}. Even higher catalytic currents are obtained when $[Cu^{II}(bdmpza)_2]$ is immediately reduced at 0 V and then brought to 2.0 V. X-ray photoelectron spectroscopy now only shows a single peak at 933.3 eV suggesting that full conversion to CuO has taken place. The decrease of the catalytic current upon prolonged electrolysis is most likely due to depletion of Cu^{2+} from the electrode under these conditions. It is likely that upon reduction $[Cu^{II}(bdmpza)_2]$ converts to metallic Cu(0) at the electrode interface that in turn is oxidized to CuO. For several related systems conversion of molecular species to Cu(0) has been observed in relation to the catalytic hydrogen evolution reaction.[48–50]

From the cyclic voltammetry in Figure 3.3 it was observed that the electrochemical reduction of $[Cu^{II}(bdmpza)_2]$ has a great influence on the current observed in the oxidative regime and is believed to proceed via initial formation of metallic copper. An electrochemical quartz crystal microbalance (EQCM) in combination with cyclic voltammetry is a powerful tool to gain insight into adsorption processes taking place on the electrode. In these studies roughly 180

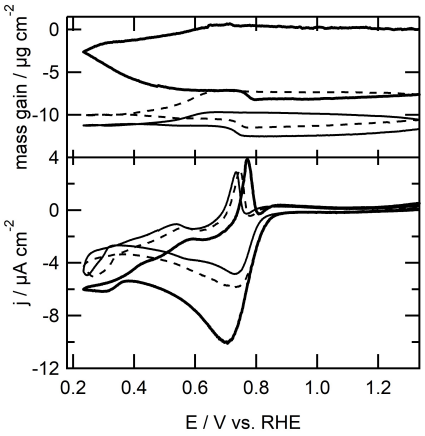

Figure 3.7: Electrochemistry of $[Cu^{II}(bdmpza)_2]$ combined with a quartz crystal microbalance showing the loss of mass of the electrode (top panel) during cyclic voltammetry (bottom panel) in a 0.1 M aqueous NaOH solution of pH 13. E_{start} = 1.3 V, scan rate = 1 mV s^{-1}.

nmol $[Cu^{II}(bdmpza)_2]$ in EtOH was dropcasted onto the EQCM electrode. Figure 3.7 shows the EQCM of $[Cu^{II}(bdmpza)_2]$ between 1.3 and 0.2 V *versus* RHE. The bottom panel shows the potential — current relationship from the CV, whereas the top panel shows the corresponding mass change of the quartz crystal, determined from the change in oscillation frequency of the quartz crystal simultaneously with the cyclic voltammetry experiment. At a scan rate of 1 mV s^{-1} a broad and clearly visible reduction peak is observed with an onset of 0.7 *versus* RHE, due to reduction of $[Cu^{II}(bdmpza)_2]$ to Cu(0). The features observed in the cyclic voltammetry upon reduction leading to formation of copper are strongly scan rate dependent. Similar to the cyclic voltammetry depicted in Figure 3.3b, a negative baseline is observed in both negative and positive scan. In addition to reduction of $[Cu^{II}(bdmpza)_2]$, this in part may be due to reduction of some dioxygen that leaks into the Teflon EQCM cell. The top panel of Figure 3.7 shows that the initial mass of the electrode does not change upon scanning the potential from 1.3 to 0.7 V *versus* RHE. Beyond the onset of the reduction wave at 0.7 V *versus* RHE in the cyclic voltammogram, the mass of the crystal starts to decrease, indicating that desorption of material from the electrode takes place. This mass decrease continues in the positive going scan and reaches a plateau

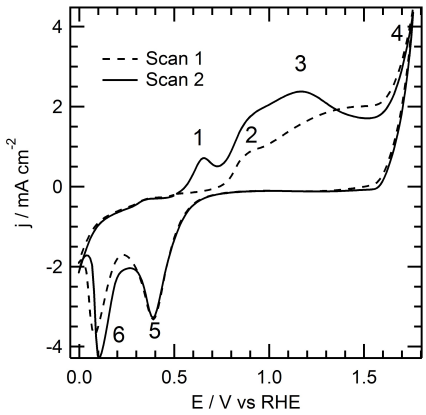

Figure 3.8: Cyclic voltammogram of a polycrystalline Cu electrode at 100 mV s^{-1} in 0.1 M aqueous NaOH solution (pH 13). The experiment is started at 0.5 V versus RHE and scanned towards positive potentials first.

at 0.4 V *versus* RHE. The sharp oxidation peak observed at 0.8 V *versus* RHE is considerably less dependent on the scan rate. This is most likely a stripping peak,[51] illustrated by a small and abrupt decrease in mass. The second and third scan show considerably less current and smaller mass changes than the first scan and is in agreement with a high conversion of $[Cu^{II}(bdmpza)_2]$ to metallic copper at this stage. In Figure 3.7, a total charge of 8.5 mC has passed through the WE to reduce $[Cu^{II}(bdmpza)_2]$, which equals a total of 88 nmol electrons. A larger amount of 180 nmol $[Cu^{II}(bdmpza)_2]$ was dropcasted onto the gold electrode, but it proved difficult to exclude large amounts of material from ending up on the quartz rather than on the gold surface which is electrochemically active. Moreover some of the charge flow may be due to reduction of dioxygen as it proved to be difficult to exclude air leaking into the Teflon EQCM cell. Nevertheless these numbers are in line with a considerable part of the dropcasted material to be reduced to copper in the EQCM experiment and agree with full conversion of $[Cu^{II}(bdmpza)_2]$ to take place during prolonged amperometry at 0.0 V *versus* RHE.

The EQCM data in Figure 3.7 shows that relatively little ligand ($\sim$75 nmol bdmpza equaling 21 % of dropcasted bdmpza) is lost from the electrode interface during the reduction of

$[Cu^{II}(bdmpza)_2]$ to Cu(0). Also the amount of copper lost to the solution at the copper stripping peak at 0.8 V *versus* RHE is limited (after three scans $\sim$ 70 nmol Cu, 38 % of all dropcasted copper).

In the cyclic voltammetry of polycrystalline copper a small oxidation wave is observed at 0.6 V *versus* RHE that is ascribed to oxidation of Cu(0) to Cu_2O (Figure 3.8, signal 1).[51] A very similar oxidation wave is observed at 0.6 V in case of deposited $[Cu^{II}(bdmpza)_2]$ (Figures 3.3 and 3.7). Further oxidation to CuO, however, is considerably more facile in case of deposited $[Cu^{II}(bdmpza)_2]$ compared to polycrystalline copper, which shows broad features (signals 2 and 3 in Figure 3.8) as the result of oxidation of different crystal domains.[51–53] The copper deposit obtained from $[Cu^{II}(bdmpza)_2]$ only shows a small and very sharp oxidation wave (Figure 3.3b, signal 7). We have been unable to reproduce these electrochemical features of using other sources of copper, including copper oxide nanoparticles, $Cu(OTf)_2$ and a polycrystalline copper electrode (see Figure 3.8). In all these cases copper is considerably easier removed from the electrode surface compared to samples of $[Cu^{II}(bdmpza)_2]$. In line with the remarkable stability of the copper catalyst obtained from $[Cu^{II}(bdmpza)_2]$ compared to other sources of copper, also the observed catalytic current is more persistent and significantly higher. It appears that the bdmpza ligand has clear effect on the stability of the copper particles that are formed, and seems to prevent solvation of Cu^{2+} upon reoxidation of copper to the +II oxidation state. In line with such a hypothesis the presence of concentrated solutions of carbonate[54] and especially borate[34, 55] have a dramatic influence on the stability and therefore activity of copper deposits under oxidative conditions. It seems that similar to coordinating anions, the $bdmpza^-$ ligand has a stabilizing effect on copper oxide *versus* solvation, thereby posing an interesting application of the use of organic ligands and/or additives in heterogeneous water oxidation chemistry.

3.4 Conclusions

Two paths haven been identified wherein $[Cu^{II}(bdmpza)_2]$ is converted to CuO, which is the true active species in the water oxidation reaction (Figure 3.9). Under oxidative conditions the complex $[Cu^{II}(bdmpza)_2]$ slowly converts to CuO and leads to moderate activity only. Initial reduction of $[Cu^{II}(bdmpza)_2]$ below 0.8 V *versus* RHE leads to initial formation of Cu(0), which ultimately converts to CuO under catalytic conditions. This path leads to a substantial higher cat-

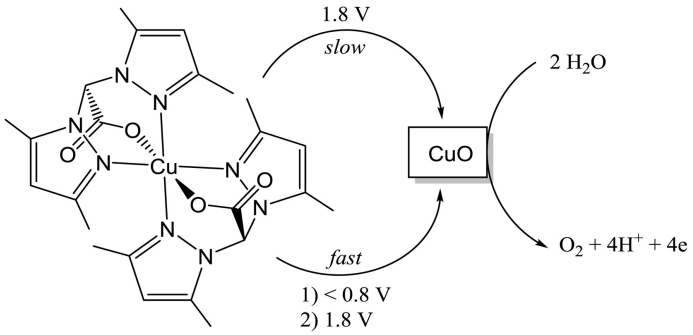

Figure 3.9: Activation pathways of $[Cu^{II}(bdmpza)_2]$ towards CuO, the active water oxidation catalyst.

alytic activity under the conditions explored. One therefore has to be very careful which standby and/or start potential is selected prior to catalytic water oxidation mediated by molecular copper complexes, as these settings may have a dramatic effect on the displayed catalytic activity as illustrated above. Also the $bdmpza^-$ ligand plays an important role in the observed catalytic activity, since dropcasting various other copper sources results in mediocre stability and activity. Clearly one cannot use such alternative copper sources convincingly as a control for the formation of active CuO nanoparticles. The precise mechanism wherein $bdmpza^-$ influences the catalytic activity is not well understood at present.

Acknowledgments

The authors gratefully acknowledge dr. Tom van Dijkman and prof. dr. Elisabeth Bouwman for supplying the bdmpzaNa ligands used in this work. This work was financially supported by the ERC (StG 637556).

References

(1) Duan, L.; Bozoglian, F.; Mandal, S.; Stewart, B.; Privalov, T.; Llobet, A.; Sun, L. *Nat. Chem.* **2012**, *4*, 418–423.

(2) Matheu, R.; Ertem, M. Z.; Benet-Buchholz, J.; Coronado, E.; Batista, V. S.; Sala, X.; Llobet, A. *J. Am. Chem. Soc.* **2015**, *137*, 10786–10795.

(3) Concepcion, J. J.; Jurss, J. W.; Norris, M. R.; Chen, Z.; Templeton, J. L.; Meyer, T. J. *Inorg. Chem.* **2010**, *49*, 1277–1279.

(4) Diaz-Morales, O.; Hersbach, T. J. P.; Hetterscheid, D. G. H.; Reek, J. N. H.; Koper, M. T. M. *J. Am. Chem. Soc.* **2014**, *136*, 10432–10439.

(5) Lalrempuia, R.; McDaniel, N. D.; Müller-Bunz, H.; Bernhard, S.; Albrecht, M. *Angew. Chem. Int. Ed.* **2010**, *49*, 9765–9768.

(6) Bucci, A.; Savini, A.; Rocchigiani, L.; Zuccaccia, C.; Rizzato, S.; Albinati, A.; Llobet, A.; Macchioni, A. *Organometallics* **2012**, *31*, 8071–8074.

(7) Sheehan, S. W.; Thomsen, J. M.; Hintermair, U.; Crabtree, R. H.; Brudvig, G. W.; Schmuttenmaer, C. A. *Nat. Commun.* **2015**, *6*, 6469.

(8) Blakemore, J. D.; Schley, N. D.; Balcells, D.; Hull, J. F.; Olack, G. W.; Incarvito, C. D.; Eisenstein, O.; Brudvig, G. W.; Crabtree, R. H. *J. Am. Chem. Soc.* **2010**, *132*, 16017–16029.

(9) Hetterscheid, D. G. H.; van der Ham, C. J. M.; Diaz-Morales, O.; Verhoeven, M. W. G. M.; Longo, A.; Banerjee, D.; Niemantsverdriet, J. W.; Reek, J. N. H.; Feiters, M. C. *Phys. Chem. Chem. Phys.* **2016**, *18*, 10931–10940.

(10) Nyhlén, J.; Duan, L.; Åkermark, B.; Sun, L.; Privalov, T. *Angew. Chem. Int. Ed.* **2010**, *49*, 1773–1777.

(11) Concepcion, J. J.; Tsai, M.-K.; Muckerman, J. T.; Meyer, T. J. *J. Am. Chem. Soc.* **2010**, *132*, 1545–1557.

(12) Chen, Z.; Concepcion, J. J.; Hu, X.; Yang, W.; Hoertz, P. G.; Meyer, T. J. *P. Natl, Acad. Sci. U.S.A.* **2010**, *107*, 7225–9.

(13) Fukuzumi, S.; Hong, D. C. *Eur. J. Inorg. Chem.*. **2014**, 645–659.

(14) Limburg, B.; Bouwman, E.; Bonnet, S. *Coordin. Chem. Rev.* **2012**, *256*, 1451–1467.

(15) Junge, H.; Marquet, N.; Kammer, A.; Denurra, S.; Bauer, M.; Wohlrab, S.; Gärtner, F.; Pohl, M.-M.; Spannenberg, A.; Gladiali, S.; Beller, M. *Chem. Eur. J.* **2012**, *18*, 12749–12758.

(16) Blakemore, J. D.; Schley, N. D.; Olack, G. W.; Incarvito, C. D.; Brudvig, G. W.; Crabtree, R. H. *Chem. Sci.* **2011**, *2*, 94–98.

(17) Limburg, J.; Vrettos, J. S.; Liable-Sands, L. M.; Rheingold, A. L.; Crabtree, R. H.; Brudvig, G. W. *Science* **1999**, *283*, 1524–1527.

(18) Lloret-Fillol, J.; Codolà, Z.; Garcia-Bosch, I.; Gómez, L.; Pla, J. J.; Costas, M. *Nat. Chem.* **2011**, *3*, 807–813.

(19) Kottrup, K. G.; Hetterscheid, D. G. H. *Chem. Commun.* **2016**, *52*, 2643–2646.

(20) Ellis, W. C.; McDaniel, N. D.; Bernhard, S.; Collins, T. J. *J. Am. Chem. Soc.* **2010**, *132*, 10990–10991.

(21) Wasylenko, D. J.; Ganesamoorthy, C.; Borau-Garcia, J.; Berlinguette, C. P. *Chem. Commun.* **2011**, *47*, 4249.

(22) Barnett, S. M.; Goldberg, K. I.; Mayer, J. M. *Nat. Chem.* **2012**, *4*, 498–502.

(23) Gerlach, D. L.; Bhagan, S.; Cruce, A. A.; Burks, D. B.; Nieto, I.; Truong, H. T.; Kelley, S. P.; Herbst-Gervasoni, C. J.; Jernigan, K. L.; Bowman, M. K.; Pan, S.; Zeller, M.; Papish, E. T. *Inorg. Chem.* **2014**, *53*, 12689–12698.

(24) Pap, J. S.; Szyrwiel, L.; Srankó, D.; Kerner, Z.; Setner, B.; Szewczuk, Z.; Malinka, W. *Chem. Commun.* **2015**, *51*, 6322–6324.

(25) Zhang, T.; Wang, C.; Liu, S.; Wang, J.-L.; Lin, W. *J. Am. Chem. Soc.* **2014**, *136*, 273–281.

(26) Su, X.-J.; Gao, M.; Jiao, L.; Liao, R.-Z. Z.; Siegbahn, P. E. M.; Cheng, J.-P.; Zhang, M.-T. *Angew. Chem. Int. Ed.* **2015**, *54*, 4909–4914.

(27) Zhang, M.-T.; Chen, Z.; Kang, P.; Meyer, T. J. *J. Am. Chem. Soc.* **2013**, *135*, 2048–2051.

(28) Chen, Z.; Meyer, T. J. *Angew. Chem. Int. Edit.* **2013**, *52*, 700–703.

(29) Garrido-Barros, P.; Funes-Ardoiz, I.; Drouet, S.; Benet-Buchholz, J.; Maseras, F.; Llobet, A. *J. Am. Chem. Soc.* **2015**, *137*, 6758–6761.

(30) Coggins, M. K.; Zhang, M.-T.; Chen, Z.; Song, N.; Meyer, T. J. *Angew. Chem. Int. Ed.* **2014**, *53*, 12226–12230.

(31) Li, T.-T.; Cao, S.; Yang, C.; Chen, Y.; Lv, X.-J.; Fu, W.-F. *Inorg. Chem.* **2015**, *54*, 3061–3067.

(32) Liu, X.; Jia, H.; Sun, Z.; Chen, H.; Xu, P.; Du, P. *Electrochem. Commun.* **2014**, *46*, 1–4.

(33) Liu, X.; Cui, S.; Sun, Z.; Du, P. *Electrochim. Acta* **2015**, *160*, 202–208.

(34) Yu, F.; Li, F.; Zhang, B.; Li, H.; Sun, L. *ACS Catal.* **2015**, *5*, 627–630.

(35) Liu, X.; Cui, S.; Qian, M.; Sun, Z.; Du, P. *Chem. Commun.* **2016**, *52*, 5546–5549.

(36) Folkman, S. J.; Kirner, J. T.; Finke, R. G. *Inorg. Chem.* **2016**, *55*, 5343–5355.

(37) Stracke, J. J.; Finke, R. G. *J. Am. Chem. Soc.* **2011**, *133*, 14872–14875.

(38) Stracke, J. J.; Finke, R. G. *ACS Catal.* **2013**, *3*, 1209–1219.

(39) Vickers, J. W.; Lv, H. J.; Sumliner, J. M.; Zhu, G. B.; Luo, Z.; Musaev, D. G.; Geletii, Y. V.; Hill, C. L. *J. Am. Chem. Soc.* **2013**, *135*, 14110–14118.

(40) Burzlaff, N.; Hegelmann, I.; Weibert, B. *J. Organomet. Chem.* **2001**, *626*, 16–23.

(41) Kozlevcar, B.; Gamez, P.; de Gelder, R.; Driessen, W. L.; Reedijk, J. *Eur. J. Inorg. Chem.* **2003**, 47–50.

(42) Wonders, A. H.; Housmans, T. H. M.; Rosca, V.; Koper, M. T. M. *J. Appl. Electrochem.* **2006**, *36*, 1215–1221.

(43) Kozlevčar, B.; Golobic, A.; Gamez, P.; Koval, I. A.; Driessen, W. L.; Reedijk, J. *Inorg. Chim. Acta* **2005**, *358*, 1135–1140.

(44) Waechtler, T.; Oswald, S.; Roth, N.; Jakob, A.; Lang, H.; Ecke, R.; Schulz, S. E.; Gessner, T.; Moskvinova, A.; Schulze, S.; Hietschold, M. *J. Electrochem. Soc.* **2009**, *156*, H453.

(45) Durando, M.; Morrish, R.; Muscat, A. J. *J. Am. Chem. Soc.* **2008**, *130*, 16659–16668.

(46) Moulder, J. F.; Stickle, W. F.; Sobol, P. E.; Bomben, K. D. Handbook of X-ray Photoelectron Spectroscopy., 1995.

(47) Liu, X.; Cui, S.; Sun, Z.; Ren, Y.; Zhang, X.; Du, P. *J. Phys. Chem. C* **2016**, *120*, 831–840.

(48) Kugler, M.; Scholz, J.; Kronz, A.; Siewert, I. *Dalton T.* **2016**, *45*, 6974–6982.

(49) Liu, X.; Zheng, H.; Sun, Z.; Han, A.; Du, P. *ACS Catal.* **2015**, *5*, 1530–1538.

(50) Liu, X.; Cui, S.; Sun, Z.; Du, P. *Chem. Commun.* **2015**, *51*, 12954–12957.

(51) Giri, S. D.; Sarkar, a. *J. Electrochem. Soc.* **2016**, *163*, I1252–I1259.

(52) Ambrose, J.; Barradas, R. G.; W., S. D. *J. Electroanal. Chem.* **1973**, *47*, 65–80.

(53) Droog, J. M. M.; Alderliesten, C. A.; Alderliesten, P. T.; Bootsma, G. A. *J. Electroanal. Chem.* **1980**, *111*, 61–70.

(54) Du, J.; Chen, Z.; Ye, S.; Wiley, B. J.; Meyer, T. J. *Angew. Chem. Int. Ed.* **2015**, *54*, 2073–2078.

(55) Shi, Y.; Gimbert-Surinach, C.; Han, T.; Berardi, S.; Lanza, M.; Llobet, A. *ACS Appl. Mater. Inter.* **2016**, *8*, 696–702.

4 | *In situ* generated copper-phenanthroline complexes as catalysts for the oxygen reduction reaction

Abstract

The oxygen reduction reaction was investigated with an *in situ* generated copper phenanthroline complex using different ratios of ligand to copper. A structural investigation of the *in situ* generated complex by EPR spectroscopy showed the formation of complexes in two different geometries. The 1:1 complex has an elongated octahedron geometry and is an active oxygen reduction catalyst. In case of this species, reduction of Cu^{II} is not reversible. At a higher 1,10-phenanthroline to copper ratio a complex is generated with a trigonal bipyrimidal geometry. In this case the complex has a well-defined redox couple, but is not active towards the oxygen reduction reaction. There is thus a paradox wherein a decision has to be made between catalytic activity and stability of the complex. Under reductive conditions the possibility of forming a metallic copper layer on the electrode surface is ever present. A strategy to prevent the active 1:1 complex form forming an electrocatalytically active copper layer is proposed. This strategy is discussed in detail in Chapter 5.

"Tell me, tutor,' I said. 'Is revenge a science, or an art?"

Mark Lawrence in *Prince of Thorns*

In preparation for publication

4.1 Introduction

The oxygen reduction reaction is of interest for the development of efficient fuel cells wherein it is the counter reaction to the hydrogen oxidation reaction. In order to find an excellent catalyst for the oxygen reduction reaction, the binding energy of all intermediates of the catalytic cycle wherein oxygen reduction takes place need to be optimized simultaneously. This will result in a potential energy landscape wherein all redox intermediates within the catalytic cycle are found at the equilibrium potential of water. Under these conditions catalysis should start at the equilibrium potential. Since the various catalytic intermediates bind in a very similar manner to a heterogeneous surface, it is not possible to align these to the same potential energy. This inability to align the catalytic intermediates from an energetic point of view is referred to as the scaling relationships, first described by Nørskov.[1] Due to such scaling relations the oxygen reduction reaction has a theoretical minimum overpotential of 0.41 V at a metal surface.[2]

In nature, laccase is an efficient copper-based enzyme for the reduction of oxygen to water.[3] Due to the complex protein backbone the reaction pathway for the oxygen reduction reaction is different to that of heterogeneous catalysts. This difference in reaction mechanism leads to a different potential energy landscape and a lowering of the overpotential of the oxygen reduction reaction compared to heterogeneous surfaces is observed.

The difficulty of using copper as a molecular oxygen reduction catalyst lies in the fast ligand exchange kinetics of copper. The exchange rate of water ligands at a Cu^{II} center is in the range of 10^8 ligands per second.[4, 5] The low barrier for ligand exchange on copper complexes causes other ligands to be replaced at a high exchange rate as well. By decoordinating the ligands from the metal center under reductive conditions a metallic copper layer can be formed on the surface of the electrode (see for example Chapter 3). Using 3,5-diamino-1,2,4-triazole (DAT) as a ligand, a dinuclear $Cu_2(DAT)_2$ complex is formed,[6] which was claimed to be a very active oxygen reduction catalyst.[7] The structure of the formed catalyst is highly dependent on the reaction conditions.[8] The complex $[Cu_2(DAT)_2(\mu\text{-}OH_2)(H_2O)_4(SO_4)](SO_4) \cdot 3.5H_2O$ synthesised *ex situ* forms a deposit on the electrode surface during oxygen reduction.[9] Moreover, when the complex is dropcasted onto a glassy carbon electrode, the loss of DAT from the complex is observed and a Cu(0) deposit is formed on the surface of the electrode. This surface deposit is the active

oxygen reduction catalyst.[9] Therefore, one needs to be careful to the nature of the active catalyst in copper-mediated oxygen reduction. Under very low concentrations of DAT, a copper layer is formed on a glassy carbon electrode, which is a good catalyst for carbon dioxide reduction.[8]

Anson and coworkers reported oxygen reduction using physisorbed copper complexes with 1,10-phenanthroline based ligands.[10–12] The first report describes a copper complex with a 4,7-diphenyl-1,10-phenanthrolinedisulfonate (DPP) ligand which is forming a $[Cu\text{-}(DPP)_2H_2O]^{2-}$ complex in water.[11] The complex has a very large interaction with a pyrolytic graphite electrode, causing the complex to adsorb on the working electrode spontaneously. Using the charge transfer of the redox couple, the surface coverage of the complex was determined to be 8.5×10^{-10} mol cm^{-2}, indicating multiple layers of complex on the electrode surface. Two different species are observed in the cyclic voltammetry, of which the first is claimed to be a Cu^{II} complex with two ligands and water ligated to the copper center. The copper sits in a tetragonal geometry, with one of the axial position being unavailable due to surface adsorption. The second structure is claimed to be a tetrahedral Cu^{I} complex with only two DPP ligands coordinated. This indicates a substantial structural change upon reduction from Cu^{II} to Cu^{I} and might forestall the adsorption of the complex on the electrode surface. The cyclic voltammetry did not change when an excess of DPP was added to the electrolyte solution, which is an indication that under these conditions no complex is present with only one DPP ligand. During oxygen and H_2O_2 reduction, the $[Cu^{II}(DPP)_2H_2O]^{2-}$ complex is suggested to be reduced to $[Cu^{I}(DPP)_2H_2O]^{3-}$, which is the active species that binds dioxygen. Deactivation of the catalyst was suggested to occur through formation of $[Cu^{I}(DPP)_2]^{3-}$ via dissociation of an aqua ligand from the active oxygen reduction catalyst $[Cu^{I}(DPP)_2H_2O]^{3-}$. It can be reactivated by oxidizing the complex to the $[Cu^{II}(DPP)_2]^{2-}$ complex, which will spontaneously form the stable $[Cu^{II}(DPP)_2H_2O]^{2-}$, restoring the initial catalytic activity.

Using different phenanthroline derivatives, Zhang and Anson found that the 4,7-dimethyl-1,10-phenanthroline (DMP) ligand performs best in the copper mediated oxygen reduction.[10] This was correlated to a shift of the Cu^{I}/Cu^{II} couple to higher potentials compared to copper complexes with 1,10-phenanthroline, 2-2'-bipyridine, 6,6-dimethyl-2,2'-bipyridine and 6-methyl-2,2'-bipyridine ligands. Similar to the complex $[Cu^{II}(DPP)_2H_2O]^{2+}_{ads}$ *vide supra*, the complex $[Cu^{II}(DMP)]^{2+}$ adsorbs onto the graphite working electrode spontaneously, as is observed

from the shape of the redox couples in the cyclic voltammogram. The formation of both complexes $[Cu^{II}(DMP)]^{2+}_{ads}$, with only one ligand coordinated, and $[Cu^{II}(DMP)_2]^{2+}_{ads}$ are observed electrochemically. The adsorbed complex with one ligand is predominantly observed when $CuSO_4$ is present in solution, whereas in presence of DMP in the electrolyte solution, the $[Cu^{II}(DMP)_2]^{2+}_{ads}$ complex is observed. This indicates the complex can reversibly form the complex with one and with two DMP ligands, depending on the presence of Cu^{2+} or DMP in the electrolyte solution. Oxygen and H_2O_2 reduction is observed in presence of the $[Cu^{II}(DMP)]^{2+}_{ads}$ complex, with an onset potential of 0.79 V *versus* RHE at pH 5. This is in contrast to the DPP case, where the active species was proposed to have two bidentate ligands coordinated. Due to the adsorption of the active species to pyrolytic graphite and the absence of any spectroscopic data of Cu at such materials, prompted us to investigate the ORR at copper phenanthroline species under better defined reaction conditions.

Here we report oxygen reduction by *in situ* generated copper-phenanthroline complexes. Since the ligands have a very strong interaction with pyrolytic graphite electrodes and the difficulty to characterize, gold electrodes were selected as the working electrode. The structure of the *in situ* generated complexes was investigated using EPR spectroscopy. Other ligands were investigated as well, DMP is an interesting ligand for a copper complex as it gives higher activity than copper-phenanthroline when adsorbed on graphite electrodes.[10] Bipy is interesting as ligand as it is very similar in structure as 1,10-phenanthroline, but allows for rotation between the phenyl rings, giving the complex more flexibility.

4.2 Experimental

4.2.1 Materials

1,10-phenanthroline (Sigma Aldrich, 97%), 2-2'-bipyridine (Alfa Aesar, 99%), 4,7-dimethyl-1,10-phenanthroline (Sigma Aldrich) and $Cu(OTf)_2$ (Alfa Aesar, $\geq$ 99%) were used as received.

Electrolyte solutions were prepared with $HClO_4$ (Merck suprapur, 70 %), HCl (Merck, 37 %), Na_2HPO_4 (Merck, 99.9%), NaH_2PO_4 (Merck, 99.9 %), NaCl (Merck, 99.9 %) and were prepared with MilliQ water ($>$ 18.2 MΩ cm resistivity).

Argon and dioxygen (5.0) were purchased from Linde Gas.

4.2.2 Electrochemical methods

All electrochemical experiments were performed on an Autolab PGSTAT 128N with integrated EQCM module in one-compartment 25 ml glass cells in three-electrode setups. A gold working electrode (99.995 %, Alfa Aesar, 0.05 cm^2 geometric surface area) was used in a hanging meniscus configuration. Platinum (99.99%, Alfa Aesar) was used as a counter electrode and a Ag/AgCl (3 M KCl) purchased from Autolab was used as reference electrode. The potentials were adjusted to the reversible hydrogen electrode (RHE) scale by addition of 0.446 V to the potential *versus* Ag/AgCl.

The Au electrode was cleaned by oxidation at 10 V *versus* a graphite rod counter electrode in 10% H_2SO_4 for 30 s. This was followed by a 6 M HCl bath for 20 s, followed by flame annealing. The electrode was then electrochemically polished by cycling between 0 and 1.75 V *versus* RHE (E_{start} = 0.7 V) at 1 V s^{-1} in 0.1 M $HClO_4$.

Prior to experiments, the electrolyte solution was deaerated for at least 20 minutes using argon. Oxygen reduction experiments were performed in 0.05 M NaH_2PO_4, 0.05 M Na_2HPO_4, 0.05 M NaCl and 0.6 mM HCl. In case of catalytic experiments, 0.1 mM $Cu(OTf)_2$ was added to the electrolyte solution while a 1 mM 1,10-phenanthroline concentration was used, unless denoted differently. Prior to oxygen reduction experiments, oxygen was bubbled through the electrolyte for at least 20 minutes, while during experiment, oxygen was blown over the solution.

4.2.3 EPR spectroscopy

The EPR experiments were performed on a Bruker EMXplus X-band. Simulation of the spectra was performed using the W95EPR software. The spectra were simulated using the W95EPR software. The EPR samples were prepared by dissolving different concentrations, ranging from 1 mM to 0.1 mM, of 1,10-phenanthroline together with 0.1 mM Cu^{II}, 0.1 M phosphate buffer, 0.05 M NaCl acidified to pH 4 using HCl. The samples were recorded at 77 K.

4.3 Results

4.3.1 EPS spectroscopy of an *in situ* generated copper-phenanthroline complex

Cu^{2+} is insoluble in in a perchlorate solution in absence of any ligand. To avoid precipitation of copper from the reaction mixture, an electrolyte based on chloride was selected, which kept all copper species in solution prior to the electrochemistry experiments. Due to the fast ligand exchange kinetics of copper, bidentate ligands were expected to readily decoordinate immediately leading to small concentrations of free Cu^{2+}. To counter formation of substantial concentration of free copper in solution, a high ratio of 1,10-phenanthroline *versus* the copper in solution will ensure that most of the complex in solution will have two 1,10-phenanthroline ligands in the solution at all times. This should lead to a well-defined molecular complex, but does not ensure a catalytically active species. In this chapter, the structure of the ligands in solution was investigated with EPR spectroscopy, followed by an investigation of the redox behavior of the *in situ* generated complexes. Finally, the electrocatalytic behavior of the complexes is investigated for the oxygen reduction reaction.

EPR spectroscopy is powerful tool in the characterization of compounds which have at least one unpaired electron. As Cu^{II} has 9 d-electrons, one electron will always be unpaired. Cu^{II} complexes generally adopt two types of geometries: the trigonal bipyramidal and elongated octahedron geometry. Depending on the geometry of the complex, the singly occupied molecular orbital (SOMO) of the complex is either the d_{z^2} or the $d_{x^2-y^2}$ orbital. For the trigonal bipyrimidal geometry the SOMO is the d_{z^2} orbital, whereas a Cu^{II} complex in the elongated octahedron geometry has the $d_{x^2-y^2}$ as SOMO. The value of the empirical parameter g, comparable to the chemical shift in NMR spectroscopy, is determined in the x-, y- and z-direction.[13] The relative positions of the g-values can be determined by Equation 4.1, where *i* = *x*,*y* or *z*, *n* is the degree of orbital mixing, λ is the spin-orbit coupling constant, E_0 and E_n are the energies of the ground and the exited states.

$$g_i = g_e \pm \frac{n\lambda}{E_0 - E_n} \tag{4.1}$$

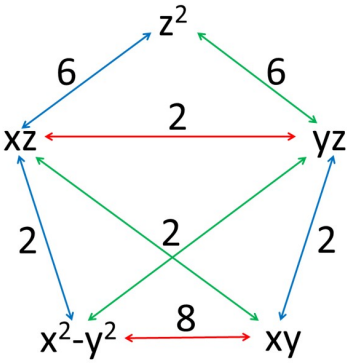

Figure 4.1: The magic pentagon for the determination of shift of g-values in EPR spectroscopy. The colors represent the direction of the overlap: green is in the x-direction, blue is in the y-direction and red is in the z-direction.

The direction of the shift, represented by $\pm$ depends whether the orbital that mix with the SOMO are filled (+) or empty (-). For Cu^{II} complexes, all orbitals except the SOMO are filled and the g-values increase as a result of orbital mixing. The shift of the g-values is thus determined by the mixing factor n, which can be obtained from the so-called "magic pentagon", displayed in Figure 4.1. The numbers in Figure 4.1 show the magnitude in which g_i shifts due to orbital mixing along axis i. The colors represent the direction of the overlap: green is in the x-direction, blue is in the y-direction and red is in the z-direction. In a molecule with a mirror plane in x-y and the SOMO is the d_{z^2} orbital, there is no orbital mixing possible in the z-direction, thus $g_z = g_e$. The g_z value in the case of the complex described in this chapter is also called $g_\perp$. Mixing in the x- and y-direction is equal resulting in only one g-value, which is called $g_\parallel$. In case the SOMO is the $d_{x^2-y^2}$, orbital mixing occurs in both xy and z direction. The orbital mixing in x- and y-direction has the same magnitude, resulting in one $g_\parallel$ value. The orbital mixing in z-direction is now larger than the mixing in the xy-plane. This results in a larger $g_\perp$ than $g_\parallel$ (Figure 4.1).

The values for $g_\perp$ and $g_\parallel$ were obtained by fitting the EPR spectra using Win95EPR. The geometry assignment was made on basis of the positions of $g_\perp$ and $g_\parallel$.

The structure of the *in situ* generated copper-phenanthroline complexes do not differ greatly

Table 4.1: *EPR parameters of in situ generated Cu(II) complexes with 1,10-phenanthroline ligands from 0.1 mM* Cu^{II} *and varying 1,10-phenanthroline concentrations in 0.1 M phosphate buffer, 0.05 M NaCl, acidified to pH 4 using HCl.*

[phen]	$g_\perp$	$g_\parallel$	*SOMO*	*Geometry*
0.1 mM	2.05	2.25	$d_{x^2-y^2}$	Elongated octahedron
0.2 mM	2.17	2.03	d_{z^2}	Trigonal bipyramid
0.3 mM	2.17	2.03	d_{z^2}	Trigonal bipyramid
0.4 mM	2.17	2.02	d_{z^2}	Trigonal bipyramid
0.5 mM	2.18	2.01	d_{z^2}	Trigonal bipyramid
0.6 mM	2.18	2.01	d_{z^2}	Trigonal bipyramid
0.7 mM	2.17	2.04	d_{z^2}	Trigonal bipyramid
0.8 mM	2.17	2.01	d_{z^2}	Trigonal bipyramid
0.9 mM	2.18	2.02	d_{z^2}	Trigonal bipyramid
1.0 mM	2.17	2.03	d_{z^2}	Trigonal bipyramid

if a 1,10-phenanthroline to copper ratio of 2:1 or higher is used (Figure 4.2 and Table 4.1). The $g_\parallel$ value is either 2.17 or 2.18 and the $g_\perp$ values range from 2.01 to 2.04. These values are slightly higher than the values found for copper-phenanthroline complexes in a previous study.[13] The values of 2.17 and ∼2.0 indicate a trigonal bipyramidal structure, with the SOMO being the d_{z^2} orbital. With a one to one ratio of copper to phenanthroline, the $g_\parallel$ value is 2.05, while the $g_\perp$ value is higher and found at 2.25. This is indicative of a complex with an elongated octahedron geometry with the SOMO being the $d_{x^2-y^2}$ orbital.

The structure of two similar *in situ* generated 10 to 1 complexes with 2-2'-bipyridine (bipy) and 4,7-dimethyl-1,10-phenanthroline (DMP) ligands were recorded by EPR as well. The g-values for 10 to 1 ligand to Cu^{II} complexes with both the DMP and bipy ligands are very similar to the 1,10-phenanthroline complex, indicating the copper complexes are also in the trigonal bipyramidal geometry.

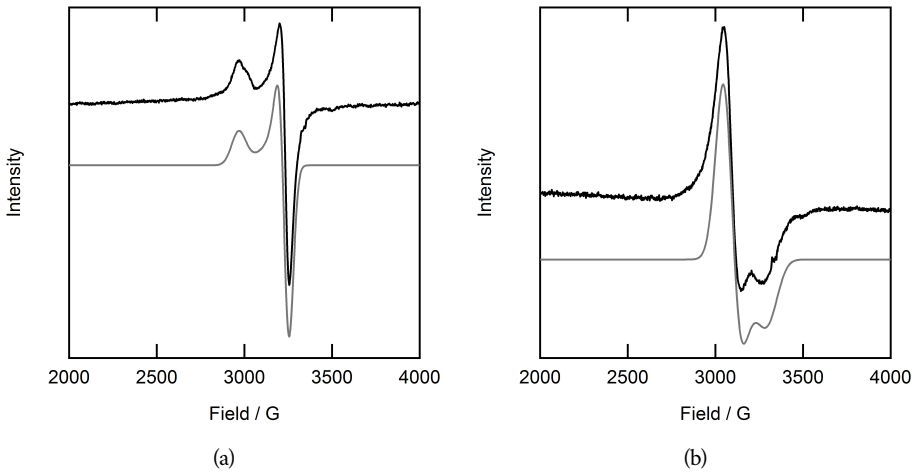

Figure 4.2: X-band EPR spectra (black lines) and simulations (grey lines) of solutions of 0.1 mM Cu^{II} with a) 0.1 mM and b) 0.2 mM phen in 0.1 M phosphate buffer and 0.05 M NaCl acidified to pH 4 using HCl at 78 K.

4.3.2 Electrochemistry of an *in situ* generated copper-phenanthroline complex

Copper-phenanthroline was formed *in situ* in solution by preparing an electrolyte solution with 1 mM Cu^{II} and 1 mM 1,10-phenanthroline and 1 mM Cu^{II} and 2 mM 1,10-phenanthroline in 0.1 M phosphate buffer containing 0.05 M NaCl acidified to pH 4 using HCl. No well-defined redox couples were observed in an electrolyte solution containing 1 mM Cu^{II} and 1 mM 1,10-phenanthroline (Figure 4.3). A reductive peak is observed at 0.45 V. In the positive going scan, an oxidative wave is observed from approximately 0.45 V up to the vertex potential of 0.75 V. In the cyclic voltammogram at a gold electrode in argon-purged electrolyte a well-defined redox couple at 0.41 V *versus* RHE was observed at a scanrate of 100 mV s^{-1}, together with two oxidation event around 0.6 and 0.7 V *versus* RHE (Figure 4.3). A single redox couple is observed if the upper vertex is kept below 0.11 V.

Due to the high ligand exchange rate of copper ions, a higher concentration of phenanthroline to copper is expected to yield more $[Cu^{II}(phen)_2L_x]^{+/2+}$ (where L is Cl^- or H_2O) and

Table 4.2: *EPR parameters of in situ generated Cu(II) complexes with different ligands from 0.1 mM Cu^{II} and 1 mM ligand in 0.1 M phosphate buffer, 0.05 M NaCl, acidified to pH 4 using HCl.*

Ligand	$g_\perp$	$g_{\|\|}$	*Ground state*	*Geometry*
phen	2.17	2.03	d_{z^2}	Trigonal bipyramid
bipy	2.17	2.01	d_{z^2}	Trigonal bipyramid
DMP	2.17	2.01	d_{z^2}	Trigonal bipyramid

thus more stable complex in solution. Even though EPR spectroscopy does not show any structural changes above a 1:2 ratio of Cu^{II} to 1,10-phenanthroline, the influence of the ratio was investigated using cyclic voltammetry as well.

Since the solubility of 1,10-phenanthroline in water is rather low (14.9 mM at 20 °C),[14] a lowering of the copper and phenanthroline concentrations compared to the cyclic voltammetry described above was needed to dissolve the phenanthroline in the electrolyte solution. The copper concentration was decreased tenfold to 0.1 mM. With an increasing 1,10-phenanthroline to copper ratio the Cu^{I}/Cu^{II}) redox couple became more reversible (Figure 4.4). Similarly to Figure 4.3 but at a 0.1 mM concentration of copper and 1,10-phenanthroline(thus at a 1:1 ratio of 1,10-phenanthroline to Cu^{II}) no reversible redox behavior is observed whatsoever. The $E_{1/2}$ shifts from 0.41 V at a 2:1 ratio to 0.34 V at a 10:1 ratio of 1,10-phenanthroline to Cu^{II}. This indicates that the balance shifts from free Cu^{2+} and $[Cu^{II}(phen)L_x]^{+/2+}$ to $[Cu^{II}(phen)_2L_x]^{+/2+}$ at a high concentration of 1,10-phenanthroline.

The redox behavior of complexes with bipy and DMP ligands was investigated in a 1 to 10 copper to ligand ratio. Cyclic voltammetry was performed with an *in situ* generated complex from 1 mM bipy and 0.1 mM Cu^{II} in 0.1 M phosphate buffer with 0.05 M NaCl acidified to pH 4 using HCl. In the cyclic voltammogram two redox events are observed (Figure 4.5a). A reversible redox couple is visible at 0.39 V *verus* RHE with low peak separation. A low peak separation is indicative of a surface adsorbed species. Between 0.6 and 0.7 V, an oxidative peak is observed, which is accompanied by a reductive peak at 0.52 V *versus* RHE. At high scanrate, the oxidative peak between 0.6 and 0.7 V broadens and the oxidative wave of the reversible redox couple at

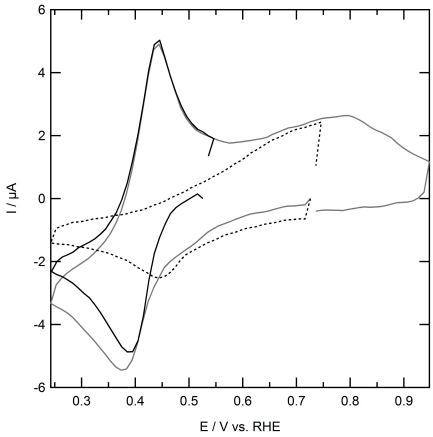

Figure 4.3: Cyclic voltammogram of a gold electrode under argon in a 1 mM solution of $Cu^{II}$and 2 mM 1,10-phenanthroline (solid lines) and in a 1 mM solution of $Cu^{II}$and 1 mM 1,10-phenanthroline (dotted line) in a 0.1 M phosphate buffer with 0.05 M NaCl acidified to pH 4 at 100 mV s^{-1}.

0.39 V is no longer visible.

In the cyclic voltammogram of *in situ* generated copper-DMP complexes from 1 mM DMP and 0.1 mM Cu^{II} in 0.1 M phosphate buffer with 0.05 M NaCl acidified to pH 4 using HCl irreversible behavior of the Cu^{I}/Cu^{II} redox couple is observed (Figure 4.5b). The separation of the peaks ranges between 470 mV at 10 mV s^{-1} to 660 mV at 500 mV s^{-1} and is thus very large. A large peak separation, and therefore irreversible redox behavior, suggests that copper deposits are being formed. It was therefore not further investigated.

By calculating the peak current of either the reduction or the oxidation process of a reversible redox process, the homogeneity of a molecular process can be determined. For one-electron transfer processes in solution, a linear relationship between the peak current and the squire root of the scanrate is expected, according to the Randles Cevčik relation (Equation 4.2), where i_p is the peak current, n is the number of electrons, F is the Faraday constant, ν is the scanrate, A is the electrode area D_0 is the diffusion constant, R is the gas constant and T is the temperature. For the Randles Cevčik relation, the peak position of the redox couple needs to be constant with

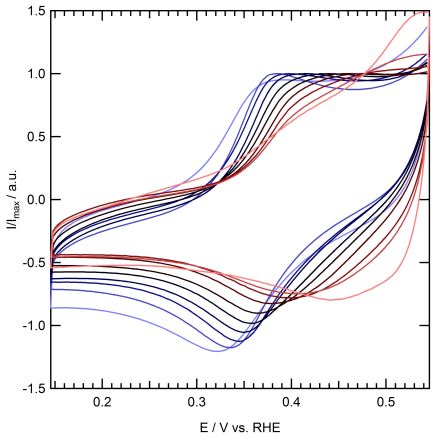

Figure 4.4: Cyclic voltammograms with a range of 1,10-phenanthroline concentration from 1 mM (blue line) to 0.1 mM (red line) and 0.1 mM of Cu^{II} in a 0.1 M phosphate buffer with 0.05 M NaCl acidified to pH 4 at 100 mV s^{-1}.

changing scanrate.

$$i_p = 0.466nFAC^0 \left(\frac{nF\nu D_0}{RT}\right)^{1/2} \tag{4.2}$$

The peak position of the redox couples of cyclic voltammograms of *in situ* generated complexes from 1 mM 1,10-phenanthroline and 0.1 mM Cu^{II} stays the same while changing the scanrate from 10 to 500 mV s^{-1} with $E_{1/2}$ = 0.81 V *verus* RHE (Figure 4.6). At scanrates of 200 mV s^{-1} and higher (blue lines), the oxidative peak becomes less well-defined. Therefore the reductive peak was used to investigate the homogeneity of the catalytic process.

The peak current of cyclic voltammograms with a 10:1 ratio of ligand to Cu^{II} is linear with the square root of the scanrate (Figure 4.7). Moreover, the trend line goes through the origin when it is extrapolated. This indicates the complex behaves as a dissolved molecular species which exhibits one-electron transfer to the working electrode. The complex in solution has the trigonal bipyramidal geometry with two 1,10-phenanthroline ligands attached to the copper ion, as was described in the EPR section *vide supra*.

The oxygen reduction reaction was investigated on a bare gold electrode and with *in situ*

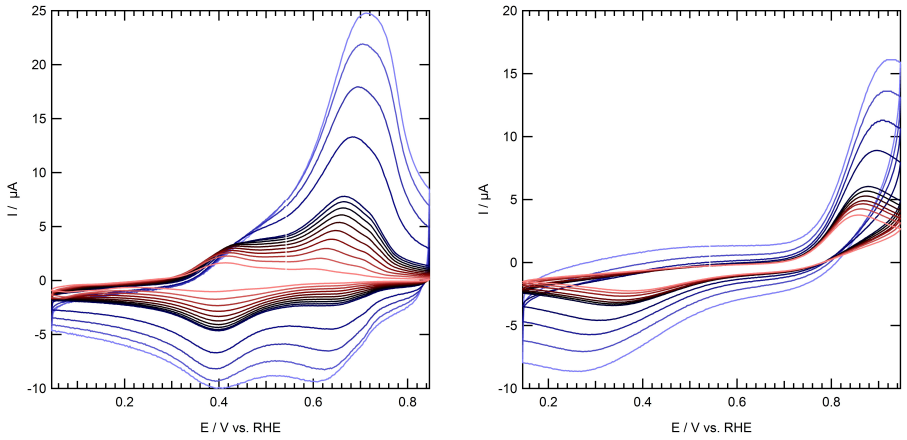

Figure 4.5: Cyclic voltammogram at scanrates from 10 (red line) to 500 (blue line) mV s^{-1} of a gold electrode with 1 mM solutions of a) 2,2'-bipyridine and b) 4,9-dimethyl-1,10-phenanthroline together with 0.1 mM Cu^{II}, 0.1 M phosphate buffer and 0.05 M NaCl acidified to pH 4 using HCl.

generated copper phenanthroline complexes (Figure 4.8). On a bare gold electrode, oxygen reduction starts at 0.36 V *versus* RHE. A maximum activity of -20 µA at the vertex potential of 0.24 V *versus* RHE is observed. Oxygen reduction with an *in situ* generated complex from 1 mM 1,10-phenanthroline and 0.1 mM Cu^{II}, a reductive current is observed starting around 0.44 V *versus* RHE. A starting potential of 0.44 V indicates a high overpotential of 800 mV. A shoulder is observed around 0.35 V, the same potential where oxygen reduction started on a bare gold electrode. The maximum activity of 11 µA is observed at the vertex potential of 0.24 V, which is lower than the activity on the bare gold electrode at the same potential. With oxygen reduction by *in situ* generated copper complex with 3 mM 1,10-phenanthroline and 1 mM Cu^{II}, an onset potential of 0.41 V *versus* RHE is observed, similar to the onset potential of the bare gold electrode. The maximum activity is 13 µA at the vertex potential of 0.24 V, which is slightly higher than the 10:1 complex, but still lower than the bare gold electrode. When the complexes from 1 mM Cu^{II} and 2 mM 1,10-phenanthroline are generated *in situ*, the onset potential is 0.44 V *ver-*

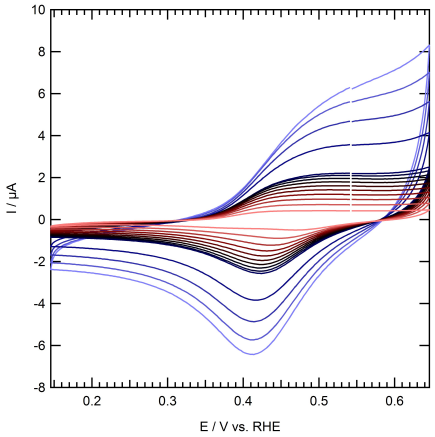

Figure 4.6: Cyclic voltammograms of a gold electrode under argon in a 1 mM solution of Cu^{II} and 2 mM 1,10-phenanthroline in a 0.1 M phosphate buffer with 0.05 M NaCl acidified to pH 4 at 500 (top blue line) to 10 mV s^{-1} (lowest orange line).

sus RHE, which is the same as the 0.1 mM Cu^{II} and 1 mM 1,10-phenanthroline situation. From 0.3 V, the current increases in line with the profile of the bare gold electrode, albeit the current is slightly lower than that of the bare gold. The maximum current is observed at the vertex potential and is 18 µA. The observed current for 1 mM 1,10-phenanthroline with 1 mM Cu^{II} in solution differs greatly from the other measurements. The current starts increasing at 0.45 V and keeps increasing until it reaches a plateau at 0.38 V *versus* RHE. The maximum current observed is 23 µA. The current observed is thus higher than the bare gold electrode and has a higher start potential than the gold electrode. The reductive current indicated the *in situ* generated complex is an active oxygen reduction catalyst.

4.4 Discussion

The fast ligand exchange kinetics of copper complexes in combination with the redox processes taking place in an electrochemical cell account for a complex picture regarding which species present in the electrolyte solution and which species is responsible for the oxygen reduction catalysis. As far as the ligand exchange equilibria are concerned, zero (free copper), one or two

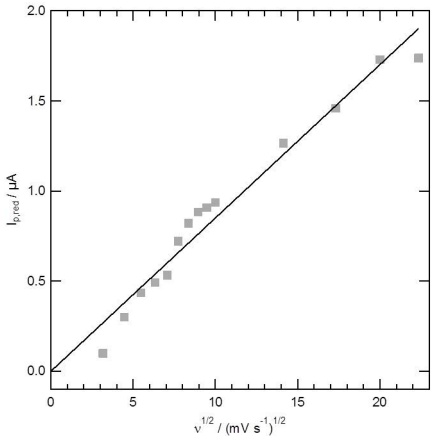

Figure 4.7: Peak current of the reduction peak *versus* the square root of the scanrate for the investigation of the homogeneity of the *in situ* generated copper-phenanthroline complex.

1,10-phenanthroline ligands can be ligated to copper. In the potential window where oxygen reduction is taking place, Cu^0, Cu^I and Cu^{II} can be expected. This leads to the following equilibria that need to be taken into account.

$$Cu^0 \rightleftharpoons Cu^I + e^- \tag{4.3}$$

$$Cu^0 \rightleftharpoons Cu^{II} + 2e^- \tag{4.4}$$

$$Cu^IL \rightleftharpoons Cu^{II}L + e^- \tag{4.5}$$

$$Cu^IL_2 \rightleftharpoons Cu^{II}L_2 + e^- \tag{4.6}$$

$$Cu^{II} + L \rightleftharpoons Cu^{II}L \tag{4.7}$$

$$Cu^I + L \rightleftharpoons Cu^IL \tag{4.8}$$

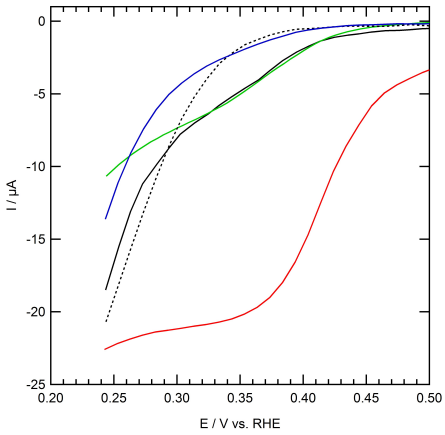

Figure 4.8: Oxygen reduction at a gold electrode with *in situ* generated copper-phenanthroline complexes with 0.1 mM Cu^{II} and 1 mM 1,10-phenanthroline (green line), 1 mM Cu^{II} and 1 mM 1,10-phenanthroline (red line), 1 mM Cu^{II} and 2 mM 1,10-phenanthroline (black solid line), 1 mM Cu^{II} and 3 mM 1,10-phenanthroline (blue line) and without any catalyst in solution (black dotted line) in a 0.1 M phosphate buffer with 0.05 M NaCl acidified to pH 4 using HCl.

$$Cu^{II}L + L \rightleftharpoons Cu^{II}L_2 \tag{4.9}$$

$$Cu^{I}L + L \rightleftharpoons Cu^{I}L_2 \tag{4.10}$$

Equations 4.3 and 4.4 is the deposition of free copper from solution onto the electrode. The reactions can happen coupled to Equations 4.7 and 4.8, which are the dissociation of the only 1,10-phenanthroline ligand on the copper center. Upon dissociation of the ligand, free copper is formed which can deposit electrochemically to the electrode surface. The deposit formed on the electrode is apparently not active in the oxygen reduction reaction. Equations 4.5 and 4.6 display the redox couple of the Cu^{I}/Cu^{II} complexes in solution. Equation 4.5 is the irreversible redox couple observed in the 1:1 ligand to copper ratio, while Equation 4.6 is the reversible redox couple observed when a ratio of 2:1 and higher is used. Based on the oxygen reduction activity displayed in Figure 4.8 the (reduced form of) $Cu^{II}L_2$ is inactive towards oxygen reduction as the activity observed is similar to that of a bare gold electrode. The catalytically active species is most likely the reduced form of $Cu^{II}L$ complex, which is predominantly present when a 1:1 ratio of copper ions to 1,10-phenanthroline is used (Figures 4.2 and 4.8).

The adsorbed $[Cu^{II}(DMP)]^{2+}_{ads}$ complex reported by Anson and Zhang has a 280 mV lower overpotential than the 1:1 copper to 1,10-phenanthroline complex in this paper.[10] A comparison of the electrochemical activity is difficult as there is no electrode surface area reported in the report by Anson and Zhang. The oxygen reduction reaction with *in situ* generated complexes

$[Cu(tmpa)(CH_3CN)](OTf)_2$ (tmpa = tris(2-pyridylmethyl)amine) is a catalyst for the electroreduction of oxygen developed in our group.[15] Both the complex $[Cu(tmpa)(CH_3CN)](OTf)_2$ and the *in situ* generated complex with a 1:1 ratio ligand to copper have one ligand attached to the copper. However the tmpa ligand has 4 coordinating nitrogen atoms which compares to two in 1,10-phenanthroline. Given that the copper center in the complex $[Cu(tmpa)(CH_3CN)](OTf)_2$ is ligated by four nitrogen donors, it is remarkable that the 2:1 complex of 1,10-phenanthroline to copper shows no activity towards oxygen reduction whatsoever.

The catalytic activity of the $[Cu(tmpa)(CH_3CN)](OTf)_2$ system is thereby significantly faster than the 1:1 complex of 1 mM Cu^{II} and 1,10-phenanthroline investigated in this work. A catalytic oxygen reduction current of approximately 1.5 mA cm^{-2} is observed on glassy carbon

with 1.0 μM [Cu(tmpa)(CH_3CN)]$(OTf)_2$ in solution whereas the Cu-phen complex obtains only 0.4 mA cm^{-2} at a 1 mM catalyst concentration. It would be interesting to compare the turnover frequencies of [Cu(tmpa)(CH_3CN)]$(OTf)_2$ and the 1:1 copper to 1,10-phenanthroline complex. Yet due to the irreversible behavior of the reduction of the this species, accompanied by deposition on the electrode obstructs us from using the foot of the wave analysis as performed in the [Cu(tmpa)(CH_3CN)]$(OTf)_2$ study.[15, 16] Since there is competition between oxygen reduction with a 1:1 copper complex and the formation of a copper deposit on the electrode surface, a strategy to prevent the formation of a copper deposit was developed. This is discussed in Chapter 5.

4.5 Conclusion

An active oxygen reduction catalyst is formed at a 1:1 phenanthroline to copper ratio. This complex does not show a reversible Cu^{I}/Cu^{II} redox couple. Therefore it is likely that formation of metallic copper on the electrode surface. We anticipate that immobilization of the gold surface with phenanthroline 1) prevents deposition of copper on gold even though free copper is present in solution and 2) spontaneously forms an active layer of copper phenanthroline species in the presence of copper salts in solution. This strategy is discussed in Chapter 5.

4.6 References

(1) Fernández, E. M.; Moses, P. G.; Toftelund, A.; Hansen, H. A.; Martínez, J. I.; Abild-Pedersen, F.; Kleis, J.; Hinnemann, B.; Rossmeisl, J.; Bligaard, T.; Nørskov, J. K. *Angew. Chem. Int. Ed.* **2008**, *47*, 4683–4686.

(2) Koper, M. T. M. *J. Electroanal. Chem.* **2011**, *660*, 254–260.

(3) Cracknell, J. A.; Vincent, K. A.; Armstrong, F. A. *Chem. Rev.* **2008**, *108*, 2439–2461.

(4) Reedijk, J. *Platin. Met. Rev.* **2008**, *52*, 2–11.

(5) Taube, H. *Chem. Rev.* **1952**, *50*, 69–126.

(6) Aznar, E.; Ferrer, S.; Borrás, J.; Lloret, F.; Liu-González, M.; Rodríguez-Prieto, H.; García-Granda, S. *Eur. J. Inorg. Chem.* **2006**, *2006*, 5115–5125.

(7) Thorum, M. S.; Yadav, J.; Gewirth, A. A. *Angew. Chem. Int. Ed.* **2009**, *48*, 165–167.

(8) Hoang, T. T. H.; Ma, S.; Gold, J. I.; Kenis, P. J. A.; Gewirth, A. A. *ACS Catal.* **2017**, *7*, 3313–3321.

(9) Van Dijk, B.; Hofmann, J. P.; Hetterscheid, D. G. H. *Phys. Chem. Chem. Phys.* **2018**, *20*, 19625–19634.

(10) Zhang, J.; Anson, F. C. *Electrochim. Acta* **1993**, *38*, 2423–2429.

(11) Zhang, J.; Anson, F. C. *J. Electroanal. Chem.* **1992**, *341*, 323–341.

(12) Lei, Y.; Anson, F. C. *Inorg. Chem.* **1994**, *33*, 5003–5009.

(13) Garribba, E.; Micera, G. *J. Chem. Educ.* **2006**, *83*, 1229.

(14) Burgess, J.; Haines, R. I. *J. Chem. Eng. Data* **1978**, *23*, DOI: 10.0.

(15) Langerman, M. P.; Hetterscheid, D. G. H. *Submitted*.

(16) Costentin, C.; Drouet, S.; Robert, M.; Savéant, J.-M. *J. Am. Chem. Soc.* **2012**, *134*, 11235–11242.

5 | Phenanthroline immobilized on Au electrodes as ligand in copper-mediated oxygen reduction

Abstract

Upon the electrochemical reduction of an *in situ* generated 5-diazo-1,10-phenanthroline ion (**1**-NH_2^+), **1** can be covalently attached to a gold electrode. The grafted molecules act as ligand when brought in contact with a copper-containing electrolyte solution. As the ligands are limited in spatial movement, the formation of complexes with only one phenanthroline ligand is ensured. The *in situ* generated complexes are investigated in the oxygen reduction reaction. An overpotential of 800 mV is observed in the oxygen reduction reaction. During catalysis a thick copper layer is formed on the electrode surface, which covers the organic layer. Catalyst deactivation occurs due to a chemical transformation of the grafted layer and the partial disappearance of the organic layer.

"Earth is presently in a period of increasing heat released over time from many sources."
Patrick Dugan

In preparation for publication

5.1 Introduction

In the previous chapter, the oxygen reduction reaction was investigated with *in situ* generated copper phenanthroline complexes. Oxygen reduction with *in situ* generated copper complexes is only efficient with 1 to 1 ratio complex of copper to 1,10-phenanthroline was used, as higher ratios of 1,10-phenanthroline to copper yield little to no oxygen reduction activity.

Due to the low barrier for ligand exchange at copper, free copper is readily formed in solutions of copper ligated to one equivalent of phenanthroline. This results in deposition of a metallic copper layer on electrode surfaces under reductive potentials. As was shown in Chapter 3, also tridentate ligands can decoordinate under reductive conditions, forming a metallic copper layer on the electrode surface.

By immobilizing the 1,10-phenanthroline covalently to a gold electrode, the formation of a copper deposit on the gold surface is prevented, since gold surface is completely coated by the organic ligand (see Figure 5.1). In order to prevent the loss of copper from the surface adsorbed ligands, Cu^{II} is kept in the electrolyte solution during catalysis. This means that a large amount of copper which is present in the electrolyte solution is not catalytically active. The surface is no longer available for the deposition of copper and thus any catalytic activity observed should be from a molecular complex present at the electrode surface.

In the group of Chidsey, oxygen reduction was investigated using a copper complex with a 3-ethynyl-1,10-phenanthroline ligand immobilized covalently to an azide modified glassy carbon electrodes was investigated.[1] Oxygen reduction was determined to be second order in copper complex loading on the electrode surface. This means the triazole linker give the complexes on the electrode surface enough mobility to form a dinuclear complex on the electrode surface with oxygen bridging between the two copper centers. No copper was present in the electrolyte solution and the copper could be decoordinated by adding sodium diethyldithiocarbamate, a strongly copper chelating ion. No long term stability experiments were reported. One could imagine copper dissociating from the surface adsorbed ligand and leaching into the electrolyte, resulting in a loss of activity.

The formation of a surface adsorbed dimer should lead to second order kinetics in copper. By immobilizing the phenanthroline molecule to the electrode surface directly, thus without the

triazole linker used by Chidsey *et al*, a rigid system is formed. The surface adsorbed complexes do not have the mobility to form dimers as the phenanthroline molecules are retained in a perpendicular fashion to the electrode surface.

The immobilization of organic molecules on electrode surfaces has been of interest over the last decades.[2–10] One possibility of immobilization is by forming a covalent bond which is formed by reducing a diazonium compound.[2, 4–6, 10] This diazonium cation can be formed *in situ* by the addition of sodium nitrite to an organic molecule containing an amine (Figure 5.2). The diazonium ion in turn is reduced in close proximity to the working electrode under reductive conditions and liberates nitrogen in the process. A radical remains on the position of the diazonium moiety. This radical can couple to the electrode, forming a covalent bond.

An advantage of the immobilization of **1** via the reduction of a diazonium ion is that it forms thin layers on the electrode.[5] Upon the reduction of 5-diazo-1,10-phenanthroline (**1**-N_2^+) at glassy carbon electrodes an organic layer with a thickness of 2 nm is formed.[6] Immobilization of **1** can also be performed by the reduction of 5-bromo-1,10-phenanthroline.[9] The thickness of the layer formed upon the reduction of 5-bromo-1,10-phenanthroline is 125 nm, which is much thicker than the layer formed by the reduction of **1**-N_2^+. Also the reduction of 1,10-phenanthroline itself leads to formation of an organic layer on the electrode. This direct reduction of 1,10-phenanthroline at glassy carbon electrodes happens at adsorbed 1,10-phenanthroline molecules via a proton coupled electron transfer step which leads to the formation of a carbon centered radical at the 4-position. The radical couples with the glassy carbon electrode, resulting in the loss of aromaticity on on one of the phenyl rings. The thickness of the organic layer on the electrode is approximately 2 nm thick, similar to the layer formed by the reduction of **1**-N_2^+.[6] Upon direct reduction of 1,10-phenanthroline,the molecules are in this case more upright than in the case of **1**-N_2^+. We anticipate that the geometry of the molecules at the electrode surface is more advantageous in the case of reduction of **1**-N_2^+ than of 1,10-phenanthroline.

The proposed mechanism of the reduction of diazonium ions does include the formation of a radical. Such radicals are highly reactive and consequently react with other radicals, forming diamagnetic dimers which do not attach to the electrode surface. It is also possible that the radicals react with molecules which are already attached to the electrode surface, forming thick

layers of organic material on the electrode surface. This has been observed in the immobilization of 1,10-phenanthroline on glassy carbon electrodes.[6] Analysis of AFM studies of the grafted layer points to a layer thickness of 2 nm, which is more than twice the length of a phenanthroline molecule in the gas phase. The generated radicals may also react with residual oxygen. In summary, these side reactions mean the efficiency of the immobilization reaction can be rather low.

In this work, we present the covalent immobilization of 1,10-phenanthroline attached to gold surface by reduction of *in situ* generated 1,10-phenanthroline-5-diazonium ion. The immobilized phenanthroline moiety functions as a ligand for copper, which in turn is studied for the oxygen reduction reaction.

Copper ions are kept in solution during oxygen reduction in order to ensure the presence of copper near the electrode surface. These conditions were chosen because due to the fast ligand exchange kinetics copper will leach into the electrolyte if it is not present in the electrolyte solution. The catalytic experiments were performed in Cl^- containing electrolyte and acidified to ph 4, since Cu^{2+} does not dissolve in perchlorate containing electrolyte solutions.

5.2 Experimental

5.2.1 Reagents and materials

1,10-phenanthroline-5-amine (Sigma Aldrich, 97%), 4-bromoaniline (Sigma Aldrich, 99%), $NaNO_2$ (Merck, 99.9%), $K_3Fe(CN)_6$ (Sigma Aldrich, 99.98%) and $Cu(OTf)_2$ (Alfa Aesar, $\geq$ 99%) were used as received.

Electrolyte solutions were prepared with $HClO_4$ (Merck suprapur, 70 %), HCl (Merck, 37 %), Na_2HPO_4 (Merck, 99.9%), NaH_2PO_4 (Merck, 99.9 %), NaCl (Merck, 99.9 %) and were prepared with MilliQ water ($>$ 18.2 MΩ cm resistivity).

Argon and dioxygen (5.0) were purchased from Linde Gas.

5.2.2 Electrochemical methods

All electrochemical experiments were performed on an Autolab PGSTAT 128N with integrated EQCM module in one-compartment 25 ml glass cells in three-electrode setups. A gold working electrode (99.995 %, Alfa Aesar, 0.05 cm^2 geometric surface area) was used in a hanging meniscus configuration. Platinum (99.99%, Alfa Aesar) was used as a counter electrode and a Ag/AgCl (3

M KCl) purchased from Autolab was used as reference electrode.

The Au electrode was cleaned by oxidation at 10 V *versus* a graphite rod counter electrode in 10% H_2SO_4 for 30 s. This was followed by a 6 M HCl bath for 20 s, followed by flame annealing. The electrode was then electrochemically polished by cycling between 0 and 1.75 V *versus* RHE (E_{start} = 0.7 V) at 1 V s^{-1} in 0.1 M $HClO_4$.

Modification of gold electrodes was performed in 0.5 M HCl electrolyte with 1 mM 1,10-phenanthroline-5-amine (97%, Sigma Aldrich) or 4-bromoaniline (99 %, Sigma Aldrich). The solution was deaerated for 30 min with argon (Linde 5.0). After deaeration, 3.4 mg $NaNO_2$ (puriss, Sigma Aldrich) was added to the electrolyte solution. After 60 seconds, argon was blanketed over the electrolyte solution and a cyclic voltammogram was started. For the 4-bromoaniline, the Au electrode was cycled between -0.5 and 0.5 V *versus* Ag/AgCl at 100 mV s^{-1} for 5 cycles. For 1,10-phenanthroline-5-amine, the Au was cycled -0.2 and 0.3 V *versus* Ag/AgCl at 50 mV s^{-1} for 10 cycles.

Oxygen reduction experiments were performed in 0.05 M NaH_2PO_4 (99.99 %, Merck), 0.05 M Na_2HPO_4 (99.99 %, Merck), 0.05 M NaCl (99.99 %, Merck) and 0.6 mM HCl (37 %, VWR International). In case of catalytic experiments, 1 mM $Cu(OTf)_2$ was added to the electrolyte solution. Prior to oxygen reduction experiments, oxygen was bubbled through the electrolyte for at least 20 minutes, while during experiment, oxygen was blown over the solution.

Apart from the EQCM experiments and the experiments wherein the XPS samples are created, all electrochemical experiments were performed in a hanging meniscus configuration. In a hanging meniscus configuration, the electrode is situated in the headspace-electrolyte interface (left panel Figure 5.3). Prior to experiment, the electrode is not in contact with the electrolyte solution. The electrolyte containing 1 mM 1,10-phenanthroline-5-amine or 4-bromoanaline is deaerated using argon. After deaeration sodium nitrite is added as a solid to the electrolyte. One minute after addition of sodium nitrite, argon is blown over the headspace and the working electrode is brought in contact with the electrolyte, making a hanging meniscus. The area of contact between different experiments can differ slightly due to differences in the meniscus that is made.

5.2.3 EQCM setup

The electrochemical quartz crystal microbalance consisted of a PEEK cell purchased from Autolab. The cell was degassed with Ar (Linde, 5.0) prior to experiment. A gold working electrode (0.35 cm^2 geometric surface area) on a quartz crystal was used as received. Platinum was used as counter electrode and the experiments were measured *versus* a Ag/AgCl (3M KCl)reference electrode.

In the EQCM setup, the electrode is situated in the bottom of the cell (see right panel of Figure 5.3). This contrasts the electrochemical experiments wherein a hanging meniscus configuration was used, where the electrode sits in the liquid-headspace interface. The electrolyte-electrode interface cannot be broken during deaeration, thus in the EQCM setup the electrode is in contact with the electrolyte during deaeration. During this time, no potential is applied to the working electrode. Upon addition of sodium nitrite, the counter and reference electrodes are inserted into the electrolyte and the standby potential is applied. After one minute, cyclic voltammetry is started.

Since the EQCM oscillator needs to be warmed up prior to experiments, the cell was filled with 3 ml MilliQ water and the oscillator was turned on for 30 minutes. Simultaneously, the electrolyte solutions were prepared as described above. In quick succession, the following steps were taken: the $NaNO_2$ was added to the electrolyte solution; the EQCM oscillator was turned off; the MilliQ water in the EQCM cell replaced with the electrolyte solution and the oscillator was turned on. The modification was then started as described above.

5.3 Results and discussion

5.3.1 The reduction of diazonium ions for the covalent coupling of organic molecules to electrode surfaces

Since the reduction of diazonium compounds are highly dependent on the size of the electrode, a well-documented example from literature was reproduced. By reduction of *in situ* generated 4-bromobenzene-diazonium (**2**-N_2^+), **2** can be immobilized on the surface of the electrode. **2** is not expected to coordinate copper, when $Cu(OTf)_2$ is dissolved in the electrolyte. Moreover, the grafted layer formed on the electrode surface is not able to transfer electrons from the electrode

to any redox-active species in the electrolyte solution. Therefore, copper from the electrolyte solution is not expected to form an active oxygen reduction catalyst.

Figure 5.4 illustrates the formation of **2** attached to gold (Au|**2**) via *in situ* reduction of 4-bromobenzene-diazonium (**2**-N_2^+). 5-diazo-1,10-phenanthroline(**1**-N_2^+) is generated *in situ* and reductively coupled to gold electrodes (Au|**1**, bottom panel in Figure 5.4). In contrast, **1** will be able to coordinate to copper and thus form a molecular oxygen reduction catalyst at the surface of the working electrode.

5.3.2 Coupling of 2 to gold electrodes by reduction of *in situ* generated 4-bromobenzene-diazonium

Several aryldiazonium compounds have been used to immobilize benzylic molecules at gold [2, 10] and glassy carbon electrodes.[4, 5, 10] In the group of Bèlanger, it was discovered a glassy carbon electrode grafted with **2** contains 0.38 nmol cm^{-2} using XPS.[4] In the cyclic voltammogram of reduction of **2** at glassy carbon, two peaks are observed. The first reduction peak is observed at 0.71 V *versus* RHE.[10] The nature of this peak is at present not fully understood. By scanning the potential up to this peak, partial blocking of the surface is observed in $K_3[Fe(CN)_6]$ blocking experiments. This peak is thus already associated with the reduction of **2**-N_2^+, but does not form a fully covered surface. The second reduction is associated with the reductive coupling of **2**-N_2^+ and **2**$^\bullet$ to the electrode surface and is observed at -0.09 V *versus* RHE. The peak is followed by a plateau reaching the vertex potential at -0.79 V *versus* RHE, which is also associated with the reduction of **2**-N_2^+ and the **2** radical. In the second scan of the cyclic voltammogram, the reductive peak is no longer visible.

Gooding *et al.* immobilized **2** via the reduction of the *in situ* generated **2**-N_2^+ at gold electrodes.[10] In the first scan of the cyclic voltammogram at a gold electrode, a reduction peak was reported at 0.36 V *versus* RHE. The peak is followed by a plateau. In the backward scan, the current drops to 0 A quickly. The reductive peak and the plateau are associated with the reduction of **2**-N_2^+ at the gold electrode. In the second scan, the peak and plateau are no longer visible. The differences in the cyclic voltammetry between glassy carbon and gold electrodes indicate the coupling of organic molecules is dependent on the electrode material and consequently that it is impossible to directly compare the reduction of diazonium ions at different electrode materials.

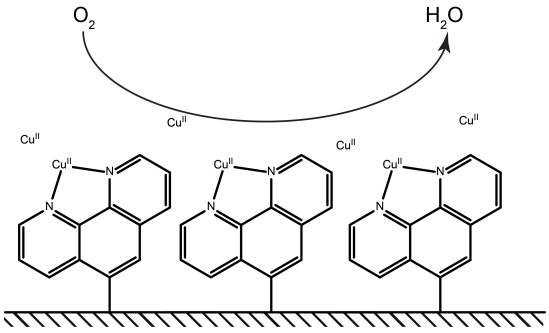

Figure 5.1: Schematic representations of inaccessibility of the gold surface due to the covalent attachment of organic molecules onto gold electrodes.

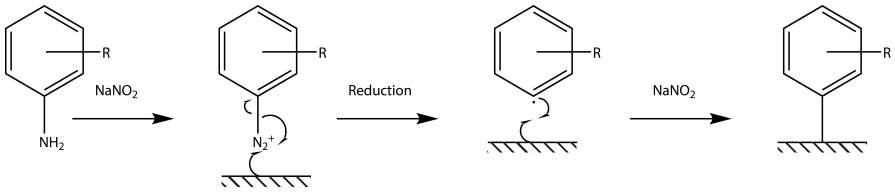

Figure 5.2: Generalized mechanism for the formation of a covalent bond between an electrode and an organic molecule by the reduction of an *in situ* generated diazonium ion.

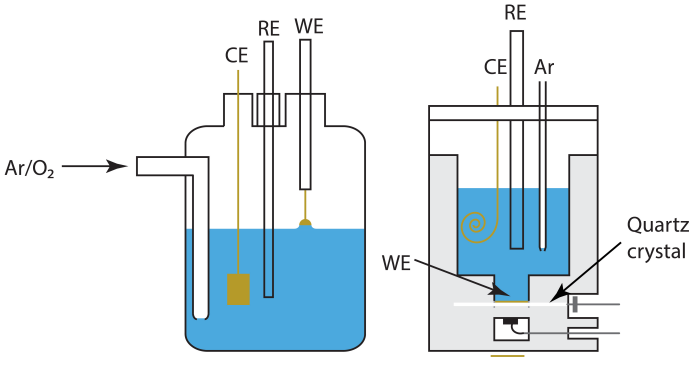

Figure 5.3: Schematic representations of electrochemical cells with an electrode used in hanging meniscus configuration (left) and the electrode sitting in the bottom of the EQCM cell (right)

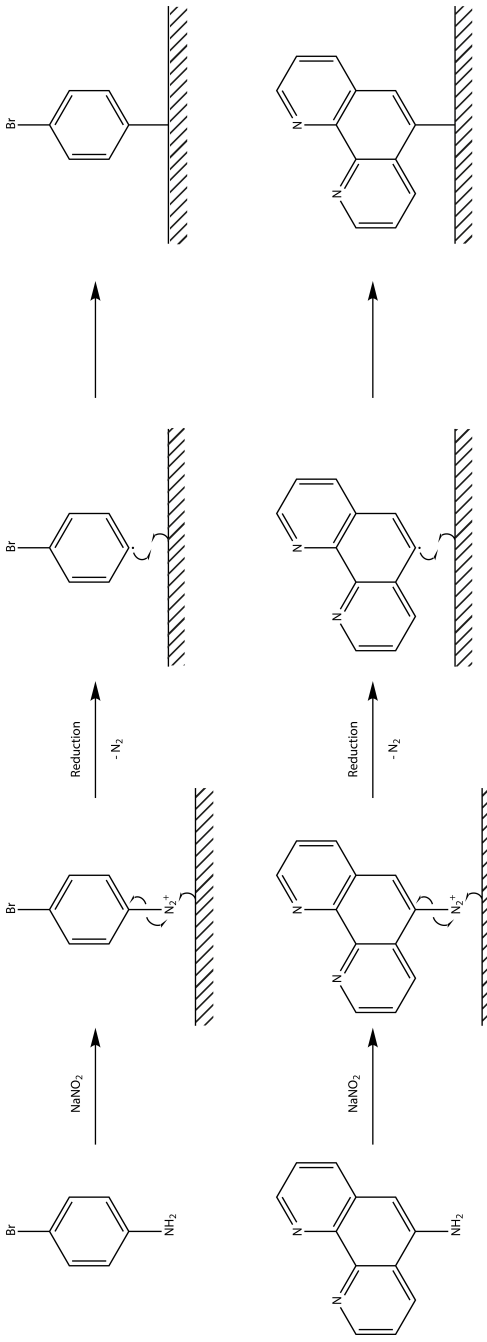

Figure 5.4: Proposed reaction mechanism of the immobilization of **2** (top) and **1** (bottom) onto a gold electrode by reduction of *in situ* generated diazonium ions.

In this study, the reductive coupling of **2** with the gold electrode was performed in a hanging meniscus configuration. In the first scan of the immobilization of **2**, a sharp reductive peak is observed at 0.34 V *versus* RHE. In the backward scan the current rapidly decreases to 0 A. The consecutive scan shows no reductive currents anymore, which indicates that the surface is fully covered with **2** after a single scan while scanning at 100 mV s^{-1}. No oxidation processes are observed between 0.71 and -0.29 V *versus* RHE in all the scans, indicating that no oxidative degradation of the organic layer takes place. The results reported here are in good agreement with the electrochemistry of **2**-NH_2 reported by Gooding *et al*. The formation of Au|**2** was further investigated using EQCM.

There is a difference in the surface area between the EQCM electrode (0.39 cm^2 real surface area) and the hanging meniscus electrode (0.05 cm^2 real surface area). Therefore differences in immobilization kinetics are expected due to different diffusion patterns. The real surface area of the working electrodes was determined *ex situ* by measuring the charge transferred during the reduction of the gold oxide formed in 0.1 M $HClO_4$ electrolyte solution.[11]

Using EQCM, the amount of **2** grafted onto the electrode surface was quantified. The reduction of the diazonium ion starts at 0.41 V *versus* RHE, as it did on the gold electrode in hanging meniscus configuration described above. A slow reduction process is observed over the whole forward scan below 0.41 V. The shape of the slow reduction of **2**-N_2^+ shown in the cyclic voltammogram is different from the cyclic voltammogram in hanging meniscus configuration due to the differences in diffusion behavior (see Figures 5.5 and 5.6). The total mass increase over the first scan is 145 ng cm^{-2}, as is shown in the top panel of Figure 5.6, which corresponds to approximately 0.9 nmol cm^{-2}.

The unit cell of a gold FCC latice has a lattice constant of 406.5 pm.[12] Since the diagonal of one of the faces contains 2 whole atomic diameters, one can calculate the atomic radius in the FCC lattice using Equation 5.1, where a is the lattice constant and r is the radius of a gold atom in the lattice.

$$(4\mathrm{r})^2 = 2\mathrm{a}^2 \text{ or } \mathrm{r} = \frac{1}{2\sqrt{2}}\mathrm{a} \text{ or } \mathrm{r} = \frac{1}{2\sqrt{2}} \times 406.5 = 143 \text{ pm} \tag{5.1}$$

One gold atom in the (111) latices takes up 7.16×10^{-16} cm^2. The total surface of the EQCM electrode thus contains approximately 5.45×10^{14} atoms. This indicates a coverage of

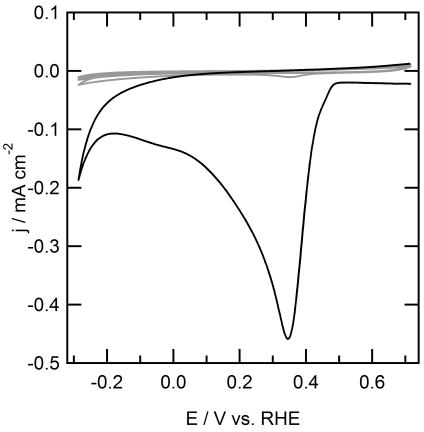

Figure 5.5: First scan (solid line) and second scan (dotted line) of electrochemical immobilization of **2** at a gold electrode (1.5 cm^2) in combination with EQCM of bromobenzene by reduction of a 1 mM **2**-N_2^+ ion solution generated *in situ* by addition of 4-bromoaniline and sodium nitrite to form a 1 mM solution of both in 0.5 M HCl electrolyte solution at 100 mV s^{-1}.

approximately 40 molecules of **2** per 100 gold atoms.

The total deposition of **2** measured by EQCM at a gold electrode (0.9 nmol cm^{-2}) is higher than the coverage found in the group of Bèlanger on glassy carbon electrodes measured *ex situ* by XPS spectroscopy (0.38 nmol cm^{-2}).[4]

During the reduction of the diazonium salts, carbon centered radicals are formed as intermediates (see Figure 5.2). These radicals are highly reactive, can dimerize or react with other species in solution, which results in a low faradaic efficiency. During the first cycle of the cyclic voltammogram, 371 μC cm^{-2} reductive current has been recorded. This means the faradaic efficiency of the formation of a Au-**2** bond by reduction of **2**-N_2^+ is approximately 48%.

In an outer sphere electron transfer process, there is no interaction between the electrode and a dissolved redox species. The electron transfer happens via tunneling through the electrolyte. An adsorbed layer on the electrode surface can block the tunneling of the electrons to the electrode if the layer adsorbed is thick enough and is not conducting. This allows us to investigate the conductivity of the grafted layers using a redox probe in solution. The conductivity

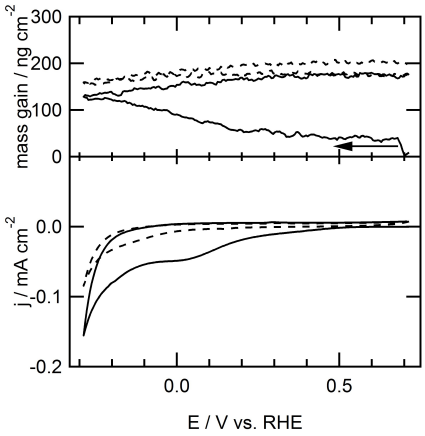

Figure 5.6: First scan (solid line) and second scan (dotted line) of electrochemical immobilization of **2** at a gold electrode (1.5 cm^2) in combination with EQCM of bromobenzene by reduction of a 1 mM **2**-N_2^+ ion solution generated *in situ* by addition of 4-bromoaniline and sodium nitrite to form a 1 mM solution of both in 0.5 M HCl electrolyte solution at 100 mV s^{-1}.

is of importance since during oxygen reduction, electrons need to transfer from the electrode to dissolved copper in the electrolyte in the blank. If no electron transfer is possible, no oxygen reduction activity is expected from dissolved copper species. When electron transfer through a grafted layer is observed, oxygen reduction could be a possibility. This should help predict the oxygen reduction behavior of the different grafted layers. For these experiments, $K_3[Fe(CN)_6]$ was used as it is known to react via outer sphere electron transfer processes.[10]

Gooding *et al.* attribute a redox couple with $E_{1/2} = 0.22$ V *versus* Ag/AgCl at a glassy carbon electrode to $K_3[Fe(CN)_6]$ via outer sphere electron transfer.[10] In the reduction of *in situ* generated **2**-N_2^+ on glassy carbon electrodes, two reduction events were observed, a first reduction peak at 0.71 V and a second reduction peak at -0.09 V *versus* RHE. By grafting the electrode over both reduction peaks, no redox chemistry of $K_3[Fe(CN)_6]$ was observed, indicating a total blockage of electron transfer to and from the glassy carbon electrode. Since no redox activity with $K_3[Fe(CN)_6]$ was observed the grafted layer must be thick enough to prevent fast tunneling through the layer. By scanning the electrode up to only the first reduction at 0.71 V, the na-

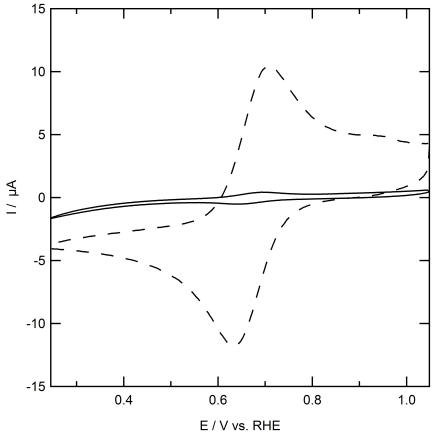

Figure 5.7: Outer sphere electron transfer at a gold electrode (dotted line) and a gold electrode modified with **2** using 1 mM $K_3[Fe(CN)_6]$ in 0.1 M phosphate buffer and 0.05 M NaCl at pH 7.

ture of the first reduction peak could be investigated. The peak current of the redox couple of $K_3[Fe(CN)_6]$ was halved, indicating the surface was partially blocked by **2**. This indicates grafting already starts at 0.71 V at a glassy carbon electrode. Apparently, full coverage of the surface has not been reached yet under these conditions.

In an outer sphere electron transfer process, there is no interaction between the electrode and the molecule in solution. Therefore the halfway potential ($E_{1/2}$) of the redox couple should remain the same. If the electron transfer kinetics becomes slower due to the presence of a grafted layer, an increase in ΔE is expected together with a lower maximum current. On a polished gold electrode, a Fe^{II}/Fe^{III} redox couple is observed with $E_{1/2}$ = 0.65 V (Figure 5.7). The peak of the oxidative wave is positioned at 0.29 V and with a peak current of 9.2 µA and the reductive peak lies at 0.61 V with a peak current of -10µA. If the surface is grafted with **2**, the current decreases twenty-fold while the peak potentials of the Fe^{II}/Fe^{III} redox couple remain more or less at the same position, with $E_{p,o}$ = 0.63 V and $E_{p,r}$ = 0.28 V, resulting in $E_{1/2}$ = 0.66 V. Since no apparent change in ΔE was observed, electron transfer must still occur at relatively fast rates. It therefore appears the surface of the gold electrode grafted with **2** is locally not completely covered. Since the surface exposed to the electrolyte might differ slightly each time a hanging meniscus is made,

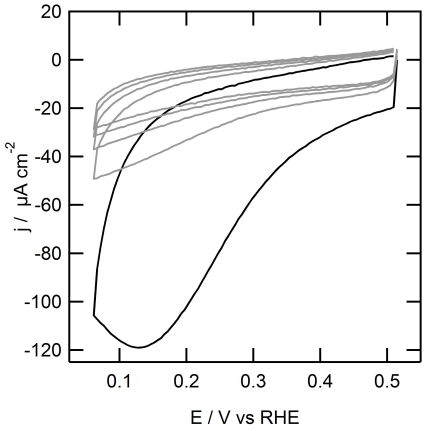

Figure 5.8: Immobilization of 1,10-phenanthroline on a gold electrode (0.05 cm^2) in hanging meniscus configuration from 1 mM **1**-N_2^+ ions formed*in situ* by addition of sodium nitrite and **1**-NH_2 to form a 1 mM solution of both to a 0.5 M HCl electrolyte solution at 50 mV s^{-1}.

the small redox couple observed after grafting is attributed to redox activity at parts of the gold electrode that was not exposed to the grafting electrolyte in the immobilization experiment.

5.3.3 Reductive coupling of *in situ* generated 5-diazo-1,10-phenanthroline to gold electrodes

The immobilization of **1** on glassy carbon electrodes was previously described by the group of Ekinci.[5] The immobilization was performed in 46% HBF_4 between -0.1 and -1.2 V *versus* Ag/AgCl (approximately 0.1 to -1.0 V *versus* RHE) at -4 ∘C at 200 mV s^{-1}, while sodium nitrite was added dissolved in acetonitrile. Already at -0.1 V *versus* Ag/AgCl, a reductive current was observed. A double reduction peak was observed in the first scan, the first at -0.7 and the second at -0.9 V *versus* Ag/AgCl, which were attributed to the reduction of protonated 1,10-phenanthroline-5-amine and of the *in situ* generated diazonium ion. In the second and consecutive scans, the current decreased significantly, but the two reduction peaks remained visible. The surface coverage was determined to be 0.68 nmol cm^{-2} by XPS. The amount of **1** that is actually available for coordination was determined in the presence of [$RuCl_3$]. By hanging the grafted electrode in a [$RuCl_3$] solution and investigating the redox chemistry of the electrode afterwards, the number

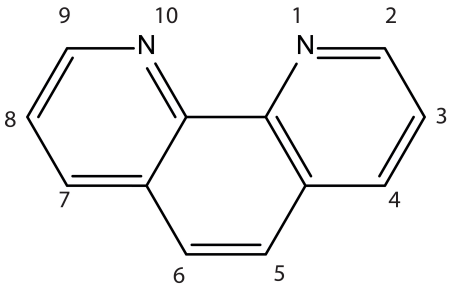

Figure 5.9: Numbering of substituents of 1,10-phenanthroline according to IUPAC convention.

of available sites on the surface was determined to be 0.36 nmol cm^{-2}.

Several other methods to immobilize phenanthroline onto gold electrodes have been reported as well.[6, 7, 9] In the group of Bertotti, 5-bromo-1,10-phenanthroline was reduced in DMF to form the radical on the 5- position on the phenanthroline ring either stepwise via 5-bromo-1,10-phenanthroline reduction to form a radical anion of 5-bromo-1,10-phenanthroline. Formation of this radical anion was followed by loss of Br^- leaving a radical at the position where the bromine left. At this position, phenanthroline, in turn could couple to the Au working electrode.[9] This forms a layer of Au|**1** on the electrode surface that in structure is identical to the reduction of the *in situ* generated **1**-NH_2. The thickness of the grafted layer was determined to be 125 nm using AFM. This indicates the formation of multiple layers of organic material on the surface of the electrode. Direct reductive coupling of 1,10-phenanthroline to glassy carbon was investigated in the group of Bèlanger.[6, 7] Reduction of 1,10-phenanthroline yields a coupling at the 4-position. On the other hand the reduction of *in situ* generated **1**-N_2^+ couples exclusively at the 5-position, since the radical formed on the phenanthroline molecule is situated in an sp-orbital and thus cannot migrate over the benzylic rings via its π-clouds. This implies that a different surface structure is obtained in case of **1**-N_2^+ reduction compared to reduction of 1,10-phenanthroline..

The reductive immobilization of **1** on gold was investigated using cyclic voltammetry in 0.5 M HCl solution (Figure 5.8). In contrast to the immobilization of **2**, the potential window was changed to 0.06 and 0.51 V, due to an oxidation observed above 0.51 V *versus* RHE. This oxidation is attributed to the formation of a ketone moiety on the 6-position.[3] At the start of the cyclic

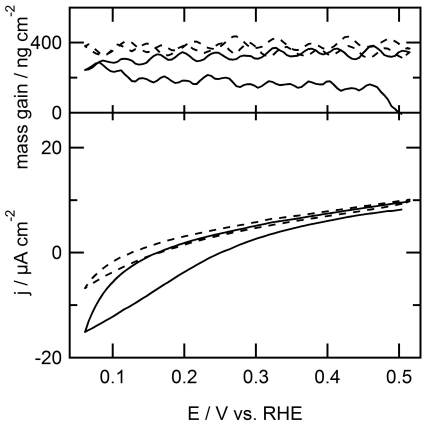

Figure 5.10: EQCM response of the first scan (solid line) and second scan (dotted line) of immobilization of **1** at a gold electrode (0.39 cm^2 geometric surface area) by reduction of a 1 mM **1**-N_2^+ ion solution generated *in situ* by addition of 1,10-phenanthroline-5-amine and sodium nitrite to form a 1 mM solution of both in 0.5 M HCl electrolyte solution at 50 mV s^{-1}.

voltammetry at 0.51 V, a reductive current is observed. The negative current increases as a more reducing potential is applied. At 0.11 V *versus* RHE, a peak is observed. In the backward scan, the current decreases rapidly. In each following scan, a decrease in current is observed at the vertex potential of 0.06 V. In the fifth and last scan, significant current can still be observed, suggesting **1**-N_2^+ is still being reduced in the fifth scan. Between different immobilization experiments of **1** under the same conditions, minor differences are observed with respect to the current and the peak position.

The amount of **1** that was immobilized on the gold electrode was quantified using EQCM (Figure 5.10). At the starting potential of 0.51 V an oxidative current of 8.2 µA is observed. It is unexpected that at the beginning of the experiment an oxidative current is observed. This current decreases linearly to 0 µA at 0.31 V *versus* RHE. Below 0.31 V, a reduction current is observed to continue to decrease until the vertex potential is reached. A weak shoulder can be observed between 0.21 and 0.11 V. In the backward scan, the current decreases to 0 A, after which a steady increase in oxidative current is observed increasing to 4 µA. Simultaneously with the

cyclic voltammetry experiment, the mass of the electrode was measured using a microbalance. The mass of the electrode increases between 0.42 and 0.27 V *versus* RHE. This mass increase continues in the backward scan up till 0.42 V. In the second scan, the mass remains stable, indicating that no further modification of the electrode takes place. Most likely an outer sphere electron transfer that reduces **1** takes place, which results in dimerization of **1** in the electrolyte solution.

The reductive coupling of **1** at the EQCM electrode and the associated mass changes are displayed in Figure 5.10. At the start of the experiment at 0.5 V, an oxidative current is observed. Initially, the apparent mass of the electrode increases between the vertex potential of 0.51 V and 0.46 V. This increase in mass is most likely not associated with the reductive addition of of **1** to the electrode surface. After all, a positive current is still being measured under these conditions, which is at present not understood. We therefore do not take into account the initial mass increase between 0.51 and 0.46 V. The mass of the electrode increased by 77 ng cm^{-2} in the part of the voltammogram where reductive current is observed. This corresponds to 0.4 nmol cm^{-2} or 18 molecules of **1** per 100 gold atoms. A maximum of 50 molecules of **1** can be deposited on the surface of a gold (111) electrode, according to modeling experiments on Au|**1** (shown in Figure 5.11). The diameter of gold is 144 pm as was determined from the lattice constant.[12] The length of **1** was determined to be 6.6 nm by measuring the length of the molecule in ChemBioDraw 3D after energy minimization by MM2

$K_3[Fe(CN)_6]$ was used as a redox probe to investigate the surface blocking properties of **1** attached to the gold working electrode (Figure 5.12). Both redox peaks broaden with respect to the redox probe at a bare gold electrode, with $E_{p,o}$ = 0.78 V and $E_{p,r}$ = 0.51 V. The halfway potential $E_{1/2}$ is 0.65 V, which, as expected, is similar to the value found for the bare gold electrode. The peak current at the Au|**1** system drops to 5 μA, which is approximately half the peak current observed at the bare gold electrode. This drop in peak current and increased peak separation indicates that the outer sphere electron transfer rates from the electrode to the solution are retarded.

The current observed in the outer sphere redox behavior of **1** on gold differs from the immobilization of **1** on GC reported in the group of Ekinci.[5] They observed a large decrease in current and do not report discernible redox peaks of the $K_3[Fe(CN)_6]$ redox couple, but rather a positive and negative plateau. The higher surface blocking of the electrode observed by Ekinci

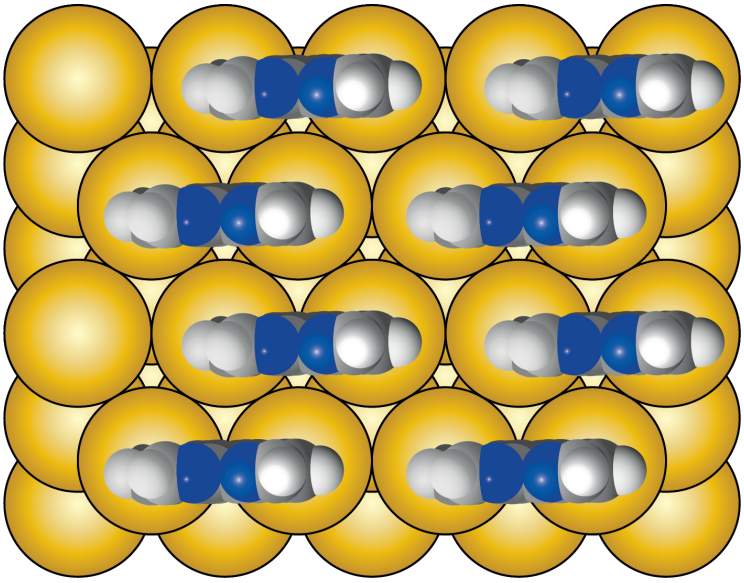

Figure 5.11: A gold (111) surface with the molecules of **1** for a well-ordered maximum surface coverage of 50 molecules of **1** per 100 Au surface atoms. The gold surface was made with the surface explorer[13] whereas the phenanthroline molecules were drawn in ChemBioDraw 3D. First an energy minimization was performed, after which the distance between the outer carbon atoms was measured. A gold diameter was 144 pm was selected.[12]

et al correlates well with the higher surface coverage that was observed in their experiments on glassy carbon.

5.3.4 Oxygen reduction activity of modified gold electrodes

In oxygen reduction experiments at immobilized catalysts it is important to rule out that any catalytic activity is due to uncovered electrode material. The activity of an unmodified gold electrode was therefore investigated between 0.63 and 0.23 V *versus* RHE in 0.1 M phosphate buffer and 0.05 M NaCl acidified to pH 4 using HCl. The onset potential for oxygen reduction is determined to be roughly 0.39 V, after which a catalytic wave is observed reaching -410 μA cm^{-2} at the lower vertex potential of 0.23 V.

Another important potential catalytic species that must be ruled out is deposition of copper

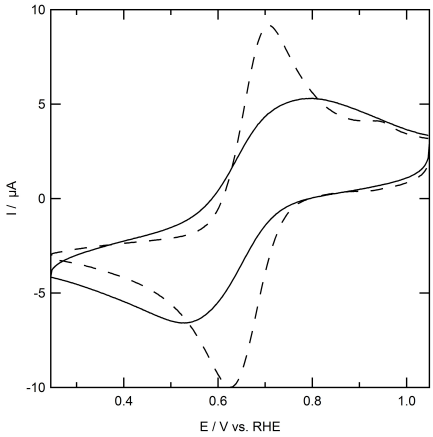

Figure 5.12: Outer sphere electron transfer at a gold electrode (dotted line) and a gold electrode modified with **1** using 1 mM $K_3[Fe(CN)_6]$ in 0.1 M phosphate buffer and 0.05 M NaCl at pH 7.

the gold electrode that forms under reductive potentials.[14, 15] Oxygen reduction at a gold electrode in presence of 1 mM Cu^{2+} was investigated using cyclic voltammetry between 0.25 and 0.75 V. In the cyclic voltammogram, a reductive current of -6 µA is observed at the vertex potential of 0.75 V *versus* RHE. Two reversible redox events are observed in the cyclic voltammogram of the Au|Cu^{II} system in presence of oxygen. The first redox couple has a reductive peak at 0.72 V and an oxidative peak above the vertex potential of 0.75 V. The second redox event has a reductive shoulder around 0.55 V, which underlies the other reductive peak and an oxidative peak at 0.72 V. These peaks are associated with copper deposition on the gold working electrode. Below 0.45 V, a catalytic wave is observed with a maximum current of -145 µA cm^{-2} at the vertex potential. It is surprising that oxygen reduction is suppressed by adding Cu^{2+} to the electrolyte solution. The current at 0.25 V in absence of Cu^{2+} is approximately three times higher than the current at a gold electrode in presence of Cu^{2+}.

At an electrode modified with **2** no outer sphere electron transfer with $K_3[Fe(CN)_6]$ is observed (see section 5.3.2). Since it is unlikely for **2** to bind copper ions from the solution. It is not expected that Au|**2**|Cu^{II} will show any oxygen reduction activity. The stability of such grafted layers is important to help understand the stability of Au|**1**. In the single sweep voltammetry of

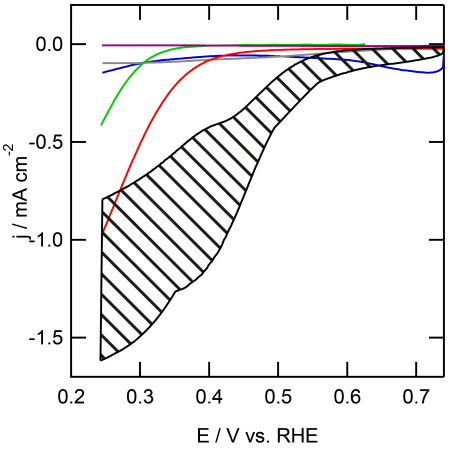

Figure 5.13: Electrochemical behavior of a bare gold electrode (green line), Au|**2**|Cu (purple), Au|Cu (blue line), Au|**1** (red line) and Au|**1**|Cu (black area) in presence of oxygen and Au|**1**|Cu in absence of copper (grey line) in 0.1 M phosphate buffer with 0.05 M NaCl acidified to pH 4 with HCl at 100 mV s^{-1}. The black area represents the spread of current observed over different oxygen reduction experiments.

Au|**2**|Cu^{II} in presence of oxygen, no current is observed. This shows that it is therefore possible to block oxygen reduction by grafting the electrode surface with a layer of organic molecules, even in the presence of dissolved copper species. Since no outer sphere electron transfer was observed with Au|**2**|Cu^{II}, two reasons for the absence of oxygen reduction could be given. First, there is the absence of electron transfer, meaning it is impossible to get electrons from the electrode to the surface via the grafted layer. Secondly, Au|**2** cannot coordinate to copper, indicating no surface immobilized complex can be formed to reduce oxygen.

In absence of copper, the electrode modified with **1** was investigated for the oxygen reduction reaction. Electron transfer is possible through the grafted layer as was observed in the surface blocking experiments using $K_3[Fe(CN)_6]$ (see section 5.3.3). Outer sphere reduction of O_2 therefore may still be possible and **1** immobilized on the gold electrode might act as an oxygen reduction catalyst as well. In the single sweep voltammogram, reductive current is observed with an onset potential of 0.45 V *versus* RHE. A catalytic wave with a maximum activity of 970 µA

cm^{-2} was observed. The current is 2.5 times higher than the oxygen reduction activity observed on an unmodified electrode in absence of copper (-970 μA cm^{-2} for Au|**1** *versus* -410 μA cm^{-2} for a bare gold electrode). With **1** immobilized on a gold electrode, the onset potential for the reductive current is shifted positively with 100 mV compared to an unmodified gold electrode in presence or absence of Cu^{II}.

An oxygen free solution of Au|**1**|Cu^{II} does not show any redox couples. Oxygen reduction at Au|**1**|Cu^{II} was observed with an onset potential that varied between 0.40 and 0.35 V *versus* RHE within different experiments. The activity at the lower vertex potential ranged between -0.80 to -1.6 mA cm^{-2} over different experiments. The onset shifted positively by 150 to 200 mV compared to the unmodified gold electrode in presence or absence of copper ions in solution, while the onset shifted 100 to 150 mV compared to Au|**1**. The activity is two to four times larger than the unmodified gold electrode in absence of Cu^{II} and equal to to two times larger than Au|**1**.

As mentioned above, the oxygen reduction activity for Au|**1**|Cu^{II} was not the same over all experiments. In some experiments a minor shoulder was observed between 0.50 and 0.30 V. The maximum current observed at the vertex potential of 0.25 V differed from -0.80 to -1.6 mA cm^{-2} in different experiments. The overpotential for oxygen reduction ranged from 0.83 to 0.88 V. In all experiments, the activity of the Au|**1**|Cu^{II} system surpassed the activity observed on a bare gold electrode. The differences in activity and onset potential could be due to the different surface structures formed by the reduction of **1**-N_2^+. With **1** attaching to **1** molecules which are already grafted onto the electrode surface, different surface structures can form during the reduction of **1**-N_2^+, which appears to be difficult to control. These differences could account for the differences observed in the catalytic activity of Au|**1**|Cu^{II} between different experiments. A different explanation could be the number of defects or the surface roughness, which could increase the number of **1** molecules adsorbed on the electrode surface.

In order to investigate the stability of the 1,10-phenanthroline immobilized system, cyclic voltammetry over 200 cycles was performed (Figure 5.14). A decrease in current is observed from 960 μA cm^{-2} in the first scan to 400 μA cm^{-2} in 200th scan. Accompanied by the decrease in activity is the appearance of two oxidation and reduction peaks. There is an oxidation peak increasing with each scan at 0.55 V which is accompanied by a reduction at 0.47 V. The second redox couple has an oxidative peak at 0.73 and a reduction at 0.68 V.

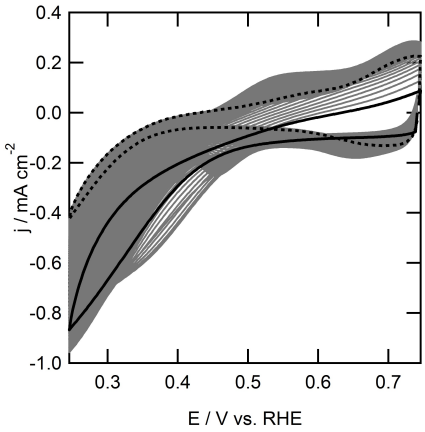

Figure 5.14: Electrochemical behavior of a gold electrode (0.05 cm^2 geometric surface area) grafted with **1** in presence of oxygen in 0.1 M phosphate buffer with 0.05 M NaCl acidified to pH 4 with HCl at 100 mV s^{-1}. First scan is depicted in black, 200th scan is depicted in dotted black line.

Apparently, the Au|**1**|Cu^{II} system is not a very stable system. The decrease in catalytic activity indicates that deactivation of the catalyst or degradation of the organic layer takes place. The Au-**1** bond could be broken and the complex may leach into the electrolyte solution. This would indicate that the gold surface becomes exposed to the electrolyte and that copper ions from the solution can adsorb onto the gold electrode. This would result in redox activity similar to the Au|Cu^{II} system. The redox couples do not completely match between Au|Cu^{II} and Au|**1**|Cu^{II} after 200 cycles of oxygen reduction. Another explanation could be the formation of thick copper layers on top of the phenanthroline layer. The composition of Au|**1**|Cu^{II} as a function of scan number and thus time was investigated by XPS.

5.3.5 XP spectra of Au|1 after different stages of oxygen reduction

The gold 4f peaks of the unmodified electrode are observed at 83.9 eV, which corresponds to literature values of 83.8 eV[16, 17] and 83.9 eV[18] (see Figure 5.15a). In the Au|**1** system, the binding energy and the total intensity of the Au 4f peak does not change, indicating that the adsorbed layer of **1** is very thin. After 25 cycles of oxygen reduction in the Au|**1**|Cu^{II} system a difference

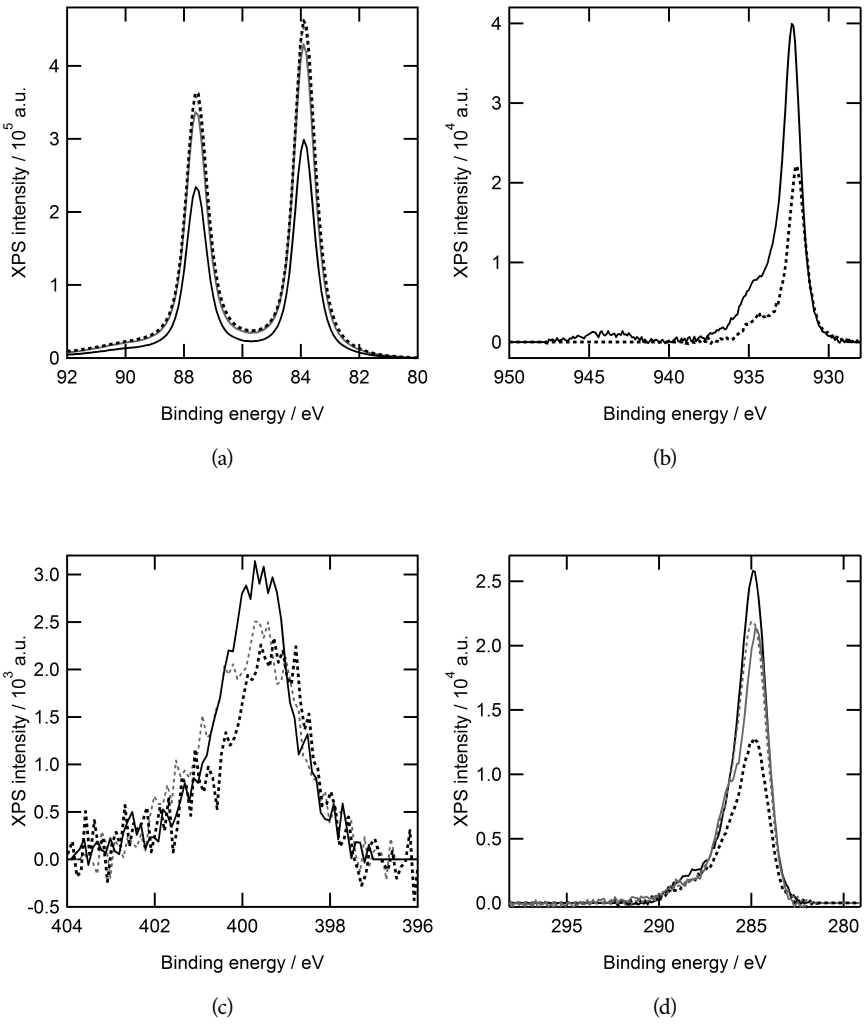

Figure 5.15: *Ex situ* X-ray photoelectron spectra of gold electrodes in the (a) Au 4f region, (b) Cu 2p region, (c) N 1s region and (d) C 1s region of an unmodified electrode (gray solid line), an electrode grafted with **1** (gray dotted line), after 25 cycles of oxygen reduction (black solid line) and after 200 cycles of oxygen reduction (black dotted line).

is observed, the intensity of the Au signals dropped by approximately 30%. 200 cycles of oxygen reduction brings the intensity of the gold 4f peaks back to the value of the unmodified electrode. The position of the peaks does not change during oxygen reduction or by immobilization of **1** on the electrode.

A copper layer is formed during oxygen reduction as is observed by the appearance of the Cu 2p peaks at 932.3 eV after 25 cycles of oxygen reduction (Figure 5.15b). This is in the same region where metallic copper and Cu(I) oxide is observed Literature reports values between 931.5 and 932.4 for Cu(0) and between 931.6 and 932.0 for Cu_2O.[19, 20] Weak satellites are observed between 940 and 947 eV, which is indicative of the presence of Cu(I) oxide.[21] When 200 cycles of oxygen reduction is performed, the total intensity of copper decreases to approximately 50% of the value observed after 25 cycles of oxygen reduction. The peak position shifts to a lower binding energy of 932.0 eV and the satellites between 490 and 497 eV disappear, indicating the copper present may be metallic Cu(0). The decrease in intensity for the Cu 2p peaks is reflected in the higher intensity for the Au 4f peaks, where the intensity returned to values similar to a bare gold or an electrode grafted with **1**.

The N 1s signals of the grafted electrode are observed at 399.6 eV (Figure 5.15c). Upon performing 25 cycles of oxygen reduction, the peak position and XPS intensity do not differ significantly compared to the electrode prior to the catalytic reaction. After 200 cycles of oxygen reduction the binding energy shifts to a slightly lower binding energy of 399.3 eV. This indicates a structural change of the organic layer which must still be present on the electrode surface, which could possibly be the formation of an N-oxide species.

The modified electrode changes during oxygen reduction catalysis. Initially, the electrode is grafted with a thin layer of **1** as the intensity of the gold 4f peaks does not change. After 25 cycles of oxygen reduction, a copper layer is present on the electrode surface, while an organic layer still appears to be present between the electrode and the copper layer. This is observed from a decrease in intensity of the Au 4f peaks, while the carbon and nitrogen peaks are still present in approximately the same intensity. Moreover the copper 2p peaks are present and show weak satellites, which indicates the adsorbed copper is in a reduced form. After 200 cycles of oxygen reduction, the amount of copper on the electrode is halved compared to 25 cycles of oxygen reduction. Also the carbon content is halved, indicating the layer of **1** is undergoing

chemical changes. The intensity of the Au 4f peaks is at approximately the same level as a bare gold electrode. The degradation of the catalyst is also observed in the oxygen reduction activity. At the first 30 scans, the oxygen reduction activity increases, after which it keeps decreasing (Figure 5.14).

5.4 Conclusion

By immobilizing **1** at a gold electrode, oxygen reduction catalysis could be performed in an electrolyte solution containing Cu^{2+} At the start of the catalytic reaction the organic layer is still intact. During catalysis a layer of copper grows on the electrode surface which is accompanied by an increase in catalytic activity. During long term voltammetric cycling there is a change in the structure of the organic layer. As part of this structural change in the copper layer on the electrode surface is diminished while the oxygen reduction activity decreases.

Although the Au|**1**|Cu^{II} system forms an active oxygen reduction catalyst, it is not suitable for an application in an electrochemical cell, as the long-term stability is low and the overpotential is too high. However it is suitable for mechanistic studies, potentially making it a valuable tool in elucidating the mechanism of the oxygen reduction reaction.

5.5 References

(1) McCrory, C. C. L.; Devadoss, A.; Ottenwaelder, X.; Lowe, R. D.; Stack, T. D. P.; Chidsey, C. E. D. *J. Am. Chem. Soc.* **2011**, *133*, 3696–3699.

(2) Laforgue, A.; Addou, T.; Bélanger, D. *Langmuir* **2005**, *21*, 6855–6865.

(3) Gayathri, P.; Senthil Kumar, A. *Langmuir* **2014**, *30*, 10513–10521.

(4) Baranton, S.; Bélanger, D. *J. Phys. Chem. B* **2005**, *109*, 24401.

(5) Yeşildağ, A.; Ekinci, D. *Electrochim. Acta* **2010**, *55*, 7000–7009.

(6) Shul, G.; Weissmann, M.; Bélanger, D. *Electrochim. Acta* **2015**, *162*, 146–155.

(7) Shul, G.; Weissmann, M.; Bélanger, D. *Langmuir* **2014**, *30*, 6612–6621.

(8) Roy, F.; Et Taouil, A.; Lallemand, F.; Heintz, O.; Moutarlier, V.; Hihn, J.-Y. *Ultrason. Sonochem.* **2018**, *40*, 9–16.

(9) Valencia, D. P.; de Souza, A. P. R.; Gonçales, V. R.; Antonio, J. L. S.; Cordoba de Torresi, S. I.; Bertotti, M. *Electrochem. Commun.* **2014**, *38*, 32–35.

(10) Liu, G.; Chockalingham, M.; Khor, S. M.; Gui, A. L.; Gooding, J. J. *Electroanal.* **2010**, *22*, 918–926.

(11) Trasatti, S.; Petrii, O. A. *J. Electroanal. Chem.* **1992**, *327*, 353–376.

(12) Davey, W. P. *Phys. Rev.* **1925**, *25*, 753–761.

(13) Surface Explorer.

(14) Li, Q.; Xu, P.; Zhang, B.; Tsai, H.; Zheng, S.; Wu, G.; Wang, H.-L. *J. Phys. Chem. C* **2013**, *117*, 13872–13878.

(15) Awad, M. I.; Ohsaka, T. *Journal of Power Sources* **2013**, *226*, 306–312.

(16) Dückers, K.; Bonzel, H. P. *Surf. Sci.* **1989**, *213*, 25–48.

(17) Bird, R. J.; Swift, P. *J. Electron Spectros. Relat. Phenomena* **1980**, *21*, 227–240.

(18) Bravo, B. G.; Michelhaugh, S. L.; Soriaga, M. P.; Villegas, I.; Suggs, D. W.; Stickney, J. L. *J. Phys. Chem* **1991**, *95*, 5245–5249.

(19) Ertl, G.; Hierl, R.; Knözinger, H.; Thiele, N.; Urbach, H. *Appl. Surf. Sci.* **1980**, *5*, 49–64.

(20) Klein, J. C.; Proctor, A.; Hercules, D. M.; Black, J. F. *Anal. Chem.* **1983**, *55*, 2055–2059.

(21) Scrocco, M. *Chem. Phys. Lett.* **1979**, *63*, 52–56.

6 | Summary

Chapter 1

Before the large scale use of renewable energy sources can be implemented in our society, the efficient storage of that energy needs to be tackled. The storage of electrical energy in the form of a chemical bond *e.g.* hydrogen or hydrocarbons is a good option for the storage of this renewable energy. Hydrogen can be produced by the electrochemical reduction of protons, which costs energy. This energy can be released by the oxidation of the hydrogen formed. An electrochemical reactions always consists of two half reactions. The water oxidation reaction is a good candidate as second half reaction to complement the proton reduction reaction due to its high redox potential and the non-toxicity of the products, which are oxygen and protons. If the hydrogen is oxidized, oxygen can be reduced to form water. The water oxidation and oxygen reduction reactions are four-electron reactions. As a result the reaction mechanism is complex and difficult to optimize.

There are different types of catalysts which increase the efficiency of the water oxidation and oxygen reduction reactions. In heterogeneous catalysis, the catalyst is in a different phase than the reactant, *e.g.* an electrode (solid) and water (liquid). In homogeneous catalysis, the catalyst and reactant(s) are in the same phase, *e.g.* a molecular complex dissolved in water. Due to the harsh conditions in which water oxidation takes place, the molecular complexes can undergo structural changes and deposit on the electrode surface, effectively making it a heterogeneous catalyst. In extreme cases, a metal oxide catalyst is formed. In the oxygen reduction reaction the ligands of the molecular complex can dissociate from the metallic center and thus form a metallic layer, which is responsible for catalysis. This thesis focuses on the activation of molecular complexes and on strategies to prevent the degradation of molecular complexes in water oxidation

and oxygen reduction catalysis.

Chapter 2

In literature there are several examples of molecular iridium precatalysts for water oxidation. Examples are given where the active catalyst will or will not adsorb on the electrode surface. The adsorbed species can either be of molecular nature or be oxidized completely to form IrO_2.

In Chapter 2 a comparison is made between two similar iridium water oxidation catalysts. The catalysts have pyridyl-triazolylidene ligands where a modification is made on the triazolylidene ring. The proton in the one complex is exchanged for an ethoxy moiety. This modification has a drastic influence on the activation of the molecular precatalyst. Water oxidation with a chemical oxidant reveals the highest activity is observed on the complex with the ethoxy moiety. This indicates the electronic properties of the complexes dictate the activity of the molecular complex. Chapter 2 focuses on the electrochemical water oxidation reaction.

Using an Electrochemical Quartz Crystal Microbalance (EQCM) it was established the complexes form a deposit on the surface of the gold working electrode upon applying a potential of 1.8 V *versus* RHE. This is associated with the deposition of the catalytically active species on the surface of the electrode, as the current increases over time the longer 1.8 V is applied. The formation of gaseous products was investigated using Online Electrochemical Mass Spectrometry (OLEMS). The formation of carbon dioxide was observed at a lower potential than the formation of dioxygen in cyclic voltammetry. The formation of CO_2 is an indication of degradation of the ligand backbone, which is observed for iridium complexes before. The (partly oxidized) complexes which are adsorbed on the electrode surface are still of molecular nature, as was established by X-ray Photoelectron Spectroscopy (XPS).

The current work illustrates a small change in the structure of the complex can have

a large influence of the catalytic activity and the activation of precatalysts. The challenge for the future lies in determining which factors influence the complete degradation of the complex to IrO_2 and how the molecular complexes form well-defined molecular catalysts for the water oxidation reaction.

Chapter 3

The use of a noble metal such as iridium is not ideal in catalysis due to the high cost and relatively low availability of the metals. The use of a first row transition metal such as copper is much cheaper and more readily available than iridium. The electrochemical activation of the $[Cu^{II}(bdmpza)_2]$ complex ($bdmpza^-$ = bis(3,5-dimethyl-1H-pyrazol-1-yl)acetate) is reported in Chapter 3. The complex is coordinatively saturated, indicating water cannot bind to the complex to begin a water oxidation cycle. Since an alkaline electrolyte is used, the complex does not dissolve in the electrolyte and is dropcasted onto the gold working electrode. Upon applying an oxidizing potential above 1.6 V *versus* RHE an oxidation current is observed. In the backward scan from 2 to 0 V a series of four reduction events between 1.25 and 0.25 V are observed. Upon scanning back to 0 V and oxidizing the electrode again a fifteen fold increase is observed in the second scan. The reduction events are associated with a decrease in mass of the quartz-gold-$[Cu^{II}(bdmpza)_2]$ assembly in EQCM. This is an indication part of the ligand is lost during the reduction events. In the oxidative scan up to 1.2 V a second loss in mass is observed which is associated with the dissolution of copper into the electrolyte. The $[Cu^{II}(bdmpza)_2]$ complex was used in an OLEMS investigation. Upon applying 2.0 V a tiny amount of dioxygen is observed. The oxidation period is followed by reduction at 0 V. Finally a second oxidizing potential is applied, which yields a higher current and dioxygen production. Two pathways in which an active water oxidation catalyst forms can be discerned: an oxidative pathway and a reductive-oxidative pathway. In both pathways the structure of the active catalyst is CuO. Since the active catalyst is the same for

both activation pathways, the same maximum activity is expected. However the activation by the oxidative pathway is much slower and thus has not reached the same activity as the reductive pathway.

Chapter 4

In Chapter 4 an investigation of the oxygen reduction reaction with *in situ* generated copper-phenanthroline complexes is discussed. Using Electron Paramagnetic Resonance (EPR) spectroscopy the geometry of the copper complexes which are formed is determined. At a ratio of 1,10-phenanthroline to copper ions of 2:1 up to 10:1 the complex formed *in situ* has a trigonal bipyrimidal geometry around the copper center. At a 10:1 ratio a reversible redox couple is observed in deoxygenated aqueous electrolyte. The reversible redox couple follows the Randles Cevčik relation, indicating the redox couple is a one-electron transfer process. Unfortunately the trigonal bipyrimidal complex does not show any oxygen reduction activity. A 1:1 complex generated *in situ* by addition equimolar amounts of 1,10-phenanthroline and Cu^{II} is instead an active oxygen reduction catalyst. The 1:1 complex is in the elongated octahedron geometry as is determined by EPR spectroscopy. The complex displays an irreversible redox couple in deoxygenated aqueous electrolyte. Due to the absence of a reversible redox couple the formation of metallic copper layers on the gold working electrode is possible. A new strategy to prevent the deposition of copper on the working electrode is proposed and is reported in Chapter 5.

Chapter 5

The reduction of diazonium compounds ($R-N_2^+$) at an electrode leads to liberation of dinitrogen and the formation of a radical ($R^\bullet$). The radical can couple to the electrode surface thus forming a relatively strong (covalent) bond. This reduction of diazonium ions in aqueous solution is well-documented for benzene-diazonium and its derivatives.

Copper complexes with 1,10-phenanthroline ligands are only active oxygen reduc-

tion catalysts if there is only one 1,10-phenanthroline ligand present on the copper center, as was reported in Chapter 4. The 1,10-phenanthroline-5-diazonium ions are generated *in situ* by the addition of 5-amino-1,10-phenanthroline and sodium nitrite. By the reduction of 1,10-phenanthroline-5-diazonium the 1,10-phenanthroline derivative is immobilized on the electrode surface. The surface coverage is determined by EQCM and is 0.4 nmol cm^{-2}. This equals 18 molecules per 100 Au atoms, whereas 50 molecules should fit a Au (111) surface if the molecules are aligned perfectly. This indicates submonolayer coverage of the molecules. By immobilizing the 1,10-phenanthroline derivative on the working electrode and upon addition of a Cu^{II} salt in the electrolyte solution, a surface-attached complex is formed.

The oxygen reduction behavior of the Cu^{II}-phen complex immobilized on a gold electrode was determined and compared to different other systems. These involve the bare gold electrode, an electrode modified by the reduction of *in situ* generated 5-bromobenzene-diazonium, the electrode modified by reduction of 5-bromobenzene-diazonium in presence of $Cu^{II}$and the 1,10-phenanthroline modified electrode in absence of Cu^{II}. In all cases the Cu^{II}-phen is reducing oxygen at the lowest overpotential and the activity is also highest for the Cu^{II}-phen system.

The Cu^{II}-phen system is not very stable. Different redox couples grow into the cyclic voltammogram upon prolonged cycling. These redox couples are associated with the formation of metallic copper on the electrode-complex assembly. XPS results show accumulation of metallic copper on the electrode surface, while an organic layer is still present on the electrode as well.

The immobilized Cu^{II} complexes described in this chapter is unsuitable for large-scale electrochemical oxygen reduction. However the system can be used for fundamental studies on the oxygen reduction reaction. The difficulty in mechanistic studies on homogeneous electrocatalysis lies in the large portion of catalyst which is inactive. This

is due to the largest portion of catalyst being in the bulk of the electrolyte and not close to the electrode surface. By immobilizing the catalyst on the electrode surface all of the catalyst present is doing oxygen reduction at the same time. This allows to watch the complex in action and not while almost all of the catalyst is in its resting state far from the electrode surface. Moreover the rigidity of the immobilized ligands allow for control of the structure of the complex.

The presence of an organic layer on the electrode after oxygen reduction catalysis indicates the immobilized phenanthroline molecules are still present on the electrode surface. By optimizing the concentration of copper ions in solution the formation of metallic copper might be prevented.

Samenvatting

Hoofdstuk 1

Het op grote schaal opslaan van duurzaam geproduceerde elektriciteit is een grote uitdaging. Een van de veelbelovende mogelijkheden is het opslaan van de energie in de vorm van een chemische verbinding, zoals waterstof. Waterstof kan geproduceerd worden door de elektrochemische reductie van protonen. Deze reactie kost energie, welke vrijkomt als de waterstof geoxideerd wordt naar protonen. Zo een reactie heet een halfreactie. Een elektrochemische reactie bestaat altijd uit twee halfreacties. De water oxidatie reactie is een goede kandidaat als tweede halfreactie, doordat de gevormde producten, namelijk zuurstof en protonen, niet toxisch zijn en het een hoge oxidatie potentiaal heeft. Wanneer het waterstof geoxideerd wordt, kan zuurstof gereduceerd worden naar water. De water oxidatie en zuurstof reductie reacties zijn vier-elektronen reacties. Dit heeft tot gevolg dat het reactiemechanisme complex en moeilijk te optimaliseren is.

Er zijn verschillende soorten katalysatoren welke de efficiëntie van de water oxidatie en zuurstof reductie reacties kunnen beïnvloeden. Het is mogelijk dat de elektrode waar elektronenoverdracht plaatsvindt de katalysator is. Daarbij zit de katalysator in een andere fase (vast) dan de reactanten (vloeibaar). Dit wordt heterogene katalyse genoemd. Een andere optie is waar de katalysator, bijvoorbeeld een moleculair complex, en de reactanten in dezelfde fase zitten. Dat wordt homogene katalyse genoemd. Omdat de water oxidatie reactie een hoge evenwichtspotentiaal heeft, zijn de omstandigheden waarbij water geoxideerd wordt extreem. Hierdoor kunnen de moleculaire complexen structurele veranderingen ondergaan en een depositie vormen op het elektrodeoppervlak. Zo wordt een heterogene katalysator gemaakt. In ernstige gevallen kan het moleculaire complex volledig geoxideerd worden en een metaal-oxide katalysator vormen. Bij de zuurstof reductie reactie ligt ook het gevaar voor het vormen van een heterogene

katalysator op de loer. Onder reductieve omstandigheden kunnen de liganden rond het moleculaire complex dissociëren. Het metaal-ion kan dan een depositie vormen op de elektrode en zo een heterogene katalysator vormen, die niet meer gezien kan worden als een moleculaire verbinding. In dit proefschrift wordt de focus gelegd op de activatie van moleculaire (pre)katalysatoren en op strategieën waarmee de degradatie van moleculaire complexen voorkomen kan worden.

Hoofdstuk 2

In de literatuur zijn verschillende voorbeelden te vinden van moleculaire iridium (pre)katalysatoren voor de water oxidatie reactie. Er zijn voorbeelden waarbij een depositie op het oppervlak van de elektrode gevormd wordt, welke verantwoordelijk is voor de water oxidatie activiteit. De geadsorbeerde katalysator kan moleculair zijn, maar kan ook volledig geoxideerd zijn naar IrO_2.

In Hoofdstuk 2 wordt een vergelijking gemaakt tussen twee vergelijkbare iridium water oxidatie katalysatoren. De katalysatoren hebben een pyridyl-triazolylideen ligand waarbij een modificatie is gemaakt op de triazolylideen ring. Het proton in het ene complex is verwisseld met een ethoxy groep. Deze modificatie heeft een drastisch effect op de activatie van de prekatalysator. Door water te laten oxideren met een chemische oxidant is aangetoond dat het complex met de ethoxy groep een snellere activatie heeft dan het complex met de proton op de triazolylideen ring. Hieruit kan geconcludeerd worden dat de elektronische eigenschappen van het metaal-ion een belangrijke rol spelen in de oxidatie van water met een chemisch oxidant. Het onderzoek in Hoofdstuk 2 richt zich op de elektrochemische water oxidatie.

Met behulp van een Elektrochemische Kwarts Kristal Microbalans (EQCM) is vastgesteld dat een depositie wordt gevormd op het oppervlak van de goud elektrode indien een potentiaal van 1,8 V tegen de reversibele waterstof elektrode (RHE) wordt aangelegd. Deze massatoename wordt geassocieerd met de vorming van een katalytisch actieve laag

op het oppervlak van de elektrode, want de stroom wordt groter naarmate de potentiaal langer is aangelegd. De vorming van gasvormige producten is onderzocht met behulp van Online Elektrochemische Massaspectrometrie (OLEMS). Koolstofdioxide wordt op een lagere potentiaal gevormd dan zuurstof in cyclische voltammetrie. Koolstofdioxide wordt gevormd wanneer (een van) de liganden rond het metaalcentrum geoxideerd wordt. Dit is al vaker gezien voor moleculaire iridium complexen voor de water oxidatie reactie. Röntgen Fotoelektronen Spectroscopie (XPS) heeft aangetoond dat de depositie die gevormd wordt nog steeds een moleculaire verbinding is.

Dit Hoofdstuk toont aan dat een kleine verandering in de structuur van een moleculaire verbinding een zeer groot effect kan hebben op de activiteit en de activatie van water oxidatie prekatalysatoren. Men moet voorzichtig zijn met het trekken van conclusies uit experimenten met water oxidatie katalysatoren welke getest zijn met chemische oxidanten, omdat de activatie kan verschillen met elektrochemische experimenten. Het bepalen van de factoren welke van invloed zijn op de oxidatie van prekatalysatoren is een van de uitdagingen voor de toekomst. Een andere uitdaging is het bepalen welke factoren een rol spelen bij het vormen van een goed gedefinieerde water oxidatie katalysator.

Hoofdstuk 3

Het gebruik van een edelmetaal zoals iridium is niet ideaal voor grootschalig gebruik vanwege de hoge kosten en beperkte beschikbaarheid van deze metalen. Een 3d-overgangsmetaal is veel goedkoper en meer beschikbaar dan iridium. Koper is zo een 3d-over-gangsmetaal. De chemische activatie processen van $[Cu^{II}(bdmpza)_2]$ (bdmpza$^-$ = bis(3,5-dimethyl-1H-pyrazol-1-yl)acetaat) wordt besproken in Hoofdstuk 3. Er kunnen geen andere liganden binden aan het complex, wat betekent dat water niet direct kan binden aan het complex om geoxideerd te worden. Omdat er voor een basisch elektrolyt gekozen is, kan het complex niet in het elektrolyt oplossen. Het complex is opgelost in ethanol en met een pipet op de goud elektrode opgebracht, waarna de ethanol ver-

dampt is. In cyclische voltammetrie van 0,7 V tegen RHE in positieve richting wordt boven een potentiaal van 1,6 V tegen RHE wordt een oxidatiestroom geobserveerd. In de teruggaande scan van 2,0 naar 0 V tegen RHE worden vier reducties onderscheiden. In de tweede scan wordt een vijftien keer hogere stroom geobserveerd op 2,0 V dan in de eerste scan. De reductiepieken in de teruggaande scan worden geassocieerd met een afname van massa van de kwarts-elektrode-$[Cu^{II}(bdmpza)_2]$ combinatie in EQCM. Dit is een indicatie dat het ligand dissocieert van het metaalcentrum en in de elektrolyto-plossing gaat tijdens de reductie. In de oxidatieve scan naar 1,2 V tegen RHE gaat meer massa verloren van de elektrode. Dit wordt in verband gebracht met een klein verlies van koper wat oplost in het elektrolyt. Tevens is een OLEMS onderzoek uitgevoerd. Hierbij is eerst 2,0 V aangelegd, waarna het complex gereduceerd is op 0 V en ten slotte opnieuw geoxideerd op 2,0 V. In de initiële oxidatie wordt een oxidatiestroom en een minimale hoeveelheid zuurstof geobserveerd. Na de reductie op 0 V wordt in de tweede oxidatie een hogere stroom en zuurstofproductie geobserveerd. Met XPS is vastgesteld dat CuO de actieve water oxidatie katalysator is.

Twee routes voor de activatie van de water oxidatie kunnen worden onderscheiden: een oxidatieve en een reductieve-oxidatieve route. Aangezien de actieve katalysator voor beide activatiewegen hetzelfde is, zou de maximale activiteit van beide routes hetzelfde moeten zijn. Aangezien de snelheid van de activatie in de oxidatieve route vele malen langzamer is, wordt tijdens de uitgevoerde experimenten niet dezelfde activiteit geob-serveerd.

Hoofdstuk 4

In Hoofdstuk 4 wordt de zuurstof reductie capaciteit van *in situ* gegenereerde koper-1,10-fenanthroline-complexen besproken. Met behulp van Elektronspinresonantie (EPR) spectroscopie kan de geometry van de complexen in oplossing worden bepaald. Als een koper:fenanthroline van 1:2 tot 1:10 wordt gebruikt hebben de complexen die *in*

situ worden gevormd een trigonaal bipyrimdale geometry rond het koper-ion. Bij een 1:2 verhouding wordt in een zuurstofvrije elektrolyt een reversibel redox koppel geobserveerd. Dit redox koppel volgt de Randles Cevčik relatie, welke aangeeft dat in het redox koppel per molecuul één elektron overgedragen wordt. Het complex met een trigonaal bipyrimidale geometry is niet actief voor de zuurstof reductie reactie. Een 1:1 complex welke *in situ* gegenereerd is, is wel een actieve katalysator voor de zuurstof reductie reactie. EPR spectroscopie heeft aangetoond dat het complex zich in een verlengde octaëder geometrie bevindt. In een zuurstofvrij elektrolyt wordt in het cyclische voltammogram een irreversibel redox koppel geobserveerd. Het ontbreken van een reversibel redox koppel kan indicatief zijn voor de formatie van metallisch koper op het oppervlak van de elektrode. Een nieuwe strategie is nodig om te voorkomen dat er metallische koperlagen op het oppervlak van de elektrode gevormd kunnen worden. Deze strategie bestaat uit het immobiliseren van de fenanthroline liganden op het oppervlak van de elektrode. Hierdoor wordt verzekerd dat een 1:1 Cu^{II} tegen 1,10-fenanthroline ratio complexen gevormd wordenen mogelijk dat de liganden de depositie van koper op het elektrodeoppervlak voorkomen wordt. Deze strategie wordt in Hoofdstuk 5 nader besproken.

Hoofdstuk 5

Bij de reductie van diazonium verbindingen (R-N_2^+) aan het oppervlak van een elektrode wordt stikstof vrijgemaakt en vormt zich een radicaal ($R^\bullet$). Dit radicaal kan koppelen aan het elektrodeoppervlak en vormt daarmee een relatief stabiele (covalente) verbinding. Deze reductie van diazonium ionen in waterige oplossingen is goed gedocumenteerd voor benzeen-diazonium en derivaten. Zoals besproken in Hoofdstuk 4 zijn koper complexen met 1,10-fenanthroline liganden alleen actieve zuurstof reductie katalysatoren indien er één fenanthroline ligand gecoördineerd is aan het koper ion. De 1,10-fenanthroline-5-diazonium ionen worden gegenereerd door 5-amino-1,10-fenanthroline en na-

triumnitriet in zuurstofvrij elektrolyt bij elkaar te voegen. 1,10-fenanthroline wordt geïmmobiliseerd op het oppervlak door de reductie van 1,10-fenanthroline-5-diazonium. Met EQCM is de oppervlakteconcentratie van het 1,10-fenanthroline bepaald op 0,4 nmol cm^{-2}. Deze waarde komt overeen met 18 moleculen per 100 goud atomen. Indien de moleculen perfect uitgelijnd worden zouden er 50 moleculen op moeten passen als wordt uitgegaan van een perfect (111) oppervlak. Er is dus minder dan één monolaag moleculen op het goudoppervlak. Door de immobilisatie van de 1,10-fenanthroline op het oppervlak en met koper ionen in oplossing kan een complex gevormd worden aan het elektrodeoppervlak.

De activiteit voor zuurstof reductie is bepaald en vergeleken met verschillende andere systemen. Deze andere systemen zijn een niet-gemodificeerde goud elektrode in afwezigheid van Cu^{II}, een elektrode welke gemodificeerd door de reductie van *in situ* gegenereerde 5-bromobenzeen-diazonium in aanwezigheid van Cu^{II} en een elektrode gemodificeerd met 1,10-fenanthroline in afwezigheid van Cu^{II}. De overpotentiaal van de geïmmobiliseerde complexen is in alle gevallen lager dan de andere systemen. De zuurstof reductie activiteit is hoogste voor de geïmmobiliseerde complexen.

Het Cu^{II}-phen systeem is niet stabiel. Verscheidene irreversibele redox koppels ontstaan bij langdurig scannen in het cyclisch voltammogram. Deze redox koppels worden geassocieerd met de vorming van metallisch koper op het elektrodeoppervlak. XPS heeft aangetoond dat er nog wel een organische laag aanwezig is op de elektrode en dat de liganden dus nog wel aanwezig zijn op de elektrode. Wel wordt er een laag koper gezien op de elektrode.

De geïmmobiliseerde Cu^{II} complexen die in dit Hoofdstuk worden gerapporteerd zijn niet geschikt voor een toepassing op grote schaal. Het systeem is echter wel geschikt voor fundamenteel onderzoek naar het reactiemechanisme van de zuurstof reductie reactie. In homogene elektrokatalyse bevindt het grootste gedeelte van de katalysatoren

zich in het elektrolyt ver weg van de elektrode. Deze katalysatoren zijn in hun rusttoestand en dragen niet bij aan het ontrafelen van het reactiemechanisme. Door de immobilisatie van de complexen is er een kleine hoeveelheid katalysator aanwezig welke volledig actief is. Dat houdt in dat het zeer geschikt is om onderzoek te doen aan het reactiemechanisme van zuurstof reductie.

De aanwezigheid van de organische laag tussen de elektrode en de metallische koperlaag geeft aan dat het systeem nog in tact is. Door de koperconcentratie in oplossing te optimaliseren bestaat de kans dat er een stabiel katalytisch systeem ontstaat. De optimalisatie van de koperconcentratie is een goede vervolgstudie.

List of Publications

This thesis

Chapter 2

Relevance of Chemical vs. Electrochemical Oxidation of Tunable Carbene Iridium Complexes for Catalytic Water Oxidation

Marta Olivares, *Cornelis J.M. van der Ham*, Mo Li, Markus Schmidtendorf, Helge Müller-Bunz, M.G.W.M. (Tiny) Verhoeven, J.W. (Hans) Niemantsverdriet, Dennis G.H. Hetterscheid, Stefan Bernhard & Martin Albrecht

Submitted

Chapter 3

Activation pathways taking place at molecular copper precatalysts for the oxygen evolution reaction

Cornelis J.M. van der Ham, Furkan Işık, M.G.W.M. (Tiny), J.W. (Hans) Niemantsverdriet & Dennis G.H. Hetterscheid

Catal. Today **2017**, *290*, 33–38

Chapter 4

In situ generated copper-phenanthroline complexes as catalysts for the oxygen reduction reaction

Cornelis J.M. van der Ham, Jan P. Hofmann & Dennis G.H. Hetterscheid

In preparation for publication

Chapter 5

Phenanthroline immobilized on Au electrodes as ligand in copper-mediated oxygen re-

duction

Cornelis J.M. van der Ham, Damy Zwagerman, Jan P. Hofmann & Dennis G.H. Hetterscheid

In preparation for publication

Other publications

A new mechanism for the selectivity to C1 and C2 species in the electrochemical reduction of carbon dioxide on copper electrodes

Klaas J. P. Schouten, Youngkook Kwon, *Cornelis J. M. van der Ham*, Zhisheng Qin & Marc T. M. Koper

Chem. Sci. **2011**, *2*, 1902–1909

Challenges in Reduction of Dinitrogen by Proton and Electron Transfer

Cornelis J.M. van der Ham, Marc T.M. Koper, & Dennis G.H. Hetterscheid

Chem. Soc. Rev. **2014**, *43*, 5183–5191

Early stages of catalyst aging in the iridium mediated water oxidation reaction

Dennis G.H. Hetterscheid *Cornelis J.M. van der Ham*, Oscar Diaz-Morales, M.G.W.M. (Tiny) Verhoeven, Allesandro Longo, Dipanjan Banerjee, J.W. (Hans) Niemantsverdriet, Joost N.H. Reek & Martin C. Feiters

Phys. Chem. Chem. Phys. **2016**, *18*, 10931–10940

Validation of EXAFS Analysis of Iridium Compounds

Martin C. Feiters, Allesandro Longo, Dipanjan Banjeree, *Cornelis J.M. van der Ham* & Dennis G.H. Hetterscheid

J. Phys. Conf. Ser. **2016**, *712*, 012059

Electrochemical and Spectroscopic Study of Mononuclear Ruthenium Water Oxidation Catalysts: A Combined Experimental and Theoretical Investigation

Jessica M. de Ruiter, Robin L. Purchase, Adriano Monti, *Cornelis J.M. van der Ham*, Maria P. Gullo, Khurram S. Joya, Mila D'Angelantonio, Andrea Barbieri, Dennis G.H. Hetterscheid, Huub J.M. de Groot & Fransesco Buda

ACS Catal. **2016**, *6*, 7340–7349 (2016)

Detangling Catalyst Modification Reactions from the Oxygen Evolution Reaction by Online Mass Spectrometry

Paula Abril, M. Pilar del Río, Cristina Tejel, M.G.W.M. (Tiny) Verhoeven, J.W. (Hans) Niemantsverdriet, *Cornelis J.M. van der Ham*, Konstantin G. Kottrup & Dennis G.H. Hetterscheid

ACS Catal. **2016**, *6*, 7872–7875

Influence of muzzle instability on bullet deflection, after perforating laminated particle boards

Wim Kerkhof, Ivo Alberink, *Cornelis J.M. van der Ham* & Erwin J.A.T. Mattijssen

Accepted in *J. Forensic Sci.*

doi: 10.1111/1556-4029.14171

Curriculum Vitae

Cornelis Jozef Maria van der Ham was born on September 14th, 1989 in Gouda, the Netherlands. He obtained his high school diploma from the Coenecoop College in Waddinxveen in 2008. He started the joint BSc program *Molecular Science and Technology* at the Leiden and Delft universities, which he in the group of prof. dr. M.T.M. Koper under the supervision of dr. K.J.P. Schouten with a thesis titled *Electro reduction of CO_2 on copper electrodes: investigating a recently suggested mechanism.* in 2011. Subsequently he started his MSc in Chemistry at Leiden University, where he specialized in physical chemistry.

He did an internship at Shell Technology Center Amsterdam under the supervision of dr. A. van Bavel and H. Oosterbeek entitled *A surface science study on model catalysts on the mechanism of the Fischer Tropsch reaction*. He obtained his MSc degree in 2013 on a thesis entitled *Working towards ethanol dissociation on Pt(533)* supervised by dr. L.B.F. Juurlink and dr. A. den Dunnen.

In 2013 he started his PhD at Leiden University in the Catalysis and Surface Chemistry group under the supervision of prof. dr. M.T.M. Koper and dr. D.G.H. Hetterscheid, the results of which are published in this thesis. The results are presented in oral presentations at the COST action CARISMA meeting in Tarragona, Spain in 2015 and at the NWO CHAINS conference in Velthoven, the Netherlands in 2016. Poster presentations were given at the Netherlands' Chemistry and Catalysis Conference (NCCC) in Noordwijkerhout in 2014, at NWO CHAINS in 2015 in Velthoven, at the meeting of the International Society of Electrochemistry in The Hague in 2016 and at the COST action CARISMA meeting in Lisbon in 2017. As part of the PhD program he attended the NIOK course *Catalysis an Integrated Approach* and the HRSMC course *Physical Methods in Inorganic Chemistry*,

He is currently working in the gunshot residues group at the Netherlands Forensic Institute.

Acknowledgments

I would like to start out by thanking dr. Hetterscheid and prof. dr. Koper for the opportunity to pursue my PhD in the Catalysis and Surface Chemistry group at Leiden University.

I would also like to thank all the fantastic colleagues of both the CASC group and the Metals in Catalysis Biomemetics and Inorganic Materials groups. The nice working atmosphere allowed me to learn a lot about inorganic chemistry and even a little bit of synthetic chemistry. A special thanks to Konstantin, who showed me the way around the inorganic labs and helped me with what little synthesis I did. Martijn, thank you for the fruitful discussions on both science as well as the other aspects of life, especially religion. I would like to thank the other people from the Hetterscheid group, as they made me think about what I did and why as I was teaching them the special ways of electrochemistry.

A word of gratitude to prof. dr. Albrecht and Marta Olivares for a fruitful collaboration which resulted in Chapter 2. I would also like to thank prof. dr. Niemantsverdriet, Tiny Verhoeven and dr. Hofmann for all the help with the XPS measurements.

A special thanks also to the people who raised met. Pa en ma, dank voor alles wat jullie mij geleerd hebben. Voor het achter mijn broek aan zitten als dat nodig was, maar vooral ook voor het laten zien hoe je een ander lief kunt hebben en de liefde die jullie mij gegeven hebben. Pa en ma, Bart en Joyce, Janneke en Swen, bedankt voor alle steun die jullie tijdens mijn studies hebben gegeven. Ma wat had ik je graag bij gehad op de dag dat ik dit boekje mag verdedigen. Marjo, wat ben ik blij met jouw support, zeker het laatste jaar dat ik met dit boekje bezig ben geweest.

En natuurlijk mag een heel groot dank je wel voor Colombe niet ontbreken. Je maakt me een beter mens, steunt me in mijn werk en ik kan altijd op je terugvallen. Ik ben er verschrikkelijk trots op dat ik je nu mijn vrouw mag noemen. Murakoze cyane!